PNNL-15121

Pacific Northwest National Laboratory
Operated by Battelle for the U.S. Department of Energy

Uranium Geochemistry in Vadose Zone and Aquifer Sediments from the 300 Area Uranium Plume

Editor
J. M. Zachara

Collaborators
J. A. Davis
J. P. McKinley
D. M. Wellman
C. Liu
N. Qafoku
S. B. Yabusaki

July 2005

Prepared for the U.S. Department of Energy
under Contract DE-AC05-76RL01830

DISCLAIMER

PACIFIC NORTHWEST NATIONAL LABORATORY
operated by
BATTELLE
for the
UNITED STATES DEPARTMENT OF ENERGY
under Contract DE-AC05-76RL01830

Printed in the United States of America

Available to DOE and DOE contractors from the
Office of Scientific and Technical Information,
P.O. Box 62, Oak Ridge, TN 37831-0062;
ph: (865) 576-8401
fax: (865) 576-5728
email: reports@adonis.osti.gov

Available to the public from the National Technical Information Service,
U.S. Department of Commerce, 5285 Port Royal Rd., Springfield, VA 22161
ph: (800) 553-6847
fax: (703) 605-6900
email: orders@ntis.fedworld.gov
online ordering: http://www.ntis.gov/ordering.htm


This document was printed on recycled paper.
(8/00)

PNNL-15121

Uranium Geochemistry in Vadose Zone and Aquifer Sediments from the 300 Area Uranium Plume

Editor
J. M. Zachara[(a)]

Collaborators
J. A. Davis[(b)] C. Liu[(a)]
J. P. McKinley[(a)] N. Qafoku[(a)]
D. M. Wellman[(a)] S. B. Yabusaki[(a)]

July 2005

Prepared for
the U.S. Department of Energy
under Contract DE-AC05-76RL01830

(a) Pacific Northwest National Laboratory, Richland, Washington
(b) U.S. Geological Survey, Menlo Park, California

Summary

In 1996, an interim record of decision was issued for the 300-FF-5 Operable Unit on the Hanford Site in southeast Washington State. The record of decision specified the interim remedy as (1) continued monitoring of groundwater and (2) institutional controls to restrict groundwater use. This record of decision was based on a remedial investigation that suggested levels of uranium would decrease with time because of natural geochemical and hydrologic processes. A prediction was made that concentrations of uranium would decrease to the proposed drinking water standard or lower (20 µg/L) in 3 to 10 years from 1993. This prediction has not been realized, prompting investigations and update of the conceptual model for uranium in the 300 Area.

In June 2002, the U.S. Department of Energy (DOE) asked scientists at Pacific Northwest National Laboratory's (PNNL) Remediation and Closure Science (RCS) Project to begin research on the 300 Area uranium plume, in collaboration with a small team of investigators from the Environmental Management Science Program, currently funded through the U.S. Department of Energy Office of Biological and Environmental Research. The study completed by the RCS Project, and summarized in this report, will be used to improve the conceptual model of the 300 Area uranium plume and develop a final record of decision for the 300-FF-5 Operable Unit.

Significant progress has been made on planned research and is summarized in this report. The information in this report is of a technical nature and is intended to provide the scientific basis for re-evaluation of the 300-FF-5 record of decision. The following are important conclusions and implications:

1. Residual hexavalent uranium U(VI) concentrations observed beneath the north and south process ponds (NPP and SPP) are heterogeneous and display no marked trend with depth. An average of 37.5% of the residual, sorbed uranium appears accessible to dissolution/desorption, but variation in this number between sediments is large. Dissolution/desorption extent was found to decrease with decreasing water content and at 21% water saturation was only 1 to 3% of total uranium.

2. Both precipitated and adsorbed U(VI) exists in the sediments. No evidence was found for precipitated U(VI) or metallic uranium. A precise demarcation of precipitated and adsorbed forms, and their relative concentrations is difficult. Adsorbed U(VI) predominates in sediments with total uranium <25 mg/kg.

3. The vadose zone sediments beneath both SPP and NPP will remain as potential source terms to maintain groundwater U(VI) concentrations at or above the drinking water standard. Their ultimate impact will be controlled by moisture flux rates through the vadose zone and their bicarbonate concentrations. Increasing groundwater levels at high river stage will solubilize sorbed U(VI) from the capillary fringe and lower vadose zone.

4. The extent of adsorption decreases with increasing aqueous bicarbonate concentration. U(VI) is adsorbed by 300 Area vadose zone and aquifer sediments more strongly than previously recognized. Travel times for adsorption and desorption fronts through the aquifer will consequently be longer by factors of 2 to 5, or even more.

5. The intrusion of river water into the aquifer during periods of high river stage has two different effects: (1) River water dilutes the total ion composition of near shore groundwater and decreases its bicarbonate concentration. This dilution increases U(VI) adsorption to aquifer solids, which further decreases aqueous U(VI) concentrations below the dilution value. Increased adsorption slows the dissipation of the U(VI) groundwater plume and reduces the discharge of U(VI) from the groundwater plume to the Columbia River. (2) Farther inland, a pressure front advances many meters from the river shoreline into the aquifer that raises the groundwater level into the lower vadose zone. Deep vadose zone sediments below the process ponds and trenches contain sorbed U(VI) that desorbs slowly as water levels rise into them, resulting in higher dissolved U(VI) concentrations in waters near the surface of the aquifer. These higher U(VI) concentrations are released into the aquifer proper as water levels drop in response to changing river stage. Thus, rising and falling river stage provides a hydrologic mechanism to mobilize U(VI) from the vadose zone and transport it to groundwater.

6. The vadose zone and aquifer sediments beneath the SPP and NPP differ significantly in sorption properties for uranium. A single value of K_d is therefore unlikely to yield realistic simulations of U(VI) geochemical behavior in the 300 Area plume given heterogeneity in sediment properties and the apparent importance of kinetic processes. Reactive transport modeling of the future dynamics of the plume will consider these issues.

7. The dissolution of U(VI) containing solids and the desorption of U(VI) surface complexes in the contaminated sediments are slow. Equilibrium-based models don't capture the slow release and have led to shorter predictions of the time required for plume dissipation to the maximum contaminant level.

8. A significant amount of copper was disposed to the 300 Area process ponds along with uranium. Total copper concentrations in vadose zone sediments correlated closely with total uranium, but copper concentrations were generally one hundred times larger. In contrast, total copper concentrations in the groundwater fines were smaller than U(VI). Microscopic and spectroscopic measurements showed that copper had precipitated on vadose zone mineral grain surfaces, apparently as a result of neutralization of waste fluid pH. The copper is currently immobilized and has shown low water solubility. Continued low solubility is expected under the current geochemical conditions. The future migration potential of the precipitated copper is low unless the pH decreases for unexpected reasons.

Acronyms

AAO	acid ammonium oxalate
AGW	artificial groundwater
ALS	advanced light source
AMOX	ammonium oxalate
BC	boundary conditions
bgs	below ground surface
CCD	charge-coupled device
CERCLA	Comprehensive Environmental Response, Compensation, and Liability Act
CLIFM	cryogenic laser induced fluorescence microscopy
CLLIFS	cryogenic laser induced fluorescence spectroscopy
DCB	dithionite citrate bicarbonate
DOE	U.S. Department of Energy
DRM	distributed rate model
EDL	electrical double layer
EMP	electron microprobe
EXAFS	extended x-ray absorption fine structure
FRT	fluid residence time
HH	hydroxylamine hydrochloride
LHeT	liquid helium temperature
MCL	maximum contaminant level
NP	North Process Pond samples in 1991 prior to excavation
NPP	North Process Pond
PNC-CAT	Pacific Northwest Consortium Collaborative Access Team
PNNL	Pacific Northwest National Laboratory
mg/kg	parts per million (ppm)
RESRAD	Residual Radioactivity Dose Model
SCM	surface complexation model
SEM	scanning electron microscopy
SPP	South Process Pond
TRLFS	time-resolved laser fluorescence spectroscopy
UMTRA	uranium mill tailings remedial action
USGS	U.S. Geological Survey
XANES	x-ray absorption near-edge spectroscopy
XAS	x-ray absorption spectroscopic
XMP	x-ray microprobe
XRD	x-ray diffraction
XRF	x-ray fluorescence

Element and Chemical Nomenclature

$CaCO_3$	calcite
$Ca\ UO_2(CO_3)_3$	calcium uranyl carbonate
Cu	copper
CuO	cuprous oxide
$Cu(UO_2)_2(PO_4)_2 \cdot 8(H_2O)$	metatorbernite
$Cu_2(CO_3)(OH)_2$	malachite
HCO_3	bicarbonate
U	uranium
UO_2	uraninite
UO_2CO_3	rutherfordine
$UO_2(CO_3)_3^{2-}$	uranyl tri-carbonate

Contents

Summary iii

Acronyms v

1.0 Introduction 1.1

2.0 Scientific Findings 2.1

2.1 Sampling and Characterization 2.1

2.1.1 Results 2.1

2.1.2 Synopsis and Implications 2.2

2.2 Spatial Distribution of Uranium 2.11

2.2.1 Results 2.12

2.2.2 Synopsis and Implications 2.14

2.3 Spectroscopic Measurements of Chemical Speciation 2.23

2.3.1 Results 2.23

2.3.2 Synopsis and Implications 2.25

2.4 Batch Adsorption/Desorption Studies, K_d Measurement, and Surface Complexation Modeling 2.31

2.4.1 Results 2.31

2.4.2 Synopsis and Implications 2.34

2.5 Advective Desorption and Adsorption Studies of Uranium with Contaminated Vadose Zone and Capillary Fringe Sediments 2.44

2.5.1 Results 2.45

2.5.2 Synopsis and Implications 2.50

2.6 Variably Saturated Flow and Transport Modeling in the 300 Area 2.61

2.6.1 Results 2.62

2.6.2 Synopsis and Implications 2.63

2.7 Recharge-Driven Uranium Transport in the Vadose Zone 2.75

2.7.1 Results 2.76

2.7.2 Synopsis and Implications 2.77

2.8 Solution Chemistry Effects on Saturated Uranium Reactive Transport 2.82

2.8.1 Results 2.83

2.8.2 Synopsis and Implications 2.83

3.0 An Integrated Conceptual Model 3.1
4.0 References 4.1

Figures

1.1 300-FF-5 Operable Unit is Located in the Southeast Part of the Hanford Site 1.3
2.1 Map of the 300 Area 2.4
2.2 Photograph of the Excavation of South Process Pond Pit #2 ..... 2.5
2.3 Relationship Between Total Uranium and Total Copper in Vadose Zone Sediment Beneath the North and South Process Ponds 2.6
2.4 Backscattered Electron Image of the Sectioned Sample NP4-1 ..... 2.16
2.5 Elemental Abundance Maps from the Large, Cracked Clast in Figure 2.4, for Uranium and Copper 2.17
2.6 Bulk XANES Spectra for Copper from NP and NPP Samples, Relative to Indicated Standard 2.17
2.7 Spot XANES Spectra for Uranium from Sample NP1-4.5, Relative to Indicated Standards 2.18
2.8 Backscattered Electron Image of Sample NP4-1, Showing a Carbonate Rhomb Imbedded in Fine-Grained Matrix, and Fine, Micrometer-Scale Inclusions of a Uranium-Rich Phase 2.18
2.9 Surfaces of Clasts from Process Pond Sediment and from the Sediments Beneath the Ponds, Coated with Secondary Mineralization 2.19
2.10 Elemental Abundance Maps for Aluminum, Silicon, Copper, and Uranium for Sample NPP2-4 ..... 2.19
2.11 Backscattered Electron Image and Abundance Maps for a Portion of the Area Shown in Figure 2.9, Overlain by XMP Abundance Maps for Uranium and Copper 2.20
2.12 XANES Spectra of Different Uranium-Containing Spots in NPP2-0.5 Showing No Evidence for U(IV) 2.20
2.13 Micro-XRF Map of the Distribution of Uranium and Copper 2.21
2.14 Uranium LIII Edge EXAFS Spectra and Corresponding FT Spectra from Selected Spots in Figure 2.13 ..... 2.21
2.15 Micro-XRF Map of Same Area as Figure 2.13 with Image Analysis and Diffuse Uranium Precipitate 2.22
2.16 Normalized X-ray Absorption Near-Edge Spectra Collected at Selected Diffuse Uranium Areas in Figure 2.15 ..... 2.22

2.17 LHeT Fluorescence Spectra of 300 Area North Process Pond Sediments and Underlying Vadose Zone Sediments at Different Depths 2.26

2.18 Deconvolution of the LHeT Time-Resolved Fluorescence Spectra of the Uranium-Rich Natural Calcite at a Delay Time of 1 ms into Two Unique Spectral Components A and B 2.27

2.19 Deconvolution of the LHeT Time-Resolved Fluorescence Spectra of NP4-1 and Uranium-Rich Natural Calcite 2.28

2.20 Deconvolution of the LHeT Time-Resolved Fluorescence Spectra of NP1-6 into Two Unique Spectral Components A and B or Three Spectral Components 2.29

2.21 LHeT Fluorescence Spectra of 300 Area North Process Pond Groundwater Fines Along with that of Uranium Sorbed on Illite 2.30

2.22 U(VI) Undergoing Isotopic Exchange Between the Aqueous and Solid Phases in Artificial GW4 Containing ^{233}U for Sediment Sample NPP 1-16 ..... 2.36

2.23 U(VI) and Calcium Released During Dilute Bicarbonate Extraction of Sediment Sample, NPP 1-16 ..... 2.36

2.24 Aqueous Concentrations of Selected Elements During Formate Buffer Extraction of Sediment Sample, NPP 1-16 ..... 2.37

2.25 U(VI) Desorption from Sediment Sample, NPP 1-16, During Equilibration with Artificial Groundwater of Varying Alkalinity 2.37

2.26 Dependence of the Log of the U(VI) Sorption K_d Value on Alkalinity for Samples, NPP 1-16 and SPP 2-18, When Equilibrated in Artificial Groundwater of Varying Composition 2.38

2.27 U(VI) Adsorption Isotherms for NPP and SPP Sediment Samples Suspended in AGW4 and AGW9. ..... 2.38

2.28 Saturated Column Desorption Data for SPP2-18 at Two Different Fluid Residence Times and Adsorption and Desorption of Injected U(VI) 2.54

2.29 Saturated Column Desorption Data for NPP1-16 at a Fluid Residence Time of 1.32 hours and Adsorption of Injected U(VI) 2.55

2.30 Unsaturated Leaching of U(VI) from Sediments SPP2-18 at 30% Water Saturation and 4-hour Fluid Residence Time and NPP1-16 at 45% Water Saturation and 3-Hour Fluid Residence Time 2.56

2.31 Unsaturated Leaching of U(VI) from Sediments SPP2-18 at 21% Water Saturation and 5-Hour Fluid Residence Time and NPP1-16 at 33% Water Saturation and 4-Hour Fluid Residence Time 2.57

2.32 Comparison of U(VI) Leaching from the SPP2-18 Sediment at 30% and 21% Water Saturation 2.58

2.33 Unsaturated Leaching of U(VI) from Sediments SPP2-18 at 30% Water Saturation and 4-Hour Fluid Residence Time and NPP1-16 at 45% Water Saturation and 3-Hour Fluid Residence Time 2.59

2.34 Unsaturated Leaching of U(VI) from Sediments SPP2-18 at 21% Water Saturation and 5-Hour Fluid Residence Time and NPP1-16 at 33% Water Saturation and 4-Hour Fluid Residence Time 2.60
2.35 Location Map Showing 300 Area in Vicinity of Simulated Cross Section 2.64
2.36 EarthVision Geology for 300 Area Vertical Two-Dimensional Cross Section and Representative Water Levels 2.65
2.37 Discretized Geology and STOMP Boundary Condition Types for Two-Dimensional Flow Model 2.65
2.38 Hydraulic Head at River and Well 399-6-1 ..... 2.66
2.39 Darcy Velocity Vectors at End of Simulation for Hourly Boundary Conditions 2.66
2.40 Hourly Hydraulic Head Boundary Conditions During November 21, 2004 ..... 2.67
2.41 Hourly X-Direction Darcy Velocity for Near-Shore Region During First Half of November 21, 1992 ..... 2.67
2.42 Hourly X-Direction Darcy Velocity for Near-Shore Region During Second Half of 11/21/92 ..... 2.68
2.43 Comparison of Simulated Water and Tracer Fluxes for Different Boundary Condition Timescales 2.69
2.44 River Water Tracer Concentrations at End of Simulation with Hourly, Daily, and Monthly Boundary Conditions 2.70
2.45 Observed Heads at Well 399-3-12 and Interpolated Simulated Heads at the Same Easting Along the Model Cross Section 2.71
2.46 Base Case: River Water Mixing Zone in Aquifer After 1 Year of Simulation 2.71
2.47 Sensitivity Case: River Water Mixing Zone in Aquifer After 1 Year of Simulation with Additional 11.3-cm Drop in River Stage 2.72
2.48 Comparison of Water Flux into River for Base Case and Sensitivity Case 2.73
2.49 Recharge-Driven Transport of Uranium Leached from 30 nmol/g Contaminated Vadose Zone Sediments 2.78
2.50 Recharge-Driven Transport of Uranium Leached from 3,000 nmol/g Contaminated Vadose Zone Sediments 2.79
2.51 Recharge-Driven Transport of Uranium Leached from 30 nmol/g Contaminated Vadose Zone Sediments Under Groundwater Chemistry from Well 399-8-3 ..... 2.79
2.52 Recharge-Driven Transport of Uranium Leached from 30 nmol/g Contaminated Vadose Zone Sediments Under Groundwater Chemistry from Laboratory Composition 2.80
2.53 Uranium Leached from 30 nmol/g Contaminated Sediments by Groundwater from Well 399-8-3 ..... 2.84
2.54 Uranium Leached from 30 nmol/g Contaminated Sediments by Laboratory Composition Artificial Groundwater 2.85
2.55 Sequence of 4 Days Loading and 1 Day Unloading of Sites Using Groundwater Composition from Well 399-8-3 ..... 2.85

Tables

2.1 Total Analyses of Historical 300 Area Process Pond Sediment by X-Ray Fluorescence and pH Measurement 2.7

2.2 Particle Size Distribution and Uranium Concentrations in Sediment Samples 2.7

2.3 Total Uranium Concentrations in 300 Area Sediment and Groundwater Fines Measured by X-Ray Fluorescence 2.8

2.4 Total and Labile Uranium Concentrations in 300 Area Sediment Samples Collected in Spring 2003 ..... 2.9

2.5 Composition of 300 Area Groundwater Collected from Various Excavations, February through April 2003 ..... 2.10

2.6 Uranium Extraction and Total Uranium 2.39

2.7 Composition of Artificial Hanford Groundwater, $pCO_{2(g)} = 10^{-3.5}$ 2.40

2.8 Comparison of U(VI) Extraction Techniques 2.41

2.9 Extractable Iron 2.42

2.10 Comparison of U(VI) Solubilized by Iron Extraction 2.42

2.11 U(VI) Surface Reactions Considered in the Semi-Empirical, Generalized Composite Surface Complexation Models 2.43

2.12 Distributed Rate Model Parameters for Modeling Bromine and Uranium Desorption Breakthrough Curves 2.51

2.13 Distributed Rate Model Parameters for Modeling Uranium Adsorption and Desorption in Short-Term Contaminated Sediments 2.52

2.14 Distributed Rate Model Parameters for Modeling Unsaturated Uranium Desorption Breakthrough Curves 2.53

2.15 Key Material Properties for STOMP Simulations 2.74

2.16 Sediment Size Distribution for NPP-1, 4.3 m Below Ground Surface 2.80

2.17 Unsaturated Flow Parameters for Hanford Unit Sediments 2.81

2.18 Solution Compositions Tested in the Multi-Component Surface Complexation Model 2.81

2.19 Sediment Size Distribution for NPP-1, 4.3 m Below Ground Surface 2.86

2.20 Water Composition for the River, Groundwater, and Laboratory Solution 2.86

1.0 Introduction

The Hanford Site, a U.S. Department of Energy (DOE) complex, encompasses ~1,517 square kilometers northwest of the city of Richland along the Columbia River in southeast Washington State. The site was acquired by the federal government in 1943, and until the 1980s was dedicated primarily to the production of plutonium for national defense and the management of resulting waste. Today DOE is engaged in a mission to cleanup the Hanford Site.

A portion of the site characterization and cleanup effort focuses on the 300-FF-5 Operable Unit, located in the southeast portion of the Hanford Site (Figure 1.1). The 300-FF-5 Operable Unit includes groundwater affected by contaminants released from waste sites in the 300 Area and north of the 300 Area. The 300 Area contains former nuclear fuel fabrication facilities, fuel research laboratories, liquid effluent disposal sites (e.g., process trenches, process ponds), and several solid waste burial grounds. Uranium is the contaminant of concern of greatest significance in groundwater at this operable unit (Hartman et al. 2004).

In 1996, a record of decision (ROD 1996) for the 300-FF-5 Operable Unit was issued that specified an interim remedy as continued monitoring of groundwater and institutional controls to restrict groundwater use. The interim record of decision was based on a remedial investigation that suggested levels of uranium would decrease with time because of natural geochemical and hydrologic processes. A predicttion was made that concentrations of uranium would decrease to the proposed drinking water standard or lower (20 µg/L) in 3 to 10 years from 1993. This prediction has not been realized, prompting investigations and update of the conceptual model for uranium in the 300 Area.

In June 2002, DOE Richland Operations asked scientists on the Pacific Northwest National Laboratory's Remediation and Closure Science (RCS) Project, to begin research on the 300 Area uranium plume in collaboration with a small team of project investigators from DOE's Environmental Management Science Program. This work done by the RCS Project, and summarized in this report, is being used to improve the conceptual model of the 300 Area uranium plume and develop a final record of decision for the 300-FF-5 Operable Unit.

The primary objectives of research conducted by the RCS Project to support the 300-FF-5 record of decision are threefold:

1. To update the conceptual model of uranium release/flux rates from the vadose zone and the migration velocity/desorption rate of uranium contamination in the aquifer by investigating the linked geochemical and hydrologic phenomena that govern those processes.

2. To identify a geochemical reaction network that is responsible for uranium retardation in the vadose zone and groundwater, and describe the parameters of the reaction network in terms of thermodynamic and kinetic (chemical, mass transfer) variables.

3. To integrate the conceptual model and reaction network into reactive transport simulations to evaluate vadose zone and capillary fringe fluxes and to forecast the future evolution of the uranium plume.

Significant progress has been made on the research that is summarized in this report. A first phase of research was scheduled for completion by March 2005 in time to contribute directly to the *Comprehensive Environmental Response, Compensation, and Liability Act* (CERCLA) 5-year review and plans for updating the 300-FF-5 record of decision (ROD 1996). A second research phase will continue into fiscal year (FY) 2006 and will involve more detailed data evaluations and the testing of alternative process-level models, evaluation of more extensive future scenarios, and publication of research findings in peer review journals. Selected scientific progress will be described in the text that follows for eight different subject categories (Chapter 2). The report also describes an integrated, but preliminary, conceptual model (Chapter 3) for the coupled vadose zone aquifer system and its implications to the future behavior of uranium in the 300-FF-5 plume.

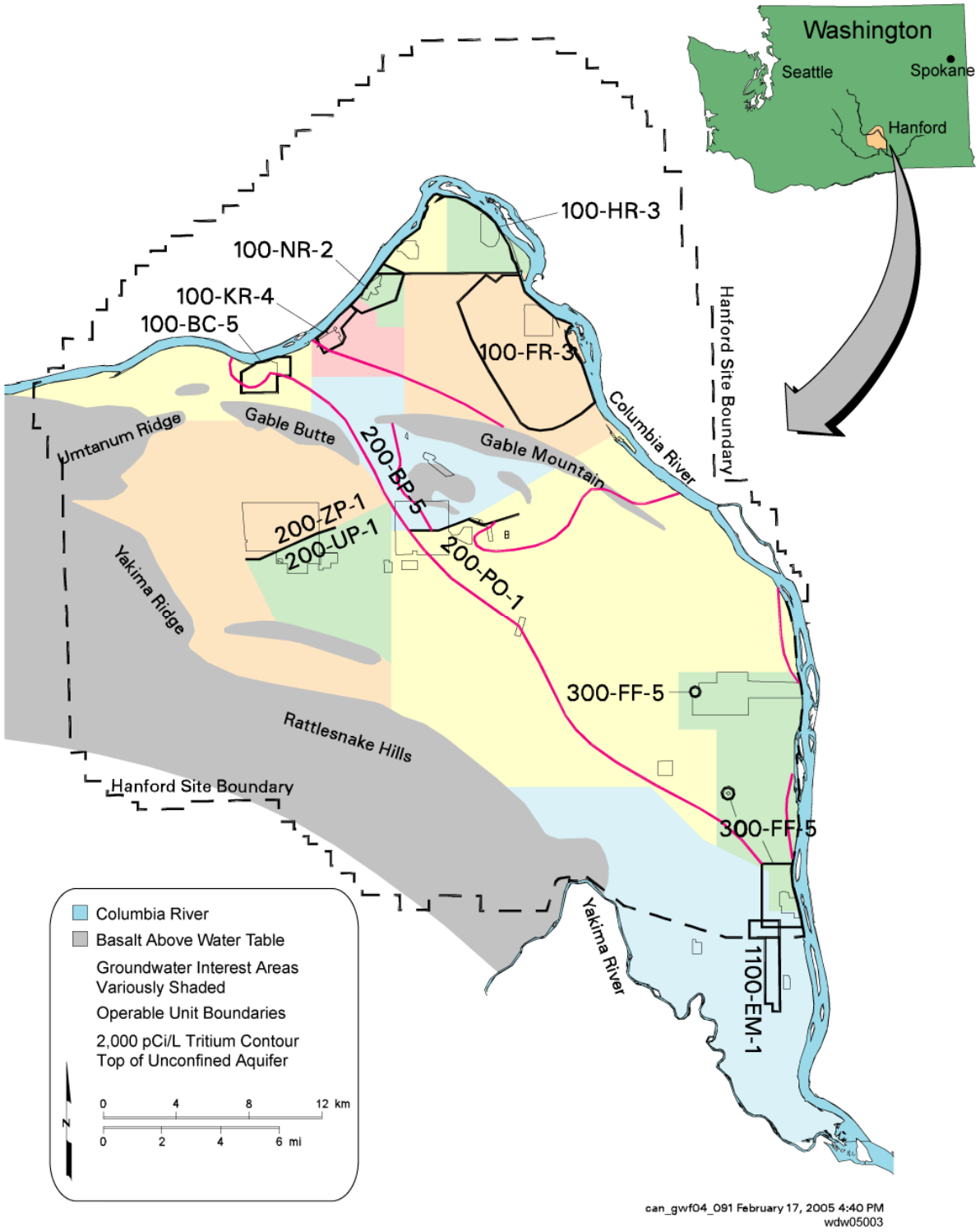

Figure 1.1. 300-FF-5 Operable Unit is Located in the Southeast Part of the Hanford Site

2.0 Scientific Findings

2.1 Sampling and Characterization

PNNL staff collaborated with Bechtel personnel in February through May 2003 to collect subsurface sediment and groundwater samples from the north process pond (NPP) and south process pond (SPP) using an excavator. The locations of these four excavations are shown in Figure 2.1. The existing land surface in April 2003 in both ponds was below grade as "contaminated" materials had been excavated and hauled to the Environmental Restoration Disposal Facility on the Central Plateau of the Hanford Site. Subsurface sediment samples were collected in approximate 0.6-m-depth intervals from the ground surface to the saturated zone (e.g., Figure 2.2). Groundwater and the entrained silt/clay sized fines were sampled at each location.

Three historical samples (NP4-1, NP4-2, NP1-4.5) that were collected in 1991 from the top 2 m of the NPP prior to its excavation were also obtained for evaluation. These materials had very high uranium and copper concentrations (Table 2.1) and represent the contaminated materials that were excavated during source term removal.

2.1.1 Results

The sediments were quite coarse in texture (e.g., Table 2.2), and contained significant mass percent of river cobble. Samples of each sediment were sieved to <2 mm. All of the sieved samples and groundwater fines were analyzed for their total uranium, copper, and trace metal content (Table 2.3) by x-ray fluorescence. Labile, sorbed hexavalent uranium [U(VI)] was measured by a bicarbonate extraction. Groundwater was analyzed comprehensively for anions, cations, pH, and other relevant variables. Solid phase inorganic carbon and extractable iron forms (dithionite citrate bicarbonate [DCB], and acid ammonium oxalate [AAO]) was measured on all sieved samples. The mineralogy of the silt and clay sized fractions (<63 μm) of four sediment samples was determined after manganese, potassium, and glycol solvation and heating. Mica, chlorite (ferroan chlinochlore), vermiculite, and smectite along with quartz and feldspars, were dominant mineral forms in the silt and clay fractions. Many other specialized analyses were performed that are described in the following sections.

Generally, total uranium concentrations were at or below detection in the size fraction ranging from 2.0 to >12.5 mm (Table 2.2). Cobbles up to 100 mm in size were common. To further investigate whether sorbed uranium was present in the larger size fractions, five fractured river cobbles varying in approximate size from 25 to 75 mm were thin sectioned and subjected to x-ray microbe measurements for uranium at the PNC-CAT beamline at the advanced photon source. Fracture channels were interrogated as were domains with significant internal porosity. No appreciable regions of uranium accumulation were found in any of the five samples (data not shown). Because of this apparent localization of sorbed uranium in the fines fraction of the sediment, all subsequent studies were performed with the <2.0 mm size fraction that was isolated by dry sieving.

The total uranium concentration in the <2.0 sediments was highly variable, with generally greater sorbed concentrations found in vadose zone sediment from the NPP (Table 2.3). All sediment samples contained uranium concentrations that were above background (1.5 to 3.0 mg/kg). Sediments with the highest uranium (and copper) concentrations exhibited a pale-green hue from precipitated copper. The concentrations of sorbed uranium and copper showed some correlation (Figure 2.3). Generally, sorbed uranium was highest in the finer textured mineral components of the sediment (e.g., silt and clay; Table 2.2) because of its higher surface area and presence of more reactive mineral components. Fine grained mineral material isolated from the groundwater contained relatively high concentrations of sorbed uranium that showed mild correlation with groundwater concentration. A variable fraction of sorbed uranium was found to be labile in the different sediments using a bicarbonate extraction (Table 2.4). The labile fraction is considered the portion of the total uranium pool that is available to desorb or dissolve into pore or groundwater. The labile sorbed fraction was quite low for the pond sediments (NP series; 4.2 to 8.1%), and higher for the deeper vadose zone materials (NPP and SPP series; approximately 8 to 67%). In no case was the sorbed U(VI) fraction found to be fully labile. Complementary lability measurements by isotopic exchange are presented in Section 2.4.

The composition of the groundwater that was collected at seven locations within the plume region was relatively constant in terms of its major cation and anion composition (Table 2.5). The groundwater exhibited pH near 8, ionic strengths of 3 to 8 mmol/L, and were dominated in composition by Ca^{2+}, Na^{+}, Mg^{2+}/HCO_3^{-}, SO_4^{2-}. Uranium concentrations varied between sampling points. The analytical data was input to a computerized speciation code (MINTEQA2; Allison et al. 1992) that contained a comprehensive thermodynamic data base for uranium aqueous species and solid phases, and other aqueous complexes and solids that are important at the Hanford Site. The calculations indicated that 300 Area groundwater was supersaturated with $CO_2(g)$ ($pCO_{2(g)} \approx$-2.6 to -3.1 atm), in equilibrium with calcite, and contained $Ca_2UO_2(CO_3)_3$ as the predominant U(VI) species (70 to 92%). The other important U(VI) aqueous species was $UO_2(CO_3)_2^{2-}$. Because the groundwater was supersaturated with $CO_2(g)$, the pH increased from approximately 7.8 to 8.2-8.4 when samples were allowed to equilibrate (degas) in contact with the atmosphere.

2.1.2 Synopsis and Implications

Samples of historical pond sediment, deep vadose zone sediment, aquifer fines, and groundwater were obtained for laboratory studies needed to define an improved hydrogeochemical model of the 300 Area uranium plume.

- The historical samples contained high levels of uranium (1,880 to 3,310 mg/kg) and copper, while excavated vadose zone materials contained from <5 mg/kg to a high of 238 mg/kg. The highest concentrations of residual uranium were found in the southwest corner of the NPP. No trends were observed in residual, sorbed uranium concentrations in the vadose zone below the process ponds. The groundwater fines contained from 12.7 to 200 mg/kg of sorbed uranium.

- The vadose zone and aquifer sediments were extremely coarse. Approximately 75% of their mass was rounded river cobble >12.5 mm in size. Sorbed uranium existed in the fines fraction (silt and clay) that represented <2% to 6% of the total sediment mass depending on sample location and depth.

- The groundwater samples were mixed sodium, calcium, and magnesium electrolytes with a pH range of 7.71 to 8.11 and a HCO_3 concentration range of 1.20 to 2.71 µmol/L. The groundwater samples were in equilibrium with calcite and $pCO_{2(g)}$ pressures of -2.56 to -3.03 atm. The groundwater samples degassed after collection, and their pH increased unless they were stored in a sealed container.

- U(VI) concentrations in groundwater sampled from the excavation pit bottoms ranged from 0.30 to 4.96 µmol/L (7.14 to 118 µg/L) and the predominant aqueous species was $Ca_2UO_2(CO_3)_3^0$.

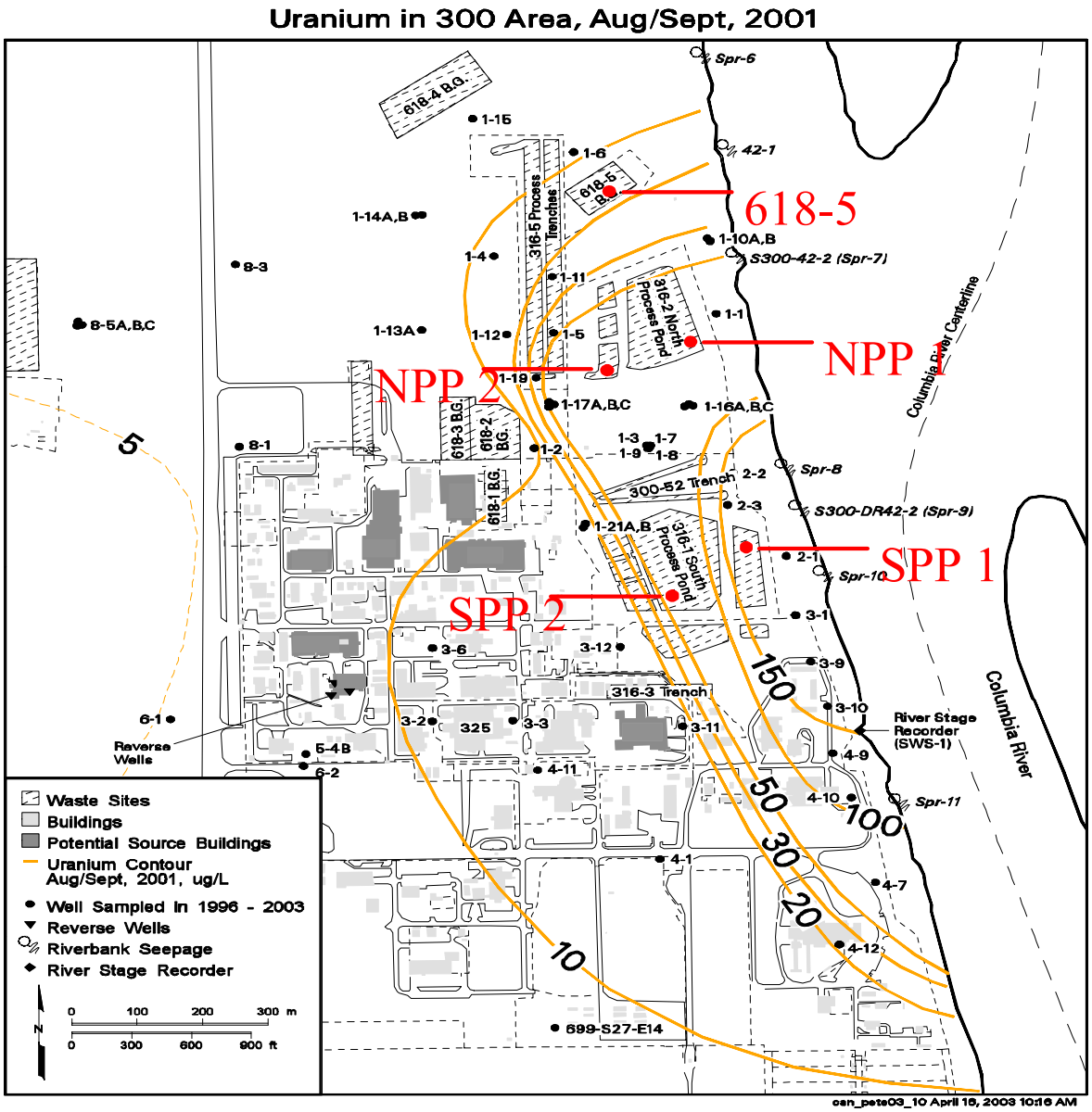

Figure 2.1. Map of the 300 Area (Contour lines for the uranium plume, location of north and south process ponds, and locations of four excavations where vadose zone and aquifer sediments were collected.)

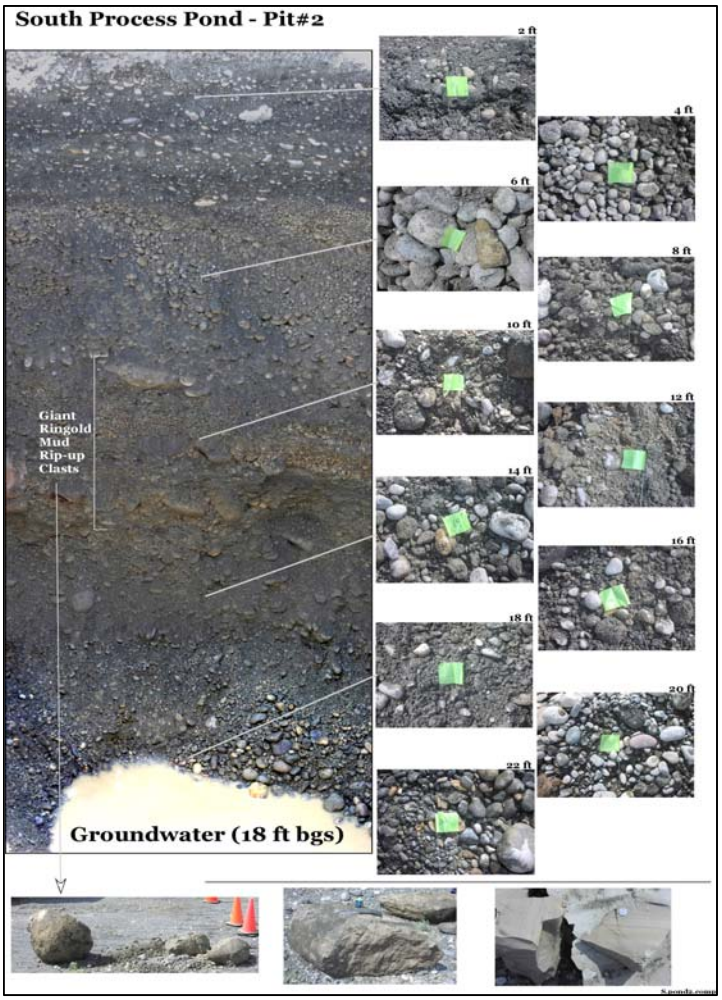

Figure 2.2. Photograph of the Excavation of South Process Pond Pit #2. (Note the subsurface structure, variation in color, and coarse textured, cobble nature of the sediments. One of the sediments that was comprehensively studied (SPP2-18) was collected immediately above the groundwater. Fine-grained materials were released to and suspended within groundwater during excavation. These were isolated by filtration and are labeled as "groundwater fines" throughout the report.)

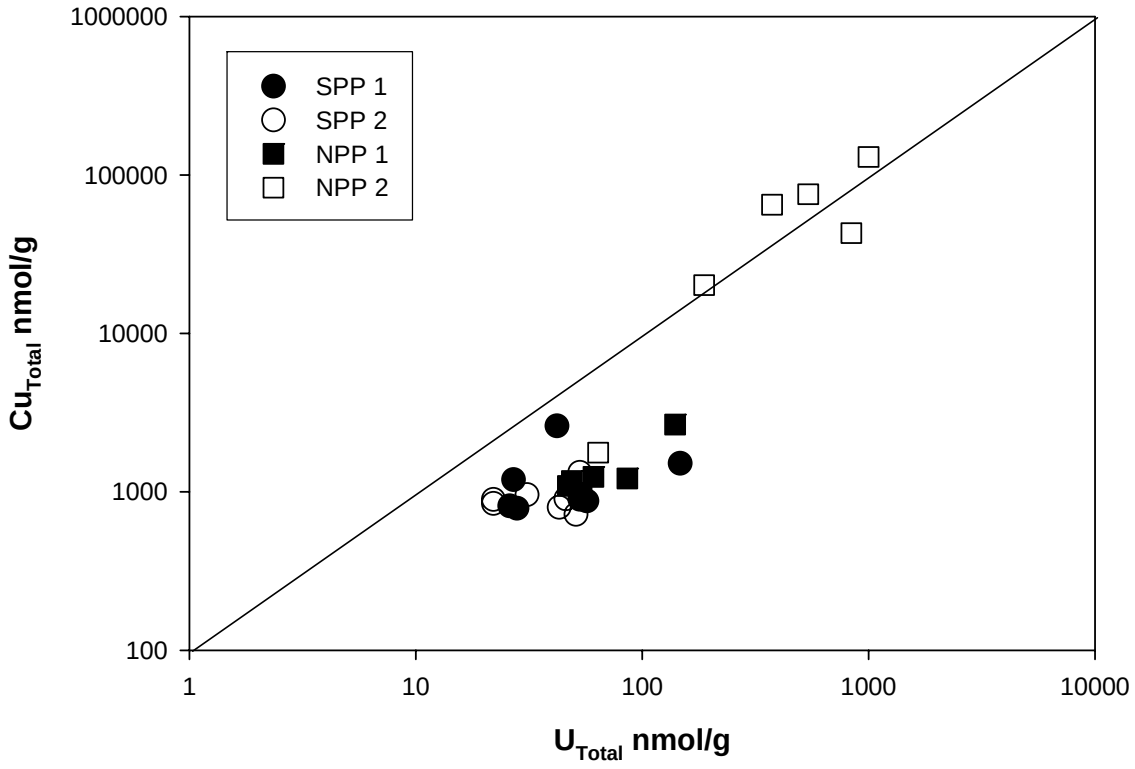

Figure 2.3. Relationship Between Total Uranium and Total Copper in Vadose Zone Sediment Beneath the North and South Process Ponds

Table 2.1. Total Analyses of Historical 300 Area Process Pond Sediment by X-Ray Fluorescence and pH Measurement

Sediment ID	Al (%)	Si (%)	P (%)	K (%)	Ca (%)	Fe (%)	U (µg/g)	Cu (µg/g)	pH[(a)] (1:1)
NP1-4.5	8.79	16.6	0.52	0.67	6.00	3.27	1,880	32,400	7.98
NP1-6	10.4	24.4	0.30	1.21	4.93	7.86	390.0	5,540	8.07
NP4-1	13.8	14.7	0.72	0.61	4.73	4.00	3,310	13,960	8.33
NP4-2	10.3	9.74	0.34	0.39	10.6	2.28	2,390	4,940	8.52
Background	0.99		6.7×10^{-5}	0.16	0.78	2.76		18.4	
(a) Average of two replicates.									

Table 2.2. Particle Size Distribution and Uranium Concentrations in Sediment Samples

Size Range (mm)	Mass Distribution (%)	U_{Total} (nmol/g)
Cobbles		
>12.5	74.5	<22
2.0-12.5	17.2	<19
Sand		
1.0-2.0	2.64	26
0.5-1.0	2.34	<18
0.25-0.5	0.78	<21
0.149-0.25	0.33	37
0.106-0.149	0.19	<23
0.053-0.149	0.20	<23
Silt + Clay		
<0.053	1.78	125

Table 2.3. Total Uranium Concentrations in 300 Area Sediment and Groundwater Fines Measured by X-Ray Fluorescence

Solid Phase [U] in <2 mm size fraction or groundwater fines											
South Process Pond Pit #1		South Process Pond Pit #2		North Process Pond Pit #1		North Process Pond Pit #2		618-5 Pit #1		618-5 Pit #2	
Depth (ft bgs)	Solid Phase [U] (mg/kg by XRF)	Depth (ft bgs)	Solid Phase [U] (mg/kg by XRF)	Depth (ft bgs)	Solid Phase [U] (mg/kg by XRF)	Depth (ft bgs)	Solid Phase [U] (mg/kg by XRF)	Depth (ft bgs)	Solid Phase [U] (mg/kg by XRF)	Depth (ft bgs)	Solid Phase [U] (mg/kg by XRF)
4	9.9	4	7.3 ± 3.3	4	14.4 ± 2.8	0.5	238 ± 12	8	6.6 ± 2.6	8	<4.9
8	<6.5	8	11.0 ± 3.3	8	12.9 ± 2.7	2	89.2 ± 5.4				
12	6.7 ± 3.4	12	12.2 ± 2.7	12	20.5 ± 2.9	4	138± 7.5	GW fines	15.7 ± 3.2		
16	13.6 ± 3.3	16	<5.3	16	11.1 ± 2.9	8	44.7 ± 3.5				
18	12.5 ± 3.2	18	<5.4	20	11.2 ± 2.7	12	15.2 ± 2.7				
22	6.2 ± 2.7	22	10.2 ± 2.7								
GW fines	35.0 ± 4.2	GW fines	12.7 ± 3.4	GW fines	33.3 ± 3.7	GW fines	200 ± 11				
Groundwater [U] (ppb)											
	70.7 ± 1.2		84.8 ± 1.4[3]		71.4 ± 1.4		247.3 ± 4.8[5]		1,181		433
	69.8		84.0 [4]						1,190 ± 22.9[6]		418.3 ± 8.2
									129.0 ± 1.7		

Table 2.4. Total and Labile Uranium Concentrations in 300 Area Sediment Samples Collected in Spring 2003

Sediment	m bgs	U (mg/kg)	Total U (mol/g)	Labile U (mol/g)	% Labile	
SPP Pit 1-4	1.2	9.9	4.16×10^{-8}	1.01×10^{-8}	24.2	
SPP Pit 1-8	2.4	<6.5	$<2.73 \times 10^{-8}$	4.77×10^{-9}	>17.5	
SPP Pit 1-12	3.6	6.7	2.82×10^{-8}	8.80×10^{-9}	31.3	
SPP Pit 1-16	4.9	13.6	5.71×10^{-8}	1.87×10^{-8}	32.7	(a)
SPP Pit 1-18	5.5	12.5	5.25×10^{-8}	1.36×10^{-8}	26.0	(a)
SPP Pit 1-22	6.7	6.2	2.61×10^{-8}	1.36×10^{-8}	52.1	(a)
SPP Pit 1, GW Fines		35	1.47×10^{-7}	7.79×10^{-8}	52.9	(a)
SPP Pit 2-4	1.2	7.3	3.07×10^{-8}	1.29×10^{-8}	41.9	
SPP Pit 2-8	2.4	11	4.62×10^{-8}	2.37×10^{-8}	51.3	(a)
SPP Pit 2-12	3.6	12.2	5.13×10^{-8}	2.24×10^{-8}	43.7	(a)
SPP Pit 2-16	4.9	<5.3	$<2.23 \times 10^{-8}$	8.00×10^{-9}	>35.9	(a)
SPP Pit 2-18	5.5	<5.4	$<2.27 \times 10^{-8}$	2.68×10^{-9}	>9.9	(a, b)
SPP Pit 2-22	6.7	10.2	4.29×10^{-8}	3.50×10^{-9}	8.2	
SPP Pit 2, GW Fines		12.7	5.34×10^{-8}	2.79×10^{-8}	52.2	(a)
NPP Pit 1-4	1.2	14.4	6.05×10^{-8}	2.19×10^{-8}	36.1	
NPP Pit 1-8	2.4	12.9	5.42×10^{-8}	2.90×10^{-8}	53.6	(a)
NPP Pit 1-12	3.6	20.5	8.61×10^{-8}	3.26×10^{-8}	37.8	(a)
NPP Pit 1-16	4.9					
NPP Pit 1-18	5.5	11.6	4.87×10^{-8}	1.76×10^{-8}	36.1	(a, b)
NPP Pit 1-22	6.1	11.2	4.71×10^{-8}	1.02×10^{-8}	21.7	(a)
NPP Pit 1, GW Fines		33.3	1.40×10^{-7}	4.33×10^{-8}	30.9	(a)
NPP Pit 2-0.5	0.15	238	1.00×10^{-6}	2.04×10^{-7}	20.4	
NPP Pit 2-2	0.61	89.2	3.75×10^{-7}	1.76×10^{-7}	47.0	(a)
NPP Pit 2-4	1.2	128.9	5.42×10^{-7}	1.48×10^{-7}	27.3	(a)
NPP Pit 2-8	2.4	44.7	1.88×10^{-7}	8.25×10^{-8}	43.9	(a)
NPP Pit 2-12	3.6	15.2	6.39×10^{-8}	4.27×10^{-8}	66.9	(a)
NPP Pit 2, GW Fines		200	8.40×10^{-7}	2.11×10^{-7}	25.1	(a)
NP1-4.5	1.4	1,600	6.72×10^{-6}	5.46×10^{-7}	8.1	(c)
NP1-6	1.8	400	1.68×10^{-6}	7.03×10^{-8}	4.2	(c)
NP4-1	0.30	3,000	1.26×10^{-5}	9.92×10^{-7}	7.9	(c)
NP4-2	0.61	2,400	1.01×10^{-5}	7.84×10^{-7}	7.8	(c)

(a) Labile uranium data from Deb Bond, Jim Davis USGS, see Section 2.4.
(b) Large mass sample.
(c) Radioactive material.
bgs = Below ground surface.
GW = Groundwater.
NP = Historical samples collected from the base of the north process pond in 1991 before any excavation had occurred.
NPP = North process pond.
SPP – South process pond.

Table 2.5. Composition of 300 Area Groundwater Collected from Various Excavations, February through April 2003

	618-5 Pit 1 (26 Feb 03)	618-5 Pit 1 (29 May 03)	618-5 Pit 2 (26 Feb 03)	SPP Pit 1 (19 Apr 03)	SPP Pit 2 (19 Apr 03)	NPP Pit 1 (26 Apr 03)	NPP Pit 2 (26 Apr 03)	Range
pH	7.71	8.11	7.80	7.83	8.04	7.83	7.88	7.71-8.11
Ionic strength (mmol/L)	7.5	8.2	7.5	3.5	4.9	5.2	6.3	3.5-8.2
Cations (µmol/L)								
Ca	1.31	1.17	1.24	0.60	0.90	1.01	1.14	0.60-1.31
K	0.16	0.20	0.16	0.07	0.09	0.07	0.06	0.06-0.20
Mg	0.58	0.49	0.56	0.21	0.28	0.34	0.40	0.21-0.58
Na	1.34	2.65	1.53	0.77	0.95	0.84	1.14	0.77-2.65
Anions (mmol/L)								
Cl^-	0.84	1.21	0.76	0.14	0.36	0.36	0.39	0.14-1.21
NO_3^-	0.42	0.53	0.40	0.36	0.40	0.29	0.43	0.29-0.53
Inorg. C	2.47	2.71	2.41	1.20	1.70	2.02	1.58	1.20-2.71
SO_4^{2-}	0.69	0.76	0.85	0.35	0.43	0.47	0.88	0.35-0.88
Si_{Total}	0.57	0.59	0.55	0.28	0.39	0.32	0.23	0.23-0.59
U (µmol/L)	4.96	1.39	1.82	0.30	0.36	0.30	1.07	0.30-4.96
Species	(%)	(%)	(%)	(%)	(%)	(%)	(%)	
$UO_2(CO_3)_2^{2-}$	5.8	2.8	5.4	22.0	6.2	7.1	7.3	
$UO_2(CO_3)_3^{4-}$	3.5	5.0	4.0	6.5	4.7	4.0	3.9	
$Ca_2UO_2(CO_3)_3^0$	90.6	92.2	90.5	70.4	88.9	88.7	88.6	
$_PCO_{2(g)}$	-2.56	-2.91	-2.66	-2.97	-3.04	-2.75	-2.91	

2.2 Spatial Distribution of Uranium

Several samples that contained high concentrations of sorbed uranium (e.g., NP 4-1 [3,000 mg/kg uranium]; NP 1-4.5 [1,600 mg/kg uranium]; NPP2-0.5 [238 mg/kg uranium]; NPP2-4 [139 mg/kg uranium]) were subjected to detailed microscopic studies to identify the spatial locations within the sediment of the uranium and the chemical/mineralogical nature of the uranium-sediment association. The primary methods applied were scanning electron microscopy (SEM), x-ray microprobe (XMP), and electron microprobe (EMP). Samples of archived process pond waste (NP 4-1 and NP 1-4.5) and of sediment excavated from the vadose zone beneath the process ponds (NPP2-0.5 and NPP2-4) were imbedded in epoxy, wafered using a diamond saw, and prepared as 100-μm-thin sections on fused quartz slides. Individual whole clasts were also examined by picking them from unprocessed sediments.

For XMP analysis, measurements were made at the Argonne National Laboratory Advanced Photon Source within the Pacific Northwest Consortium Collaborative Access Team (PNC-CAT), and at the Lawrence Berkeley Laboratory Advanced Light Source (ALS) beam-line 7.3.3. The primary x-ray beam was focused using Kirkpatrick-Baez mirrors to a 6 to 10 μm diameter on the sample surface. The sample was oriented in a precision-translation stage at 45º to the x-ray beam, and the detectors were oriented normal to the beam. Uranium maps were obtained by monitoring the uranium M_α fluorescence line using a wavelength dispersive detector, and other elements were monitored using an energy dispersive detector. The detection limit was approximately 1 $\mu g\ g^{-1}$ for all elements, equivalent to approximately 10^9 atoms within the beam "spot." Fluorescence x-ray intensities were normalized to the ion chamber current generated by the primary x-ray beam at a flux of about 5×10^{11} ph /sec. X-ray absorption near-edge spectra (XANES) were collected using a focused beam after the spatial distributions of uranium and copper had been mapped; the incident energy was varied while monitoring the x-ray fluorescence. A silicon(111) double crystal monochromator was used with an energy resolution ($\Delta E/E$) of about 1.4×10^{-4}. Powdered rutherfordine (UO_2CO_3) and cuprous oxide (CuO) were used to calibrate the beam energy.

For EMP and SEM analysis, thin sections and individual clasts were carbon coated to make them electrically conductive. They were examined using a JEOL model 8200 EMP and a JEOL 6340f SEM, and images were collected using a backscattered electron detector for atomic number contrast. The detection limit for EMP was approximately 100 μg/g, and the optical resolution was 10 to 20 nm. Elemental abundance maps were collected on the EMP using wavelength-dispersive spectrometers tuned against uranium metal and CuO standards.

Color figures were constructed for XMP and EMP results using a natural, blue-to-red, false-color representation of elemental abundances, except where it was expedient to use a bicolor representation of copper and uranium abundances. The color scheme was modified for uranium abundances by EMP to include white at the high-abundance end of the spectrum. EMP, SEM, and XMP images were super-imposed using Adobe PhotoShop.

The combined methods provided imaging capabilities that revealed the occurrence of uranium and copper in waste from the disposal ponds and in the underlying sediment that was impacted by them. The XMP detected contaminant uranium and copper at low abundance, albeit at relatively low resolution. The

use of XANES collected using the focused x-ray beam provided information about the valence of uranium and copper. EMP analysis provided accessible, high-resolution images of minerals and mineral surfaces, and allowed imaging of elemental abundances, but at relatively high detection limits.

2.2.1 Results

Select results are presented in a following set of nine figures, progressing from process pond waste materials (samples numbered 'NP,' Figures 2.4 to 2.8) to deeper vadose zone sediments collected from beneath the North Process Pond (samples numbered 'NPP;' Figures 2.9 to 2.12).

An EMP backscattered electron image of pond waste (Figure 2.4) showed the relative abundance of waste precipitates. The precipitates were compositionally heterogeneous and consisted of agglomerations of fine-grained aluminosilicate-rich materials incorporating smaller pre-existing mineral fragments, visible in the figure as small inclusions. The precipitates were chemically heterogeneous, indicating that there were multiple precipitation events of episodic and chemically variable character. These would include the high-pH sodium-aluminate waste discharges that were reportedly made to the ponds. Individual precipitate clasts also showed internal structure, including compositional banding and what appeared to be desiccation cracks on clast interiors, such as those apparent in the large particle of Figure 2.4.

The chemical variations within single clasts with respect to the abundances of uranium and copper (Figure 2.5; the images were from the large clast in Figure 2.4) indicated that they were associated, but not correlated in their accumulation during precipitation. The large clast shown, and the smaller clasts surrounding it, did not have equivalent variations in copper and uranium concentration. Also, the clasts apparently formed through multiple precipitation events or from fluids of changing composition. This was particularly evident with respect to copper and produced precipitates with distinct zoned composition (as shown also in the subtle variation in brightness in Figure 2.4).

XANES analysis for copper indicated that it occurred only as Cu(II), Figure 2.6. The XANES spectrum is affected to some degree by the binding environment for the element of interest, and can be used to fingerprint the unknown phase by standard comparison. The spectra in Figure 2.6 were compiled by calibrating the beam energy to CuO; the similarity of the spectrum for that standard (dark red) to the spectra from the NP and NPP samples (particularly the absence of a 'pre-edge' feature at 0 volts) confirmed that Cu(II) was the only species in these samples. The spectra shown were from bulk (whole-sediment) analyses and were identical to representative spot measurements (not shown). XANES analysis for uranium, however, indicated non-uniformity in uranium valence (Figure 2.7). Compared to the spectra for U(VI) and U(IV) standards, the NP samples showed a mixture of uranium valences. This mixture was evident in XMP mode only; a bulk measurement of the same materials (not shown) indicated the presence only of U(VI). The abundance of U(IV) was thus inferred to be low relative to U(VI).

SEM analysis of broken, unsectioned, uranium-rich clasts indicated that the areas examined by XANES and shown to include U(IV) were most likely UO_2 disposed with the wastes sluiced into the ponds (Figure 2.8). Minute, fine-grained uranium precipitates were observed within the fine-grained aluminosilicate matrix. These inclusions were consistent with the bright inclusions observed in Figure 2.4, and the most-abundant, white areas within the uranium abundance map in Figure 2.5.

Calcium carbonate rhombs were also observed, imbedded in the aluminosilicate matrix (Figure 2.8). Calcite ($CaCO_3$) was observed as an abundant component of NP samples using XRD (not shown). The observation of pure-phase carbonate precipitates within the aluminosilicate matrix suggested that uranium may have been partially incorporated in that phase within the alkaline waste mixture. The indurated nature of the waste precipitates suggested also that they were cemented by carbonate minerals.

The NP samples contained a complex mixture of secondary precipitates from multiple waste-sediment reaction events that were admixed with typical Hanford formation lethic fragments. The occurrences of copper and uranium were parallel but not correlated in the sense that they were not co-precipitated from a liquid of uniform composition but were instead incorporated from liquids of varying composition over time. Microclasts from different precipitation events aggregated into larger clasts of widely variable waste composition. The aluminum and silicon components of the waste were apparently cemented by carbonate mineralization, which may have incorporated uranyl by co-precipitation. Fine inclusions of a uranium-rich phase, probably $UO_{2,}$,were present throughout the precipitated waste.

A comparison of the surfaces of process pond waste precipitates (e.g., NP4-1) with the surfaces of vadose zone sediment samples (e.g., SPP1-18) suggested that they were much the same (Figure 2.9). Although the subsurface sediment, in bulk, included only a fraction of the uranium and copper present in the process pond wastes, both sediments presented surfaces that were finely mottled, with faint indications of a composite texture, and the surfaces of each were composed of similar material.

The deeper vadose zone NPP sediment was almost entirely mineral clasts (Figure 2.10). The structured, variegated maps of silicon and aluminum showed the presence of lithic fragments, mostly the locally abundant basalts, but also of single minerals, such as quartz (shown in red on the silicon map). However, the maps also showed the presence of secondary rinds of precipitated material with an aluminosilicate component, apparent as a pale blue film on the aluminum map and as deeper blue on the silicon map. Calcium was also present in the rinds (not shown), suggesting they included carbonate cement (the epoxy imbedding material precluded analysis for carbon). Since copper was not an abundant component of the natural sediment, the secondary rind was readily apparent in a copper abundance map. Also, relatively rare precipitates similar to those observed in waste precipitate NP samples were present (green arrow, Figure 2.10). These were zoned with respect to silicon, aluminum, and copper abundances.

Uranium occurred as minute inclusions within the precipitated rind (red arrows, Figure 2.10). Copper and uranium were each present at abundances near the detection limit for EMP. The uranium abundances, in particular, were near the detection limit during mapping, and the false-color mineral background away from uranium-rich inclusions was mottled deep blue due to low-abundance inaccuracies in uranium detection. A portion of the area shown in Figure 2.10 was imaged in backscattered electron mode, and overlain with EMP and XMP abundance maps for uranium and copper (Figure 2.11). The backscattered electron image clearly showed the relatively low-Z secondary precipitate rind on the mineral clasts and the presence of similarly composed precipitates. Bright uranium-rich inclusions were visible within the rind. The overlay for copper indicated its presence within the rinds, and also its incorporation as a relatively abundant component of the precipitates. The overlay for uranium revealed abundant inclusions of a uranium-rich phase, which were more evident than within the EMP overlay because the energetic XMP beam could penetrate the sample surface more deeply. Lower abundances of uranium were also present within the precipitated material.

Spectral analysis of uranium within the precipitate rind and within uranium 'hot spots' (Figure 2.12) indicated that it was present only as U(VI), consistent with bulk measurements (not shown). The uranium inclusions were apparently either microprecipitates of U(IV), e.g., UO_2, that were advected with the waste fluids into the underlying sediment, then oxidized in place; or they were secondary precipitates that formed after oxidation, dissolution, and infiltration.

Uranium and copper in sample NPP2-4 were examined in detail using XMP methods to determine the relationship between phases for which they were components alone or in combination. A 3 by 3 mm bicolor combination map for uranium and copper (Figure 2.13) was drawn with uranium represented in red and copper in green. The image was scaled to show uranium occurrence in relatively high concentrations and low-level uranium concentrations were not observable. Uranium occurred within precipitates without copper (deep red) and copper within precipitates without uranium (bright green), but they also occurred together in a single phase (orange). The copper-uranium precipitates occurred broadly within the sample, with diameters of 1 to 10 μm. Uranium L_{III} edge micro-EXAFS (Figure 2.14, where spot numbers correspond to labels in Figure 2.13) were collected, and two of the spectra were well-fit with modeled metatorbernite [$Cu(UO_2)_2(PO_4)_2 \cdot 8(H_2O)$] (Finch and Murakami 1999); other spectra were less distinct. Diffraction patterns from micro-XRD (not shown) were also consistent with the presence of metatorbernite.

The distribution of uranium within the samples was evaluated using a 'phase analysis' approach from uranium-copper x-ray intensities (not shown). The incorporation within the bicolor copper-uranium image of an additional, low-concentration uranium component (Figure 2.15, gray) indicated that a diffuse uranium component, observed in XMP and EMP maps, was present within discrete clasts and on clast surfaces. Micro-XANES analyses of diffuse-uranium areas (Figure 2.13) showed that the uranium occurred as U(VI), and principal component analysis of the XANES spectra (not shown) suggested uranium occurred as a significant surface (sorbed) species. Micro-XRD measurements suggested that the diffuse-uranium areas did not include $CaCO_3$ above the level of detection.

2.2.2 Synopsis and Implications

The following is a synopsis of investigating the spatial distribution of uranium and the implications:

- Detailed microscopic studies were performed on historical pond sediments with high uranium concentration (NP4-1 and NP1-4.5) and vadose zone sediments from the NPP pit #2. The objective of these measurements was to define uranium valence, the spatial distribution of uranium at the millimeter-to-micron scale, and the mineral phases to which uranium was associated.

- The concentrations of copper and uranium correlated with one another in all pond and vadose zone sediment studied. The valence state of uranium was U(VI) and that of copper was Cu(II). These two elements were closely associated at spatial scales of 0.010 to 0.100 mm but not at the molecular scale, i.e., they were generally not co-precipitated with one another.

- The pond sediment samples contained millimeter-size domains of secondary, fine-grained aluminosilicate precipitates possibly resulting from known high pH sodium-aluminate discharges to the ponds. Minute fine-grained U(VI) precipitates were observed within the aluminosilicate

precipitates that also appeared to be cemented or indurated by $CaCO_3$ precipitates. The zoning in copper concentration within these precipitates indicated multiple precipitation events.

- Deeper vadose zone sediments contained thin (10 to 50 μm), precipitated rinds of secondary materials on mineral grains and lithic fragments resulting from waste discharge and migration from the ponds. The rinds appeared to be composed of calcite-indurated aluminosilicates, and were readily imaged by their copper content. Both Cu(II) and U(VI) were localized in these rinds as minute inclusions.

- Detailed analysis of one vadose sample (NPP2-4) indicated that uranium occurred in two or three modes: as micrometer-scale precipitates of metatorbernite [$Cu(UO_2)_2(PO_4)_2 \cdot 8(H_2O)$]; as more diffuse uranium incorporated in aluminosilicate rinds, perhaps co-precipitated within $CaCO_3$cement; and perhaps as a significant sorbed component on aluminosilicate minerals.

- The widespread, multiphase distribution of U(VI) within fine-grained, calcite-cemented aluminosilicate precipitates and particle coatings resulting from multiple waste reaction events will greatly retard the rate and extent of sorbed U(VI) release to vadose zone pore water or groundwater.

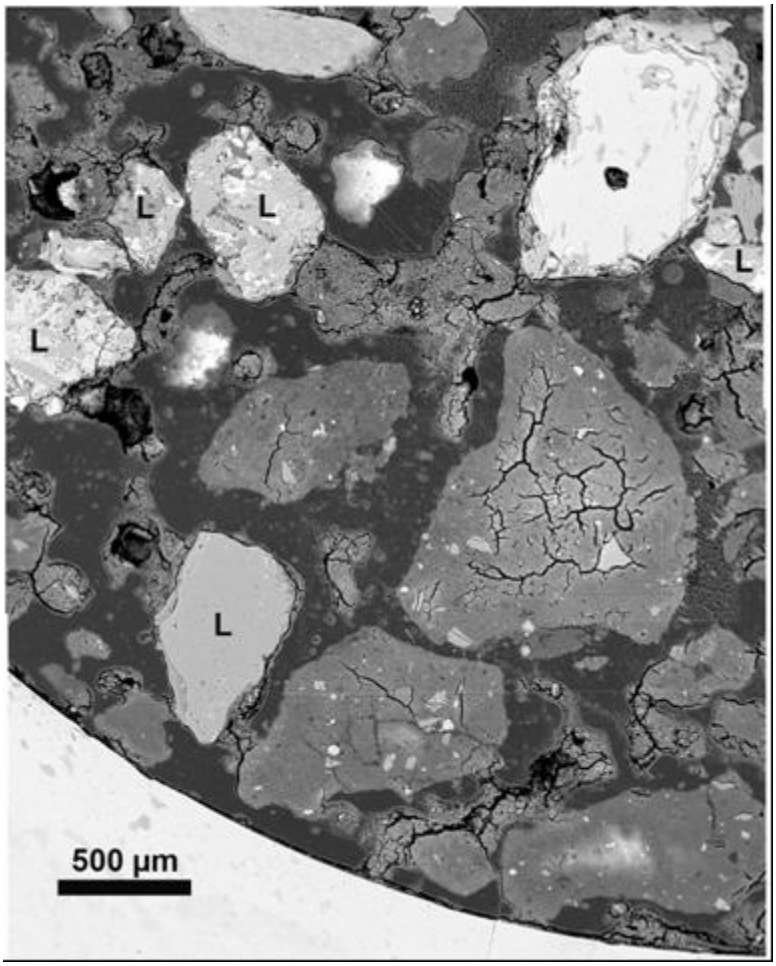

Figure 2.4. Backscattered Electron Image (EMP) of the Sectioned Sample NP4-1. (Lithic clasts are labeled with L; waste precipitates predominate.)

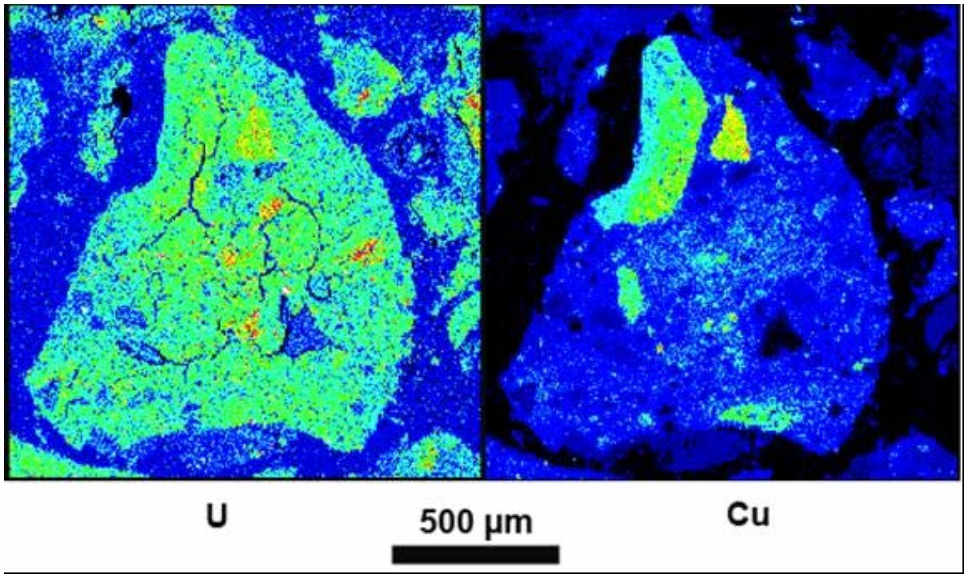

Figure 2.5. Elemental Abundance Maps (EMP) from the Large, Cracked Clast in Figure 2.4, for Uranium and Copper. (The uranium false-color spectrum was manipulated: white represents areas of greatest uranium abundance.)

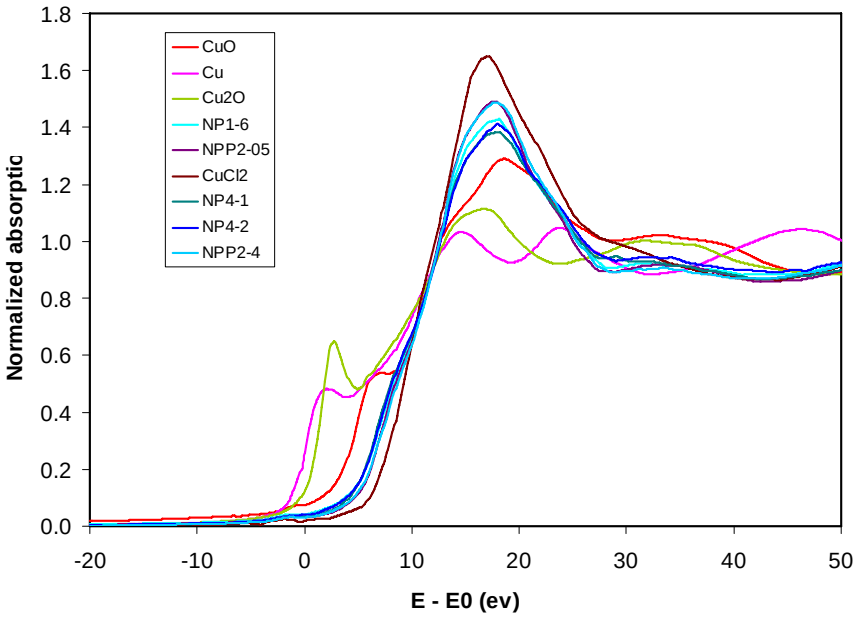

Figure 2.6. Bulk XANES Spectra for Copper from NP and NPP Samples, Relative to Indicated Standard

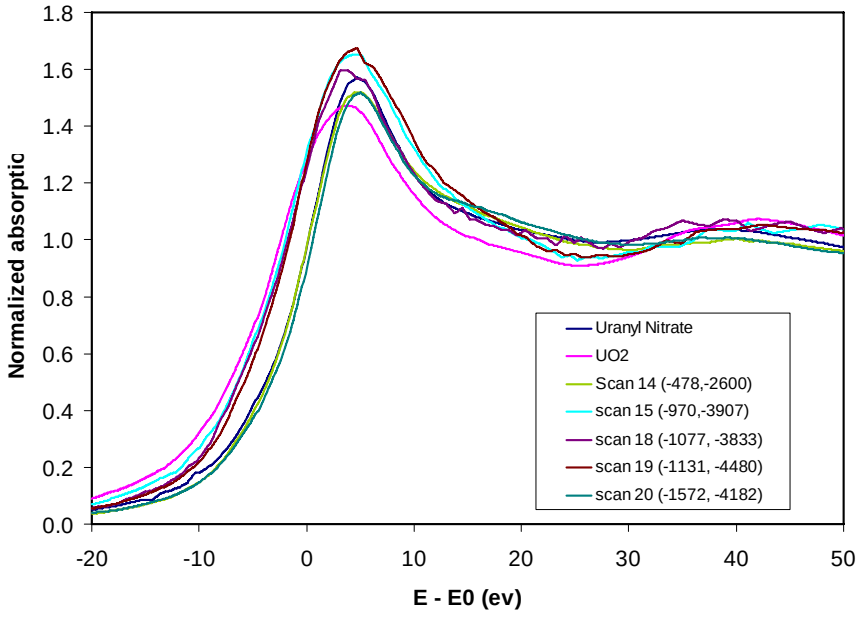

Figure 2.7. Spot XANES Spectra for Uranium from Sample NP1-4.5, Relative to Indicated Standards. (Numbers in parenthesis were analysis coordinates. Uranium valence was variable between U(VI) and U(IV).)

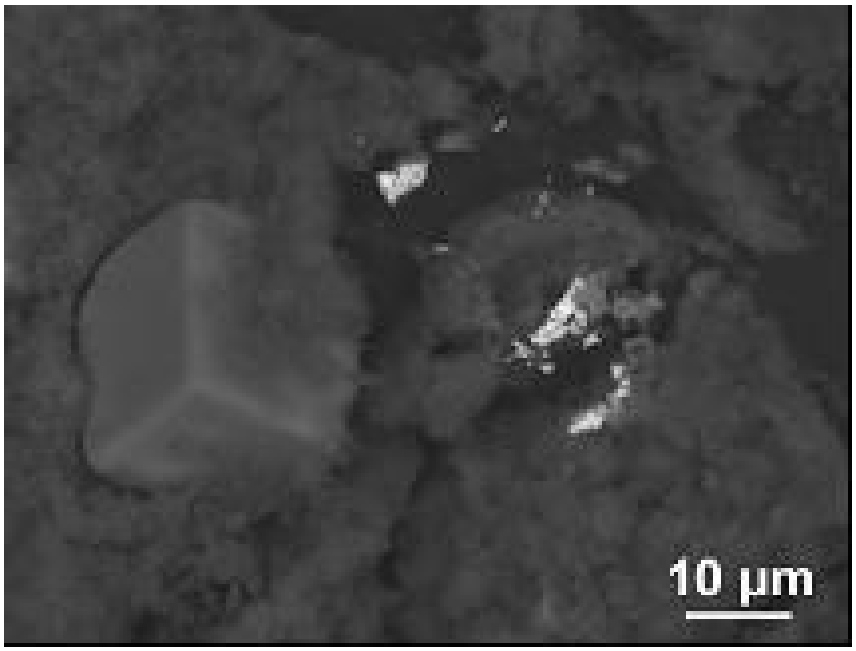

Figure 2.8. Backscattered Electron Image (SEM) of Sample NP4-1, Showing a Carbonate Rhomb Imbedded in Fine-Grained Matrix, and Fine, Micrometer-Scale Inclusions of a Uranium-Rich Phase

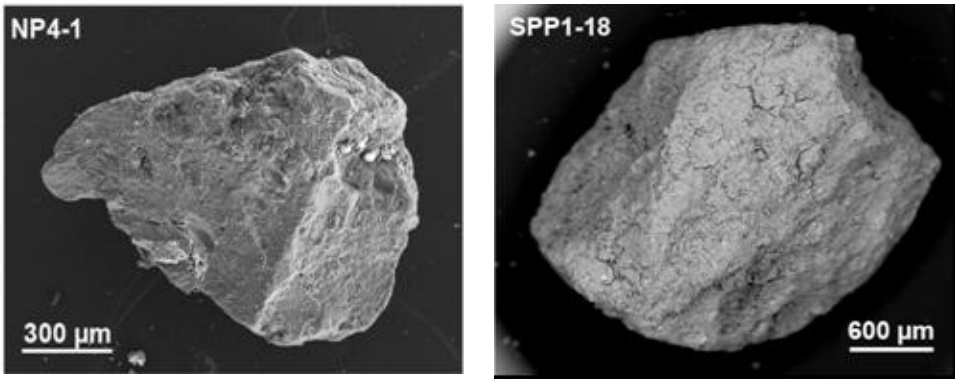

Figure 2.9. Surfaces of Clasts from Process Pond Sediment and from the Sediments Beneath the Ponds, Coated with Secondary Mineralization. (NP4-1: north pond, depth 0.3 m; SPP1-18: south pond sediment from 5.5 m beneath the pond.)

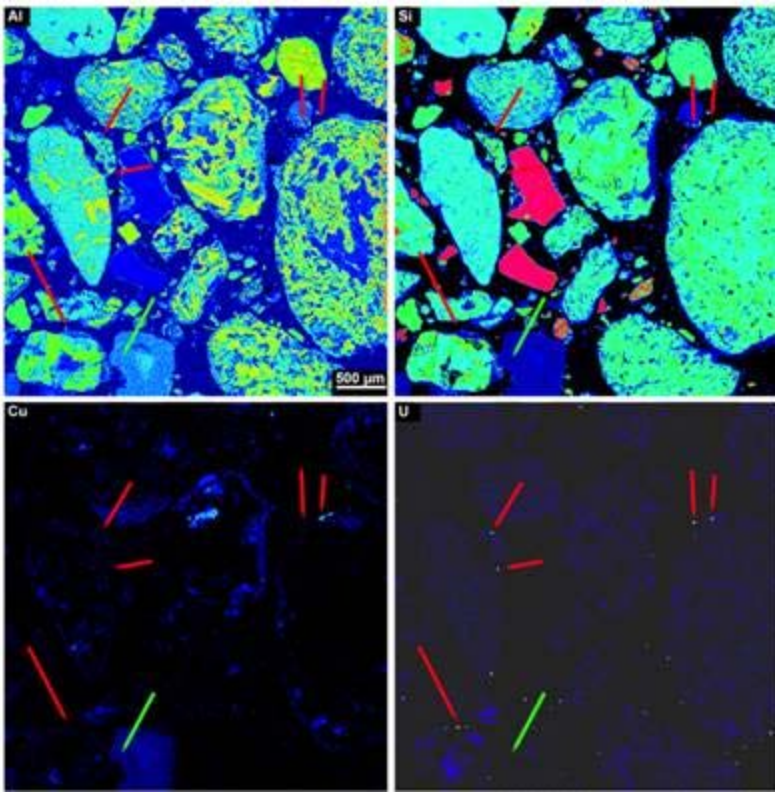

Figure 2.10. Elemental Abundance Maps for Aluminum, Silicon, Copper, and Uranium for Sample NPP2-4. (Red arrows indicate small uranium inclusions. The green arrow indicates a precipitate similar in structure and composition to those from NP samples.)

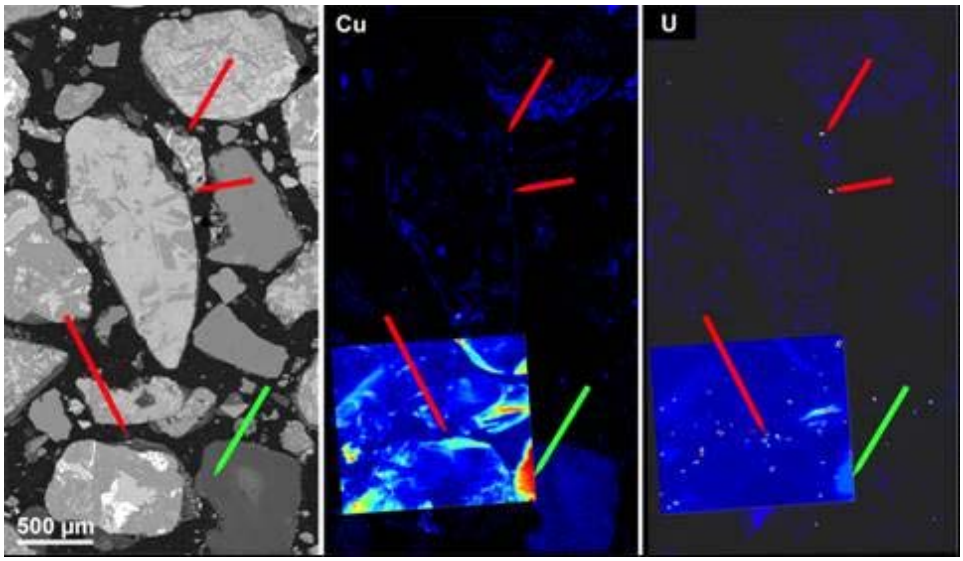

Figure 2.11. Backscattered Electron Image and Abundance Maps for a Portion of the Area Shown in Figure 2.9, Overlain by XMP Abundance Maps for Uranium and Copper

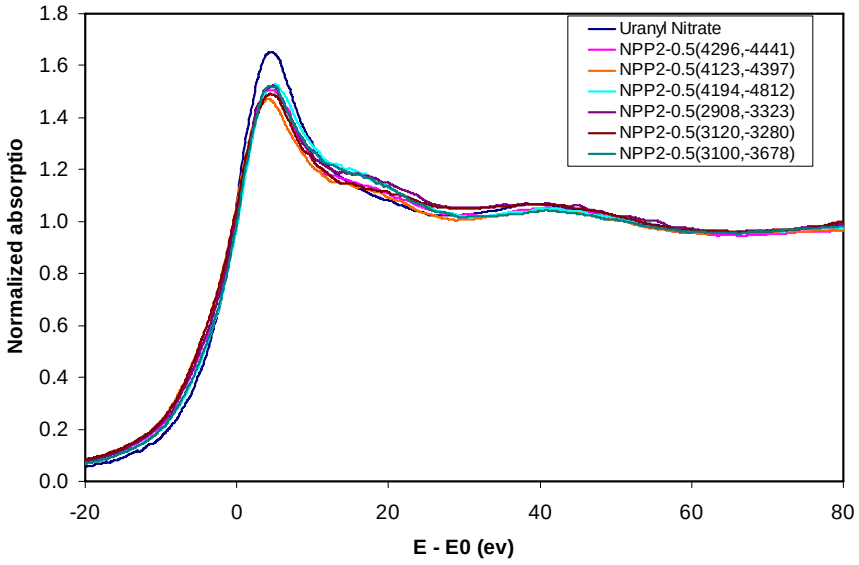

Figure 2.12. XANES Spectra of Different Uranium-Containing Spots in NPP2-0.5 Showing No Evidence for U(IV)

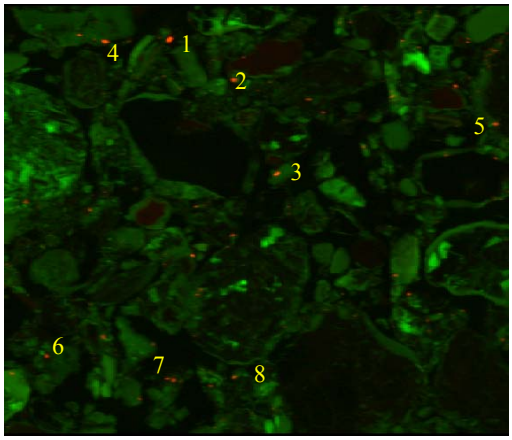

Figure 2.13. Micro-XRF Map (3 x 3 mm) of the Distribution of Uranium (red) and Copper (green). (Uranium-rich areas are represented in deep red, copper-rich areas in bright green, and copper-uranium phases in orange; NPP2-4.)

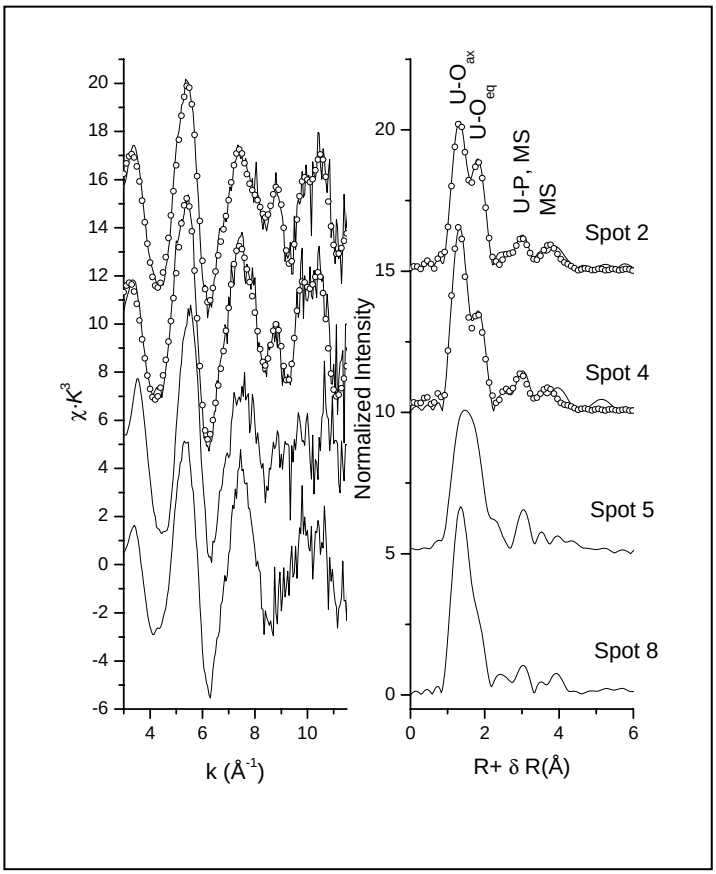

Figure 2.14. Uranium L_{III} Edge EXAFS Spectra and Corresponding FT Spectra from Selected Spots in Figure 2.13. (Solid line and dotted lines represent the normalized raw data and fit, respectively.)

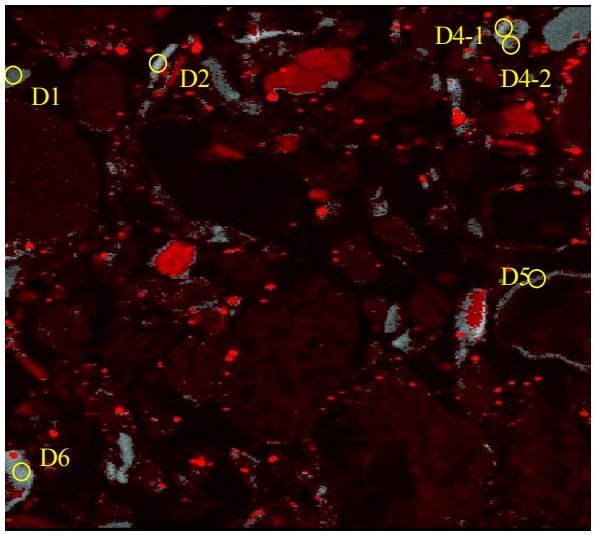

Figure 2.15. Micro-XRF Map (3 x 3 mm) of Same Area as Figure 2.13 with Image Analysis (Discrete (red) and Diffuse (gray) Uranium Precipitate. Diffuse uranium areas are represented in gray and designated with open yellow circles, e.g., diffuse uranium area D1.

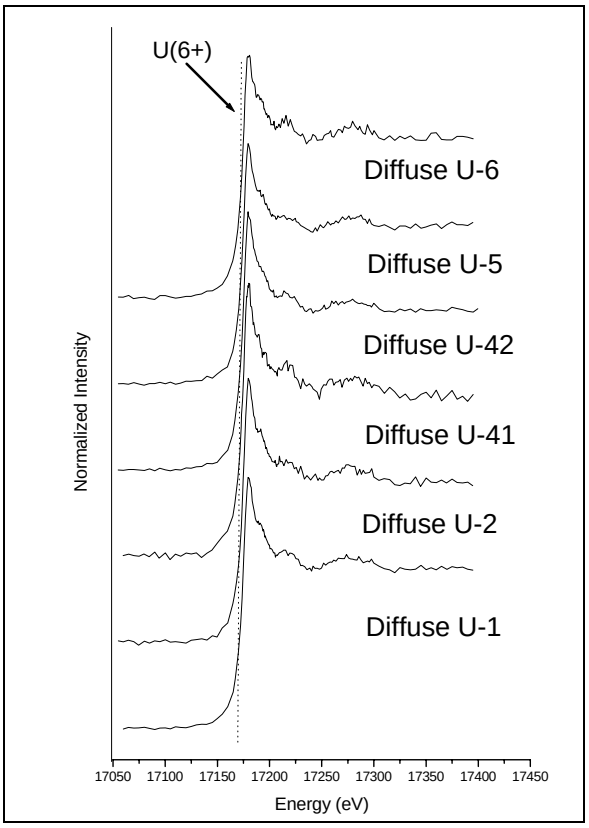

Figure 2.16. Normalized X-ray Absorption Near-Edge Spectra Collected at Selected Diffuse Uranium Areas in Figure 2.15. (The vertical dotted line corresponds to E_o of the U(6+) valence state.)

2.3 Spectroscopic Measurements of Chemical Speciation

Sorption strength and reversibility as well as the future mobility of sorbed uranium depend strongly on its chemical speciation in the contaminated sediment. Chemical speciation refers to the molecular environment that chemically interacts with or surrounds the uranyl cation. This environment may be: (1) waters of hydration for the bare uranyl aqueous cation; (2) one, two, or three covalently bound carbonate ions and water for an aqueous uranyl carbonate complex; (3) hydroxylated metal ion centers and water for adsorbed uranyl on iron, aluminum, and silicon oxides; and (4) dehydrated and or distorted octahedral, tetrahedral, and other crystallochemical environments for precipitated uranium in uranium minerals and as a minor substitute in other phases. The determination of chemical speciation is a primary pursuit in geochemistry that is accomplished using molecular spectroscopies of different sort.

Cryogenic laser induced fluorescence spectroscopy (CLIFS) (Wang et al. 2002, 2004, 2005b) and cryogenic laser induced fluorescence microscopy (CLIFM; results not reported here) (Wang et al. 2005b) were used to interrogate the chemical speciation of uranium in the various 300 Area sediment samples. CLIFS is one of the most sensitive spectroscopies for U(VI) chemical speciation, but its detection limit strongly depends on the sample composition. It is typically limited to concentrations in excess of 10 mg/kg uranium in sediment in a sorbed state. The detection limit is further constrained if high concentrations of transition metals, such as copper and iron, are present. This concentration threshold limited the total number of 300 Area sediment samples whose U(VI) speciation could be directly determined. The CLIFS measurements were preformed by pressing a small volume of sediment between a copper plate and a sapphire optical window, attaching it to the cold finger of a Cryo Industries RC-152 cryogenic workstation, and directly exposing the sample cell to the vapor flow of liquid helium at 6 ± 1 K. Time-resolved fluorescence emission spectra were recorded with a thermoelectrically cooled Princeton Instruments PIMAX time-gated, intensified charge-coupled device (CCD) camera, attached to the exit port of an Acton SpectroPro 300i double monochromator spectrograph. The data acquisition was automated by WinSpec™ data acquisition software and analyzed using the commercial software package IGOR™.

2.3.1 Results

CLIFS spectra that provided insights on U(VI) speciation could generally be collected on all sediments containing >10 mg/kg sorbed uranium. Examples of such spectra for a depth profile of samples from the NPP are shown in Figure 2.17. Three distinct spectral types were observed: a quartet for historical samples collected at the pond-waste interface (NP4-1 and NP 4-2), a broad singlet for the sample collected at the post excavation surface (NPP2-0.5), and a condensed triplet for deeper samples from the vadose zone (NPP2-2, NPP2-4, and NPP2-8). This spectral evidence indicated that the chemical speciation of U(VI) changed with depth beneath the disposal pond.

Significant efforts were expended to identify the geochemical nature of U(VI) in the sediments as implied by the CLIFS spectra. Because the samples collected at the pond-waste interface (NP4-1 and NP4-2) contained significant secondary calcite, a reference natural calcite containing co-precipitated U(VI) (360 mg/kg) (Kelly et al. 2003; Spottl et al. 2002) was analyzed as a spectral reference (Figure 2.18). This spectra was quite similar to that obtained for NP4-1 and NP4-2. Time resolved

CLIFS analysis of the natural U(VI)-containing calcite allowed identification of two chemical species in the natural calcite, components A and B (Figure 2.18), that each exhibited distinct spectra. The CLIFS spectra of the two chemical components were identical to those published of U(VI) in an aragonite structural environment (component A) and U(VI) in a calcite structural environment (component B) (Reeder et al. 2000, 2001). U(VI) in an aragonite environment dominated over U(VI) in calcite environment. Aragonite and calcite are two natural polymorphs of $CaCO_{3(s)}$. Aragonite has an open crystallographic structure that is more conducive to U(VI) co-precipitation than calcite, and it tends to precipitate in more saline, magnesium-enriched environments such as seawater (Stumm and Morgan 1996).

Similar time resolved measurements of NP4-1 (Figure 2.19, top panel) and NP4-2 (spectra not shown) also showed the presence of the same two chemical/spectral components as observed in the natural calcite. Comparison of the spectra of NP4-1 (Figure 2.19, top panel) and that of the uranium-rich natural calcite (Figure 2.19, bottom panel) recorded under the same conditions suggests that U(VI) in the aragonite structural environment was more predominant in the NP4-1 sediment. These analyses allowed the conclusion that that sorbed, high-concentration U(VI) present in NP4-1 and NP4-2 existed as a co-precipitate with $CaCO_{3(s)}$. Because x-ray diffraction measurements indicated that the $CaCO_{3(s)}$ polymorph in NP4-1 was calcite, the spectroscopic measurements implied that defect micro/nano-scopic aragonite domains existed within the calcite, and that these played host to a portion of the substituted U(VI). Moreover close inspection of the peak positions in the CLIFS spectra of the deeper vadose zone sediments (NPP2-4.0 and NPP2-8.0; Figure 2.17) with component B in Figures 2.18 and 2.19 indicated close similarly, implying that the U(VI) chemical environment in these deeper sediments was calcite-like. Ongoing CLIFS measurements are seeking to resolve the identity of the uranium-phase in samples NPP-2-4.0 and NPP2-8.0, but synchrotron measurements on these same samples reported in Section 2.2 suggest the occurrence of metatorbernite, a precipitated copper-uranium-phosphate.

Noticeable differences existed between the fluorescence properties of the NP1-6 (Figure 2.20) and NP4-1 sediments (Figure 2.19). (Note: NP1-6 was another historical sample obtained from the NPP at a depth of 1.8 m.) While the fluorescence decay of sediment NP1-6 could be well fitted with two exponential functions, the resulting fluorescence lifetimes were appreciably shorter than those of the NP4-1 sediment, suggesting the presence of fluorescence quenching. One potential cause could be co-associated copper and iron ions that are known to quench uranyl fluorescence and to be present in the contaminated sediments in relatively high concentrations. Although the time-resolved laser fluorescence spectroscopy (TRLFS) spectra could be simulated by two spectral components (Figure 2.20, top panel), the spectra assigned to uranium-bearing aragonite differed in resolution and peak intensities from those in uranium-rich natural calcite and NP4-1 sediment. When it was assumed that NP1-6 contained the same uranium-bearing aragonite as in NP4-1, the spectra of component B of NP1-6 was found to be a composite of a uranium-bearing aragonite spectrum and a third component, C (Figure 2.20, bottom panel). The presence of more than two U(VI) molecular species in the NP1-6 sediment was thus implied. The validation and identity of the third component is still under investigation.

The NP1 and NP4 samples were collected at different spatial locations and depths in the NPP. NP4-1 was collected at depth of 0.25 m and NP1-6 at 1.8 m. Perhaps sediment-waste reactions caused significant differences in the pH, ion/metal composition, total carbonate concentration, and ionic strength

of waste waters at the two locations. These chemical variables are known to have significant effects on the polymorph, precipitation rate, and minor element substitution of carbonates. Significant chemical differences existed between the sediments. More carbonate precipitation occurred from waste neutralization in sample NP4-1 (3.2%) than in the deeper NP1-6 (0.99%) sediment. Moreover, laboratory dissolution experiments with these sediments (data not shown) have revealed the presence of high soluble Mg^{2+} in sample NP4-1. The higher uranium concentration in sample NP4-1, combined with high dissolved Mg^{2+} during precipitation, could favor uranium substitution into aragonite-type coordination environments, consistent with the speciation trend observed.

Spectroscopic analyses were also performed on U(VI)-containing groundwater fines collected from multiple locations in aquifer sediments beneath the NPP and SPP (Figure 2.21). The fines were suspended particles that were filtered from contaminated groundwater that filled the excavation when it was deepened into the saturated zone. The fines were the dominant mineral sorbents of U(VI) in the aquifer sediments, and some contained U(VI) at concentrations near the spectroscopic detection limit (30 mg/kg). Nonetheless, informative CLIFS spectra were obtained on all samples. CLIFS spectra were measured at two distinct spatial locations in samples SPP1 and NPP2 (as designated by numbers in parentheses Figure 2.21) to determine if speciation varied within the sample. Sample SPP1 showed internal variability while sample NPP2 was uniform in speciation. Two primary spectral patterns were observed: (1) a calcite-like pattern (e.g., component B) for the highest concentration sample [NPP2 (1,2)], and (2) an illite-like pattern for low concentration sample SPP1 (2). The spectra for SPP1 (1) and NPP1 represented linear combinations of these two primary spectra, albeit at different concentration ratios. These results, which are now being quantitatively interpreted in detail, imply that U(VI) is associated with both calcite and/or the phyllosilicate fraction (mica, chlorite, vermiculite) in the aquifer sediments.

2.3.2 Synopsis and Implications

The synopsis of findings from spectroscopic measurements of chemical speciation and their implications are as follows:

- CLIFS was used to study the mineral/chemical speciation of U(VI) in pond sediment, deeper vadose zone sediment, and the aquifer fines.

- The spectroscopic method has a nominal detection limit of 10 mg/kg. Therefore, the majority of the historic samples NP4-1 and NP4-2 and deeper vadose zone sediment samples from pit #2 in the NPP, and groundwater fines from three of the excavations (SPP1, NPP1, and NPP2) could be interrogated by CLIFS.

- CLIFS measurements implied that the speciation of sorbed U(VI) varies with depth and spatial sampling location. Sorbed U(VI) exists in various discrete chemical environments: (1) as a co-precipitate within aragonite-defected calcite in NPP sediments [U(VI) >2,400 mg/kg], (2) within a calcite-like structure or a copper phosphate in deeper vadose zone sediments beneath the NPP (for sediments with U(VI) >45 mg/kg), and (3) within calcite [U(VI) >200 mg/kg] and as sorption complexes to the surfaces of phyllosilicates [U(VI) = 33-35 mg/kg] in the aquifer sediments. These interpretations are preliminary and will be verified over the coming months

- The U(VI) that exists within carbonates or other precipitated phases is expected to dissolve/desorb very slowly because 300 Area pore and groundwater are near saturation with calcite.

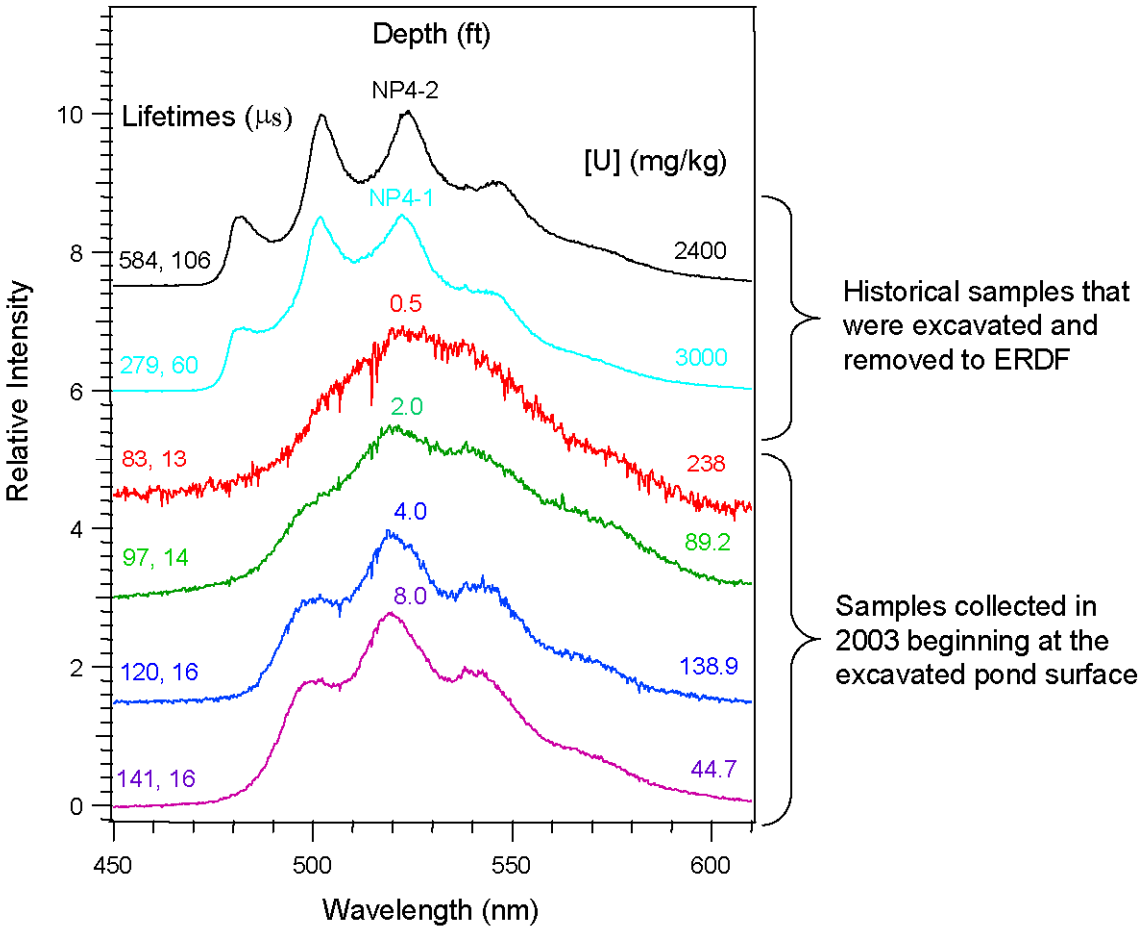

Figure 2.17. LHeT Fluorescence Spectra of 300 Area North Process Pond Sediments (NP4-1 and NP4-2) and Underlying Vadose Zone Sediments (NPP2) at Different Depths. (λlex = 415 nm; delay = 100 ms; gate width = 100 ms. For clarity, the spectra were normalized and offset along the Y-axis.)

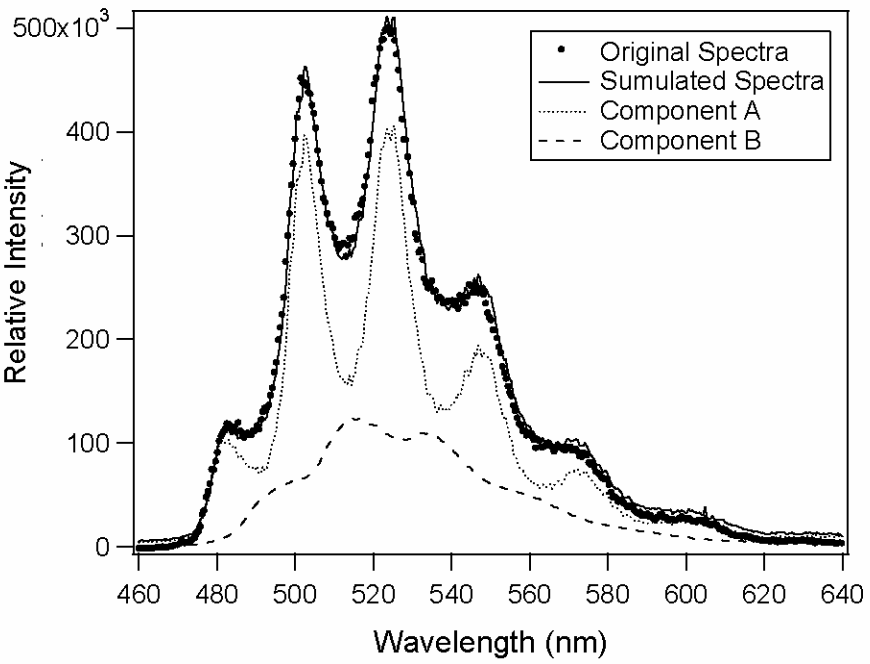

Figure 2.18. Deconvolution of the LHeT Time-Resolved Fluorescence Spectra of the Uranium-Rich Natural Calcite at a Delay Time of 1 ms into Two Unique Spectral Components A and B

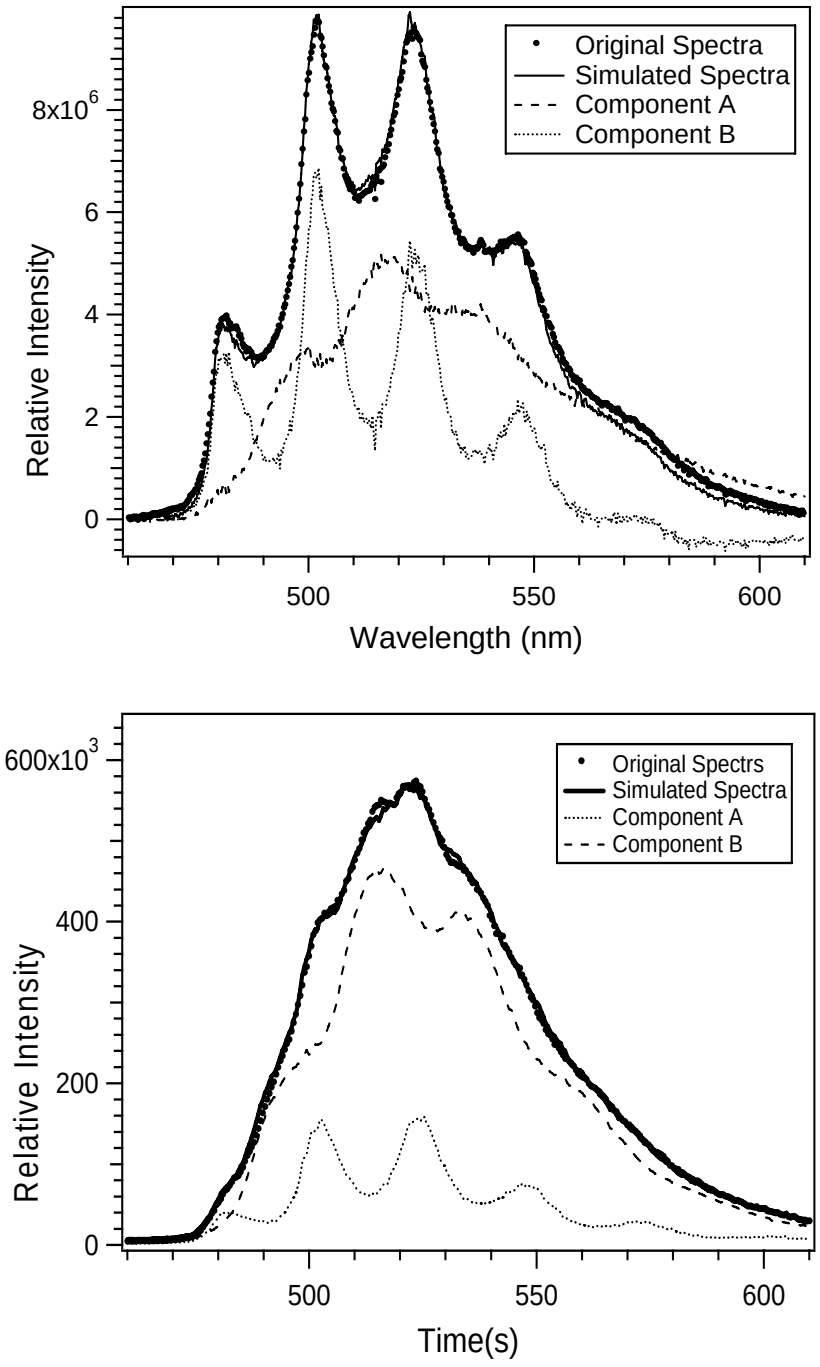

Figure 2.19. Deconvolution of the LHeT Time-Resolved Fluorescence Spectra of NP4-1 (top panel) and Uranium-Rich Natural Calcite (bottom panel). (Gate width of 10 ms with no time delay into two unique spectral components A and B.)

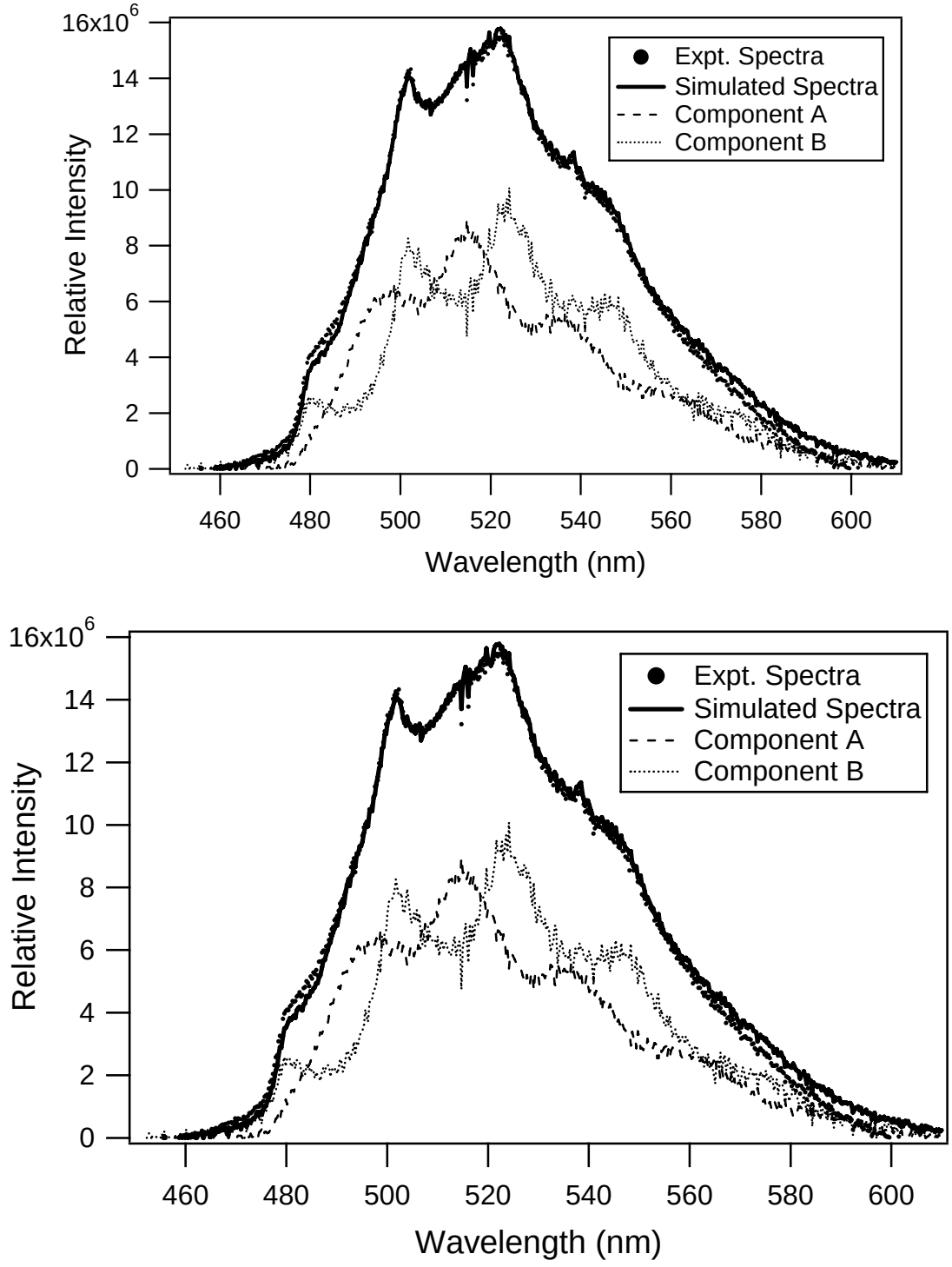

Figure 2.20. Deconvolution of the LHeT Time-Resolved Fluorescence Spectra of NP1-6 into Two Unique Spectral Components A and B (top panel) or Three Spectral Components (bottom panel). (Gate width of 10 ms with no time delay.)

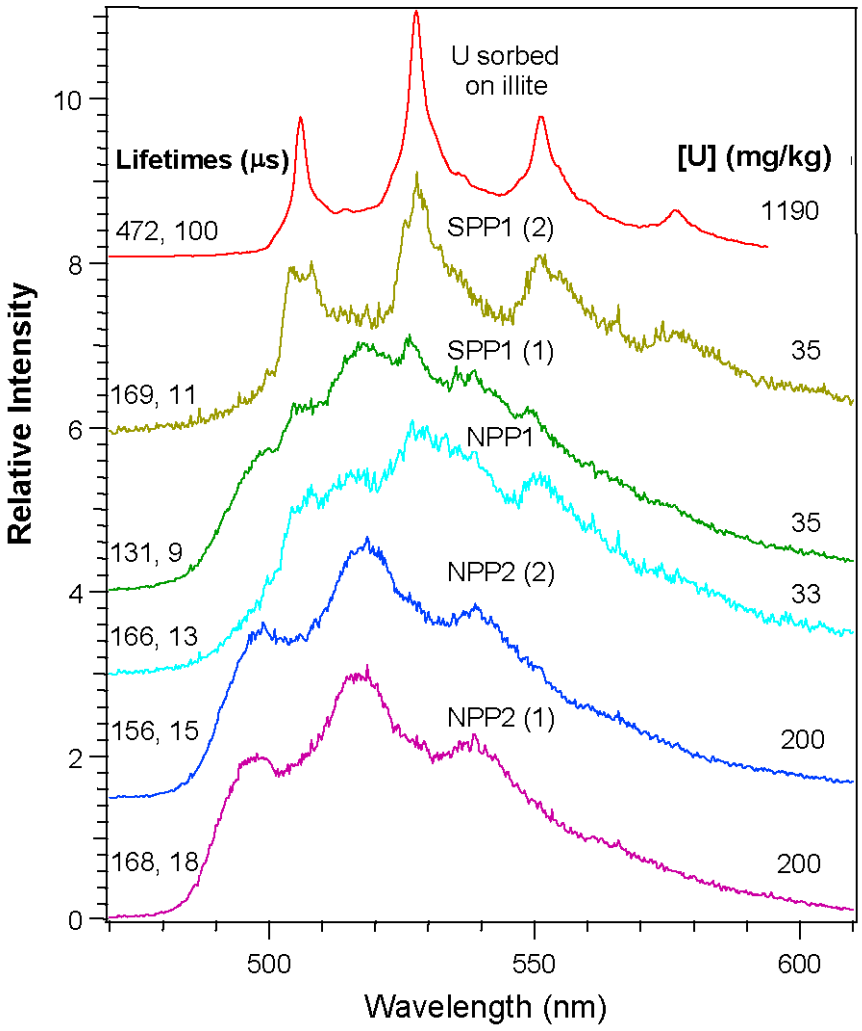

Figure 2.21. LHeT Fluorescence Spectra of 300 Area North Process Pond Groundwater Fines Along with that of Uranium Sorbed on Illite. (λlex = 415 nm; delay = 100 ms; gate width = 100 ms. Numbers in parenthesis indicate measurements at different locations on the same sample. The spectra were normalized and offset along the Y-axis for clarity.)

2.4 Batch Adsorption/Desorption Studies, K_d Measurement, and Surface Complexation Modeling

Uranium distribution coefficients (K_d) at Hanford are highly variable (0.1 to >50 mL/g) due to physical and chemical variability at the site. Several studies have examined variability in U(VI) K_d values at sites other than Hanford and concluded that uncertainties are introduced with constant K_d models (Kohler et al. 1996; Read et al. 1998; Koretsky 2000; Bethke and Brady 2000; Glynn 2003). The K_d is often measured under atmospheric conditions while $pCO_{2(g)}$ in aquifers can reach up to 5% (Hem 1985). Even small differences in $pCO_{2(g)}$ can result in orders of magnitude differences in the U(VI)-K_d.

It has been well documented (Davis and Curtis 2003; Davis et al. 2002; Davis et al. 2004; Arnold et al. 2001; Pabalan et al. 1998; Waite et al. 2000) that U(VI) can be modeled effectively using a surface complexation approach. However, the only surface complexation model (SCM) developed to date for the Hanford Site (Barnett et al. 2002) is based on the undocumented assumption that ferrihydite is the primary U(VI) adsorbent. In reality, ferrihydrite is extremely sparse in Hanford sediments. A specific method describing U(VI) adsorption with surface complexation modeling is lacking for the 300 Area given the apparent deficiency of iron hydroxides in the sediments. In addition, consideration of recently described calcium-uranium-carbon dioxide aqueous complexes (Brooks et al. 2003), generally not considered in modeling approaches, may have significant impacts on the prediction of U(VI) retention. To account for the variabilities observed in uranium K_ds, a new geochemical conceptual model is being formulated for U(VI) adsorption to 300 Area sediments. This model is to include surface complexation modeling of data collected in the laboratories at the U.S. Geological Survey (USGS).

2.4.1 Results

The total uranium content of the 300 Area sediments, as determined by γ-spectrometry (Table 2.6), shows that many of the vadose zone samples beneath the ponds are enriched in uranium. A large fraction of the uranium associated with these samples is available for exchange with vadose zone water. During isotopic exchange in artificial groundwater (AGW, Table 2.7), an initial rapid release of U(VI) is followed by a slow steady progression towards pseudo-equilibrium lasting several months (Figure 2.22). Among the samples studied, the fraction of total U(VI) exchanged after 1 day of equilibration with ^{233}U ranged from 20% to 75% (Table 2.8). As an operational definition for sorption calculations, it was assumed that the U(VI) exchanged within 24 hours is bound to the sediments as an adsorbed surface species. Longer reaction times for isotopic exchange allow for the engagement of dissolution/ precipitation processes. The isotopic exchange results also shed light on the variability of K_d values for these sediments. Values ranged from 0.5 to 28 mL/g in AGW 4 solution among all of the sediment samples.

Dilute (bi)carbonate extraction has been shown in previous studies (Davis and Curtis 2003; Kohler et al. 2004) to offer an easier means of estimating adsorbed uranium (than isotopic exchange) by complexing U(VI) with high levels of aqueous carbonate to form exceptionally soluble species, without dissolution of mineral matrices. In this study, values correlated fairly well between the isotopic exchange result (24 hours) and the amount of U(VI) extracted by dilute bicarbonate solution (72 hours) for most 300 Area samples, with an average difference of 2% (Table 2.8). In general, the dilute (bi)carbonate

extractions exhibited the same biphasic behavior as isotopic exchange, with an initial rapid desorption followed by slow steady release (Figure 2.23). In the dilute (bi)carbonate extractions, dissolved U(VI) concentrations reached a plateau on about the same time scale as the net isotopic exchange rate declined to near zero (approximately 8 weeks). In the dilute (bi)carbonate extractions, the pH initially drops ~0.5 units to 9.0 and the dissolved calcium concentration in solution also decreases, indicating the occurrence of a minor amount of calcite precipitation. It is important to keep the pH value above 9 in order to avoid re-adsorption of dissolved U(VI) in the extractions.

The spectroscopic results in Section 2.3 implied that a portion of the uranium in the 300 Area vadose zone sediments is associated with calcite (Wang et al. 2005a), both as a sorbed surface species and incorporated into the structure of the mineral. In order to estimate the U(VI) sediment content contained within carbonate minerals, formate buffer solution at pH 3.5 was added to the Hanford sediments. At this pH, calcite, along with dolomite and aragonite, will dissolve and release U(VI) from the crystal matrices. In addition, U(VI) should be desorbed in this region and re-adsorption of dissolved U(VI) should be negligible. Thus, the intent of the extraction is to determine the quantity of carbonate mineral associated uranium plus adsorbed U(VI), allowing the estimation by carbonate mineral associated uranium by difference.

An increase in extractable uranium of 20 to 50% above the amount of adsorbed U(VI) (by 24 hour isotopic exchange) was observed for all samples (Table 2.8), indicating that a significant fraction of total uranium in the sediments may be co-precipitated with carbonate phases. Dissolved silicon, calcium, and aluminum concentrations increased by 1, 3, and 4 orders of magnitude, respectively compared to equilibration in AGW 4 (Figure 2.24). Elevated levels of dissolved copper were measured for the samples with the highest uranium concentration (NPP2-2 and NPP2-8).

It is possible that poorly crystalline iron and aluminum oxides undergo partial dissolution in the formate buffer extractions, and any U(VI) associated with these secondary mineral coatings would be measured in addition to that released from carbonate minerals. Extractions of iron by hydroxylamine hydrochloride (HH), ammonium oxalate (AMOX) and dithionite citrate bicarbonate (DCB) were performed at PNNL and give some insight into the possible interactions between U(VI) and iron bearing minerals (Table 2.9). The DCB extraction removes reducible iron oxides including hematite, goethite, lepidocrocite, and ferrihydrite. Both HH and AMOX attack only poorly crystalline iron oxides, and these released approximately 40% of the total iron in the 300 Area sediments. The formate buffer dissolved only ~12 μmol/g iron from the solids, accounting for <10% of total extractable iron, but it is possible that some dissolved iron would be re-adsorbed at the pH of 3.5.

Approximately 80 to 90% of total U(VI) was extracted from the Hanford sediments during the strong iron oxide extractions (Table 2.10). This is understandable given that the extractions are performed under extreme conditions, pH below 3 or temperatures >50^{o}C. Extractions with formate buffer solution removed ~10% less uranium than those targeting iron digestion, suggesting little of the U(VI) was contained within well-crystallized iron oxide matrices (although sorption on iron oxides would still be possible).

One sample (SPP 2-18) released the same amount of U(VI) when extracted with HH, DCB, and formate buffer. In this sample, only 60% of the total uranium was dissolved, whereas other samples were near 90%. This sample contained the lowest total uranium concentration (2.8 mg/kg), near the value for crustal abundance of uranium, and suggests that there is a background concentration of unextractable U(VI) of ~1 mg/kg in all 300 Area sediments.

When equilibrated with artificial groundwater solutions (Table 2.7), all of the sediment samples released amounts of uranium well above drinking water standards. The lowest amount of uranium desorbed in any sample suspended in AGW4 (with alkalinity of 4 meq/L or 200 mg/L as $CaCO_3$) was 460 ppb. Over 20,000 ppb of U(VI) were desorbed from sample NPP 2-2 in contact with AGW 4. Desorption kinetics were rapid for the first 24 hours of reaction and then slowed to a more steady release of uranium for approximately 1 week. This biphasic kinetic behavior is similar to that observed in the isotopic exchange and dilute bicarbonate extractions. There are two possible explanations for the kinetic observations: (1) U(VI) is being released quickly by desorption and slowly from U(VI)-substituted calcite, and/or (2) that U(VI) is slowly released from intra-grain nano- and micro-porosity by diffusion.

An important observation to consider in a robust model for the 300 Area groundwater plume is that the rising and falling stage of the Columbia River causes river water to mix with ambient groundwater in the vadose zone, causing temporal changes in alkalinity. Alkalinity in the river ranges from 40 to 65 mg/L (as $CaCO_3$), while measurements of 300 Area groundwater have ranged from 95 to 300 mg/L. As has been shown in other studies (Davis and Curtis 2003; Davis et al. 2004; Pabalan et al. 1998; Waite et al. 2000; Curtis et al. 2004), U(VI) sorption is extremely sensitive to the alkalinity value because of aqueous carbonate complexation, and this general observation also holds true for the Hanford sediments (Figures 2.25 and 2.26). Additional data on the alkalinity dependence of U(VI) sorption by the sediments (for samples other than NPP 1-16 and SPP 2-18) is currently being collected.

It was observed that NPP sediment samples adsorbed U(VI) more strongly than SPP sediment samples (Figures 2.26 and 2.27). The reason for the difference between the samples from the two different locations is not known as yet, but it was observed consistently throughout all of the experiments. This was true despite the fact that NPP sediments were sampled from two different locations, as were the SPP samples.

Two simple SCM were calibrated for the sediment samples, one based on the data collected for the NPP sediments and another for the SPP sorption data. SCM calibration was completed using the generalized composite approach as described by Davis et al. (2004). Only one site type was specified in the models, and the total site density was given by the common guideline value of 3.84 $\mu mol/m^2$ of surface area (Davis et al. 2004).

The sorption datasets for the NPP and SPP sediments were considered separately in calibrating the SCMs. For each dataset, each of the surface reactions shown in Table 2.11 was tested to determine the best fit to the experimental data, and then all pairs of the reactions were considered for the best fit. Because of the importance of alkalinity as a variable, the sorption data were weighted to give more importance to fitting the sorption data as a function of alkalinity than as a function of U(VI) concentration (isotherm data). The effect of the data weighting can be seen in the superior fit to the experimental data in Figure 2.26 versus Figure 2.27. The addition of a third reaction or a second type of sorption site

(strong sites) did not improve the fit to the data. The two surface reactions given below (Davis et al. 2004) were best for fitting the data for both datasets, and these are the same reactions that were used to describe U(VI) sorption by alluvial aquifer sediments at a DOE uranium mill tailings remedial action (UMTRA) site in Colorado. For the NPP sediments, the reactions and surface constants are:

$$SOH + UO_2^{2+} = SOUO_2^{+} + H^{+} \qquad \text{Log K} = 2.88$$

$$SOH + UO_2^{2+} + H_2O = SOUOOH + 2H^{+} \qquad \text{Log K} = -4.61$$

For the SPP sediments, the reactions and surface constants are:

$$SOH + UO_2^{2+} = SOUO_2^{+} + H^{+} \qquad \text{Log K} = 2.45$$

$$SOH + UO_2^{2+} + H_2O = SOUOOH + 2H^{+} \qquad \text{Log K} = -4.90$$

Note that the surface complexation constants are greater in the SCM for NPP sediments than for the SPP sediments, in agreement with the experimental observation that U(VI) sorption is greater on the NPP sediments.

Although there is a clear and significant difference in U(VI) sorption on the NPP and SPP sediment samples, it is recognized that it might be necessary to use only one SCM in new reactive transport simulations for the 300 Area. If this limitation is imposed, a new SCM can be easily derived with parameter values determined from fitting both sorption datasets simultaneously. As mentioned above, new data are being collected as a function of alkalinity to add to these datasets.

2.4.2 Synopsis and Implications

The synopsis of findings from batch adsorption/desorption studies, K_d measurement, and surface complexation modeling and their implications are as follows:

- Bicarbonate extraction and isotopic exchange was applied to fourteen 300 Area vadose zone sediments and three groundwater fines to evaluate the fraction of the sorbed U(VI) pool that is exchangeable or reactive with pore water. The labile fraction in vadose zone sediments ranged from 21 to 76% with an average of 44%, while the groundwater fines ranged from 24.1 to 47.8% with an average of 38.2%. The non-labile fraction is effectively immobilized in the mineral fraction. The labile fraction must be explicitly considered in calculation of K_d.

- A comprehensive series of batch sorption studies were performed with two capillary fringe sediments from the north (NPP1-16) and south (SPP2-18) process ponds and a series of artificial groundwater solutions. The magnitude of the adsorption/desorption K_d values varied directly with bicarbonate concentration. Increasing bicarbonate concentration in the range of 0.05 to 10 μmol/L (the approximate range in HCO_3 present in 300 Area subsurface waters) causes major reductions in K_d. NPP sediments sorbed U(VI) more strongly than did SPP sediments by factors of two or more.

- An isotopic exchange technique was applied to measure effective K_d values for seventeen 300 Area sediments (<2.0 mm fractions) that varied in total U(VI) content in an artificial groundwater containing 4.0 mM HCO_3. Values ranged from 0.5 to 28 mL/g.

- Chemical extractions of the 300 Area sediments indicated that a significant fraction of sorbed U(VI) existed in association with solid phase carbonates as implied by the microscopy and spectroscopic studies in Sections 2.2 and 2.3.

- A two reaction surface complexation model was formulated that accounts for the effects of bicarbonate concentration, sediment surface area, and aqueous U(VI) complexation on U(VI) sorption to 300 Area sediments. The model can predict K_d, at different pH and alkalinity values. Different parameter sets were required for the NPP and SPP sediments because of their different mineralogical character.

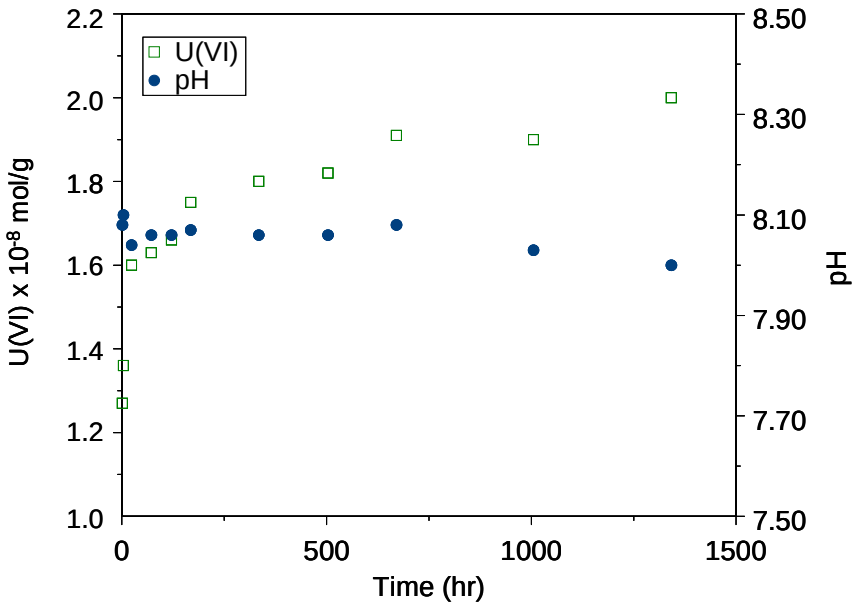

Figure 2.22. U(VI) Undergoing Isotopic Exchange Between the Aqueous and Solid Phases in Artificial GW4 Containing ^{233}U for Sediment Sample NPP 1-16 (100 g/L)

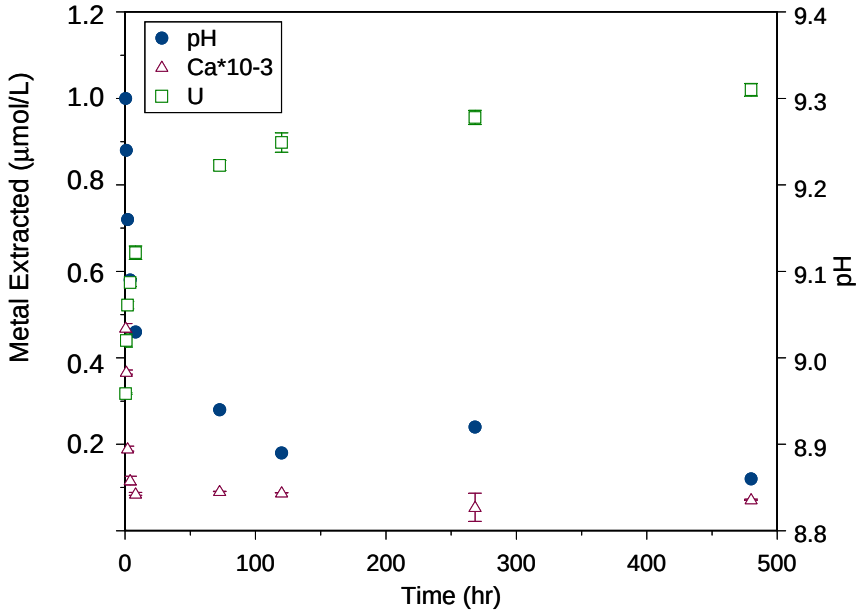

Figure 2.23. U(VI) and Calcium Released During Dilute Bicarbonate Extraction of Sediment Sample, NPP 1-16 (50 g/L)

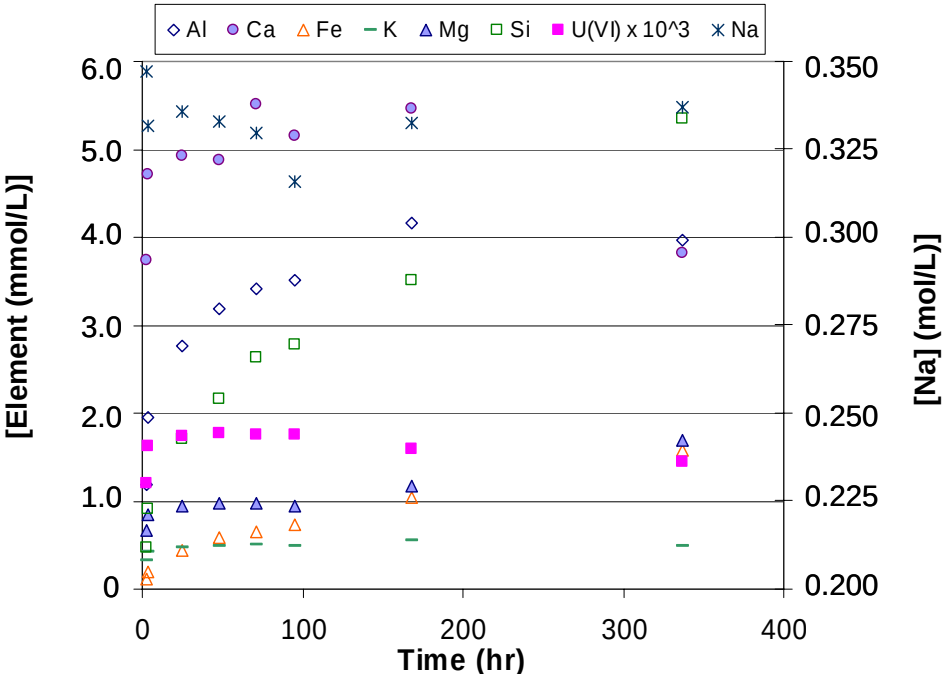

Figure 2.24. Aqueous Concentrations of Selected Elements During Formate Buffer Extraction of Sediment Sample, NPP 1-16 (50 g/L). (pH remained constant at 3.5 during the extraction.)

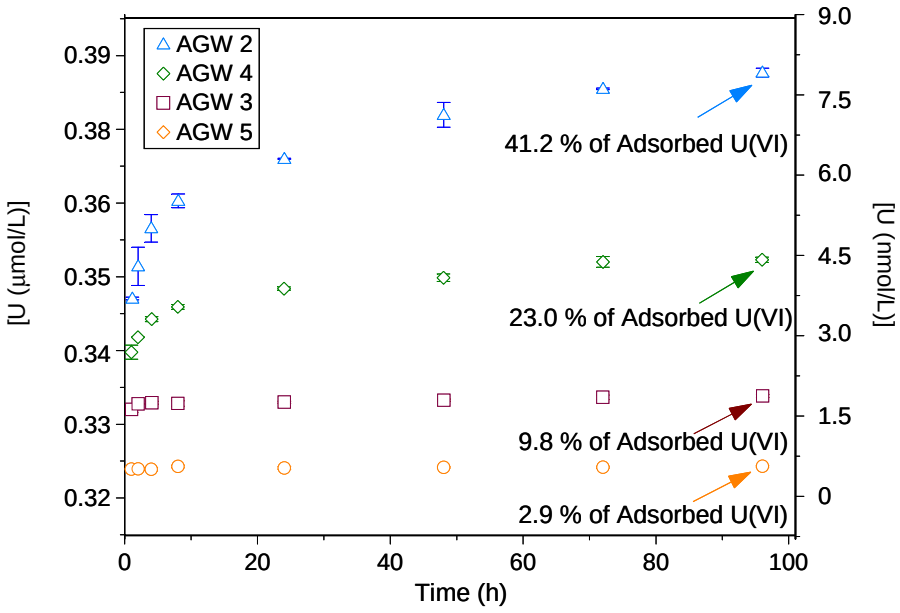

Figure 2.25. U(VI) Desorption from Sediment Sample, NPP 1-16 (200 g/L), During Equilibration with Artificial Groundwater of Varying Alkalinity. (AGW2, alkalinity of 9 meq/L; AGW4 = 4 meq/L; AGW3 = 2 meq/L; AGW5 = 1 meq/L. Total adsorbed U(VI) for the sample defined by the amount undergoing isotopic exchange within 24 hours.)

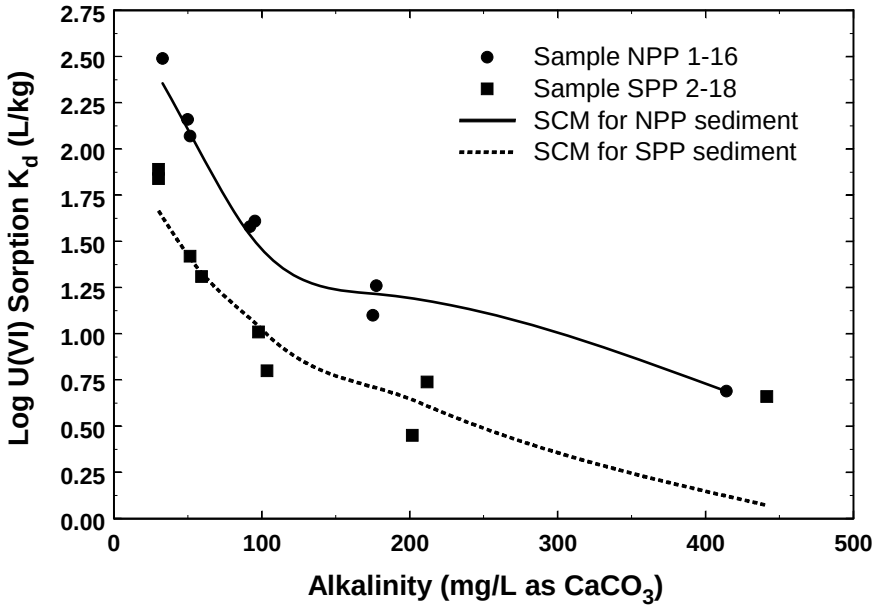

Figure 2.26. Dependence of the Log of the U(VI) Sorption K_d Value on Alkalinity for Samples, NPP 1-16 and SPP 2-18, When Equilibrated in Artificial Groundwater of Varying Composition. (Solid curves show the fits to the data for the surface complexation models for U(VI) sorption on NPP and SPP sediments.)

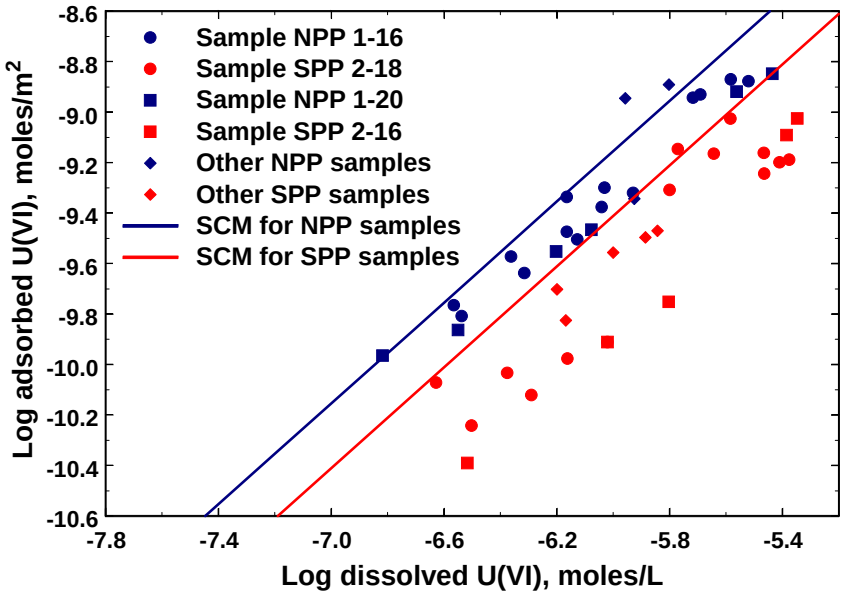

Figure 2.27. U(VI) Adsorption Isotherms for NPP and SPP Sediment Samples Suspended in AGW4 and AGW9. (Alkalinities in the NPP experiments ranged from 164 to 227 mg/L as $CaCO_3$ [average of 188 mg/L], causing some of the scatter in the data. Alkalinities in the SPP experiments ranged from 168 to 226 mg/L [average of 190 mg/L]).

Table 2.6. Uranium Extraction and Total Uranium (mol/g)

Sample	[U(VI)] Extracted by Bicarbonate[(a)]	[U(VI)] Extracted by AGW4[(b)]	[U(VI)] Exchanged with ^{233}U Isotope[(c)]	Total U by γ–Spectroscopy[(d)]	Solid Phase [U] by XRF[(e)]
NPP 1-8	1.98×10^{-8}	1.07×10^{-8}	3.30×10^{-8}	4.40×10^{-8}	5.42×10^{-8}
NPP 1-12	2.52×10^{-8}	1.15×10^{-8}	2.39×10^{-8}	5.89×10^{-8}	8.61×10^{-8}
NPP 1-16	1.55×10^{-8}	6.92×10^{-9}	1.60×10^{-8}	4.04×10^{-8}	4.66×10^{-8}
NPP 1-20	7.82×10^{-9}	4.13×10^{-9}	7.96×10^{-9}	2.63×10^{-8}	4.71×10^{-8}
NPP 2-2	1.32×10^{-7}	2.03×10^{-8}	1.88×10^{-7}	4.44×10^{-7}	3.75×10^{-7}
NPP 2-8	6.28×10^{-8}	2.81×10^{-8}	9.69×10^{-8}	1.67×10^{-7}	1.88×10^{-7}
NPP 2-12	3.35×10^{-8}	1.53×10^{-8}	3.42×10^{-8}	5.97×10^{-8}	6.39×10^{-8}
SPP 1-16	1.68×10^{-8}	9.94×10^{-9}	1.58×10^{-8}	3.08×10^{-8}	5.71×10^{-8}
SPP 1-18	1.12×10^{-8}	6.14×10^{-9}	1.05×10^{-8}	3.12×10^{-8}	5.25×10^{-8}
SPP 1-22	1.17×10^{-8}	6.74×10^{-9}	1.06×10^{-8}	3.30×10^{-8}	2.60×10^{-8}
SPP 2-8	1.98×10^{-8}	1.39×10^{-8}	1.99×10^{-8}	4.53×10^{-8}	4.62×10^{-8}
SPP 2-12	1.93×10^{-8}	1.26×10^{-8}	1.76×10^{-8}	3.35×10^{-8}	5.13×10^{-8}
SPP 2-16	6.63×10^{-9}	4.61×10^{-9}	6.68×10^{-9}	1.62×10^{-8}	$<2.23 \times 10^{-8}$
SPP 2-18	2.26×10^{-9}	1.47×10^{-9}	2.48×10^{-9}	1.20×10^{-8}	$<2.27 \times 10^{-8}$
NPP 1 GW fines	3.93×10^{-8}	1.97×10^{-8}	3.81×10^{-8}	8.90×10^{-8}	1.39×10^{-7}
NPP 2 GW fines	2.73×10^{-7}	N/A	N/A	6.60×10^{-7}	8.40×10^{-7}
SPP 1 GW fines	7.63×10^{-8}	4.07×10^{-8}	3.16×10^{-8}	1.31×10^{-7}	1.34×10^{-7}
SPP 2 GW fines	2.23×10^{-8}	1.50×10^{-8}	2.67×10^{-8}	5.59×10^{-8}	5.34×10^{-8}

(a) Bicarb extraction values are from 72-hour sampling.
(b) AGW 4 desorption values are from 72-hour sampling. AGW 4 composition is shown in Table 2.8.
(c) Isotopic exchange values are from 24-hour equilibration.
(d) U^{238} determined from Th^{234} daughter 63 KeV γ-ray emission line assuming secular equilibrium.
(e) X-ray fluorescence measurements performed at Pacific Northwest National Laboratory.

Table 2.7. Composition of Artificial Hanford Groundwater (elemental concentration in mg/L), $pCO_{2(g)} = 10^{-3.5}$

GW	Ca^{2+}	Mg^{2+}	K^{+}	Na^{+}	HCO_3^{-}	SO_4^{2-}	NO_3^{-}	Alk. (meq/L)	Ionic Strength (mol/L)	Initial GW pH
2	24.1	4.9	3.9	359.9	610.2	172.9	192.2	10	0.0193	8.30
3	24.1	4.9	3.9	167.9	122.0	172.9	192.2	2	0.0113	8.40
4	24.1	2.4	3.9	191.9	244.1	115.3	192.2	4	0.0114	8.65
5	24.1	9.7	19.5	143.9	61.0	192.1	217.0	1	0.0115	8.07
6	24.1	12.2	19.5	131.9	30.5	201.7	217.0	0.5	0.0114	7.85
9	24.1	2.4	3.9	2,351.0	244.1	115.3	5,772.7	4	0.101	8.30

Table 2.8. Comparison of U(VI) Extraction Techniques

Sample	Surface Area (m^2/g)	Total U (mg/kg)[a]	Isotopic Exchange Extracted % of Total U[b]	Bicarbonate Extracted % of Total U[c]	Formate Extracted % of Total U[d]	AGW 4 Extracted % of Total U[e]	U K_d (mL/g)[f]
NPP 1-8	19.9	10.5	75.7	45.0	101.5	24.3	12.2
NPP 1-12	27.2	14.0	40.6	42.7	90.3	19.5	7.1
NPP 1-16	27.2	9.6	39.6	38.3	82.5	17.1	9.5
NPP 1-20	17.5	6.3	30.2	29.7	77.5	15.7	4.2
NPP 2-2	17.8	105.9	42.3	29.8	72.5	4.6	27.7
NPP 2-8	18.5	39.9	58.0	37.6	69.3	16.8	25.0
NPP 2-12	14.7	14.2	54.3	56.1	107.1	25.6	5.8
SPP 1-16	21.2	9.1	51.3	54.7	101.9	32.3	2.4
SPP 1-18	22.0	7.4	33.7	36.0	78.6	19.7	2.6
SPP 1-22	25.8	7.9	32.1	35.4	68.9	20.4	5.3
SPP 2-8	17.7	10.8	43.9	43.8	91.6	30.7	0.5
SPP 2-12	15.9	8.0	52.5	57.6	100.1	37.6	0.7
SPP 2-16	15.5	3.9	41.3	41.0	93.2	28.5	1.2
SPP 2-18	15.3	2.9	20.7	18.9	61.0	12.2	0.8
NPP 1-fines	46.9	21.0	42.8	41.4	78.3	22.1	17.8
SPP 1-fines	53.9	31.3	24.1	58.0	78.7	31.0	5.9
SPP 2-fines	40.5	13.3	47.8	39.9	75.8	26.8	8.0

(a) Total uranium determined from Th^{234} daughter 63 KeV γ-ray emission line assuming secular equilibrium.
(b) Isotopic exchange data from 24-hour time point.
(c) Bicarbonate extraction data from 72-hour time point.
(d) Formate extraction data from 72-hour time point.
(e) AGW 4 extraction data from 72-hour time point.
(f) U(VI) K_d calculated from isotopic exchange at 24-hour time point.

Table 2.9. Extractable Iron

Sample	[Fe] from DCB (µmol/g)	[Fe] in HH Extraction (µmol/g)	[Fe] in AMOX Extraction (µmol/g)	[Fe] in Formate Extraction (µmol/g)[(a)]
NPP 1-16	158	41	91	13.4
NPP 1-fines	296	102	108	13.0
SPP 1-fines	239	90	86	11.7
SPP 2-18	77	19	48	9.5
SPP 2-fines	232	83	70	13.2
(a) Formate extraction data taken at 72-hour time point.				

Table 2.10. Comparison of U(VI) Solubilized by Iron Extraction

Sample	HH Extracted % of Total U	Ammonium Oxalate Extracted % of Total U	Dithionite Citrate Bicarbonate Extracted % of Total U	Sodium Formate Extracted % of Total U[(a)]
NPP 1-16	92.2	81.7	100	82.5
NPP 1-fines	96.6	94.4	100	78.3
SPP 1-fines	91.6	91.6	99.2	78.7
SPP 2-18	58.3	50.0	66.7	61.0
SPP 2-fines	91.2	87.7	96.6	75.8
(a) Formate extraction data taken at 72-hour time point.				

Table 2.11. U(VI) Surface Reactions Considered in the Semi-Empirical, Generalized Composite Surface Complexation Models. (The models had no electrical double layer [EDL] terms or surface acidity constants.)

Reaction
$SOH + UO_2^{2+} = SOUO_2^{+} + H^{+}$
$SOH + UO_2^{2+} + H_2O = SOUOOH + 2H^{+}$
$SOH + UO_2^{2+} + H_2CO_3 = SOUO_2HCO_3 + 2H^{+}$
$SOH + UO_2^{2+} + H_2CO_3 = SOUO_2CO_3^{-} + 3H^{+}$
$SOH + UO_2^{2+} + H_2CO_3 + H_2O = SOUO_2OHCO_3^{2-} + 4H^{+}$
$SOH + UO_2^{2+} + 2H_2CO_3 = SOUO_2(HCO_3)_2^{-} + 3H^{+}$
$SOH + UO_2^{2+} + 2H_2CO_3 = SOUO_2(CO_3HCO_3)^{2-} + 4H^{+}$
$SOH + UO_2^{2+} + 2H_2CO_3 = SOUO_2(CO_3)_2^{3-} + 5H^{+}$
$SOH + UO_2^{2+} + 2H_2CO_3 + H_2O = SOUO_2OH(CO_3)_2^{4-} + 6H^{+}$

2.5 Advective Desorption and Adsorption Studies of Uranium with Contaminated Vadose Zone and Capillary Fringe Sediments

U(VI) is usually considered a mobile or semi-mobile contaminant at circumneutral pH (Read et al. 1993). U(VI) subsurface migration is especially promoted under mildly alkaline conditions of the Hanford 300 Area vadose zone (Serne et al. 2002), because stable neutral (Kalmykov and Choppin 2000; Bernhard et al. 2001) and/or anionic (Grenthe et al. 1992; Clark et al. 1995) uranyl carbonate aqueous complexes are usually formed under these conditions. Recent studies, however, have shown that uranyl carbonate species adsorb on hydroxylated minerals surfaces (Duff and Amrhein 1996; Bargar et al. 1999; Bargar et al. 2000), and the competition between aqueous and surface complexation controls the extent of U(VI) retardation in mildly alkaline environments (Qafoku et al. 2005).

The reaction characteristic time for U(VI) sorption and desorption, if slow relative to the fluid residence time, may be an important parameter that can be used to predict the long-term evolution of U(VI) plumes at Hanford. U(VI) adsorption to soil minerals and sediments was kinetically controlled and demonstrated a rapid initial phase (time scale of minutes) followed by a longer phase extending to hundreds of hours (Bargar et al. 2000; Braithwaite et al. 2000; Giammar and Hering 2001; Baik et al. 2004). In addition, U(VI) adsorption during unsaturated transport in a sandy sediment from Hanford was affected by rate limited mass transfer (Gamerdinger et al. 2001a; Gamerdinger et al. 2001b), and was far from equilibrium in a hydraulically saturated, goethite column at faster pore water velocities (Gabriel et al. 1998). However, few insights are offered in the literature on the rates of U(VI) adsorption and desorption in contaminated vadose zone sediments.

As shown in preceding sections of this report, the vadose zone and capillary fringe sediments collected from the four excavations in the NPP and SPP contain significant amounts of residual U(VI) ranging from <5 mg/kg to 238 mg/kg. Bicarbonate extractions (Davis and Curtis 2003) and isotopic exchange measurements in batch sediment suspensions with excess water reported in Sections 2.1 and 2.4 indicated that 4% to 67% of the sorbed U(VI) is labile and may be released to migrating pore waters. Moreover, release rate and extent in batch systems was shown to correlate with bicarbonate concentration (e.g., Figure 2.26) because of its effect on U(VI) aqueous speciation. Column studies under field-relevant water-rock ratios were consequently performed under saturated and unsaturated conditions to assess (1) the amount of sorbed U(VI) that may be released by vadose zone and capillary fringe sediments under conditions of water advection; (2) the U(VI) concentrations that may result in pore water/groundwater from such desorption/dissolution reactions; and (3) the extent of U(VI) adsorption and desorption that might occur in contaminant-free sediments.

Hydraulically saturated (Qafoku et al. 2003; Qafoku et al. 2004) and unsaturated (Gamerdinger et al. 2001a; Gamerdinger et al. 2001b) column experiments were initially performed with two capillary fringe sediments from the south (SPP2-18; <5.4 mg/kg uranium) and the north (NPP1-16; 11.6 mg/kg uranium) process ponds. These two sediments had some of the lowest sorbed uranium concentrations of any of the vadose zone materials sampled from beneath the 300 Area process ponds. Many of the advective experiments used a groundwater stimulant with pH = 8.05, sodium and calcium in approximate equal ratios, and 1.05 mmol/L of dissolved HCO_3. This electrolyte was identical to AGW #5 in Section 2.4. The composition of the electrolyte was varied in select experiments to evaluate the influence of pH and

bicarbonate concentration on desorption rate and extent. Flow rate and moisture content were also varied to evaluate the influence of fluid residence time, pore water velocity, and macro-pore desaturation on aqueous uranium concentrations. Stop-flow events, where the inflow of the leaching solution was stopped for various time periods, were used in the saturated flow experiments to asses whether uranium concentrations in the effluent solutions were in equilibrium with sorbed uranium in the sediments. The two 300 Area sediments differed in texture and mineralogy; NPP1-16 is finer textured and contains higher extractable Fe(III). Sorption experiments and K_d measurements reported in Section 2.4 indicate that NPP1-16 sorbs U(VI) approximately two times stronger than does SPP2-18. Other column leaching experiments are currently underway with sediments containing higher uranium concentrations (NPP2-4; 129 mg/kg uranium), but are not reported here.

2.5.1 Results

Saturated Column Studies. The desorption of uranium under saturated conditions was characterized by an initial increase to a maximum uranium concentration, followed by slowly decreasing concentrations with time in both sediments (Figures 2.28a and 2.29a). Desorption was slow and its trend differed between the NPP and SPP sediments. It also persisted after contact with significant water volumes (e.g., >100 pore volumes). Uranium concentrations released by NPP1-16 were lower than those released by SPP2-18, consistent with the higher sorptivity of the former sediment as measured in batch experiment (Section 2.4). The concentrations of uranium in the column effluents were influenced by sediment texture, mineral composition, and uranium content. Increasing the fluid residence time, and the pH and bicarbonate concentration all lead to significantly increased U(VI) effluent concentrations.

The effect of fluid residence time was particularly evident in Figures 2.28a and 2.29a; the noted spikes in U(VI) concentration during the leaching experiments occurred during events when the inflow of leaching solution was stopped. The pore fluids were in contact with the sediment particles for longer time periods during the stop flow events, and these longer equilibration times allowed more uranium to dissolve or diffuse from the sediment particles. Such behavior indicated that aqueous uranium in the column effluents was not in equilibrium with the solid phase and that its concentration was kinetically controlled. Such strong kinetic behavior was noted for all the 300 Area sediments studied (Qafoku et al. 2005).

All of the sediments studied could release U(VI) concentrations in excess of the maximum contaminant level (MCL) of 30 ppb (0.13 μmol/L) under certain conditions, even SPP2-18 that had low total U(VI) (Figures 2.28a and 2.29a). Slower pore water velocities and increased bicarbonate concentration over 1.0 mmol/L tended to elevate desorbed aqueous uranium concentrations to values above the MCL. Low uranium sediment SPP2-18 maintained effluent uranium concentrations in excess of the MCL for 10 saturated pore volumes. This volume of water significantly exceeds 300 Area recharge estimates for a 10-year period. The uranium-leaching behavior from the two capillary fringe sediments indicated that groundwater intrusion into the capillary fringe as promoted by river stage increases will solubilize sorbed uranium. The extent of uranium release will depend on the bicarbonate concentration of the groundwater and the length of time that it is in contact with the sediment.

The intrinsic adsorptivity of the capillary fringe sediments for U(VI) was investigated by injecting, a long pulse of a 0.3 μmol/L U(VI) solution (approximately 71 ppb) into columns of the SPP2-18 and NPP1-16 sediments, after most of the labile uranium contaminant had been removed (Figures 2.28b and 2.29b). U(VI) breakthrough curves exhibited a long plateau of relatively low U(VI) concentrations and an increasing limb associated with partial breakthrough in both these columns. Retardation was significant in both capillary fringe sediments. The plateau of low U(VI) concentrations was significantly longer in the NPP1-16 sediment (about 160 pore volume); although the NPP1-16 experiment is still in progress. The results showed that much more time was required to achieve a full U(VI) breakthrough in the NPP1-16 sediment, and that the sorption capacity of NPP1-16 was much greater than SPP2-18.

The lack of equilibrium attainment as suggested by sustained effluent concentrations with $C/C_0 < 1$ in both columns, indicated that U(VI) adsorption was kinetically controlled. In addition, desorption was also kinetically controlled since the U(VI) release curves exhibited long tails, and spikes in U(VI) concentration were observed after the stop-flow events applied during desorption (Figures 2.28a and 2.29a).

It was assumed that surface complexation was the primary sorption mechanism because U(VI) concentrations in the influent and effluent solutions were computed to be under saturated with respect to known U(VI) mineral phases. In addition, mass balance calculations confirmed the reversible nature of adsorption (in the short term adsorption-desorption experiment), since all adsorbed U(VI) was released in the column effluents of SPP2-18 during desorption. The surface complexation reaction likely involves the formation of U(VI) carbonate ternary surface species on hydroxylated edge sites of phyllosilicates which were common in the fines fraction of both sediments.

The column effluent data in Figures 2.28 and 2.29, and other similar column profiles that are not shown, were modeled with a nonequilibrium, distributed rate model (Culver et al. 1997, 2000). This model has been successfully used to describe time-limited processes in soils and sediments (Gustafson and Holden 1990; Connaughton et al. 1993; Pedit and Miller 1994; Pedit and Miller 1995; Chen and Wagenet 1997; Culver et al. 1997; Lorden et al. 1998; Pignatello 2000). The use of this numeric model is consistent with two alternative conceptual physicochemical models: (1) a chemically controlled system containing a large number of binding site groups that each exhibits comparable U(VI) sorptivity (e.g., K_d) but different desorption or sorption rates, or (2) a mass transfer controlled system containing a wide distribution of pore- or diffusional path-lengths. The model includes a thermodynamic end state for sorption that is currently described by K_d. This will be modified in the future to include explicit surface complexation reactions of the type described in Section 2.4.

As shown in Figures 2.28 and 2.29, the model could quantitatively describe the effluent data for both contaminant desorption and short-term adsorption/desorption experiments. The approach to equilibrium for both desorption and adsorption, that was experimentally observed to be slow, is described by a first order kinetic process. Instead of a single value for the first order rate constant, the model includes a statistical distribution of rate constants described by a gamma function. Two model parameters (β, η) describe the scale and shape of the rate constant distribution. A final model parameter, the labile uranium fraction, is needed to model uranium contaminant desorption as shown in Figures 2.28a and 2.29a.

The model parameters used to quantitatively describe the saturated column data are summarized in Tables 2.12 and 2.13. The computed desorption K_d values for SPP2-18 (14 L/kg) and NPP1-16 (50 L/kg) are similar to those measured in the batch experiments in Section 2.4 at comparable bicarbonate concentrations.

The gamma function takes a variety of shapes that skews toward high rates with increasing the value of the shape parameter (η) (Gustafson and Holden 1990; Connaughton et al. 1993). The low values of the shape parameter indicated that many of the conceptual site/pore groups exhibited small rate constants. The same η value was used for both U(VI) desorption experiments (Figure 2.28a), and the value of β (the scale parameter) was calculated for each of them (Table 2.12). The calculated mean rate constant $\acute{\alpha}$ ($\acute{\alpha} = \beta \times \eta$) was greater in the fast-flow column as expected for a physicochemical process driven by concentration gradients and/or free energy. The U(VI) desorption half-lives varied between 39 and 150 hours in the SPP2-18 sediment, while the half-life calculated for the NPP1-16 sediment was much larger (528 hours). They were longer than the half-lives of another Hanford sediment (6 to 63 hours) (Barnett et al. 2000), but were shorter than those measured in a calcareous soil (~10 years) (Braithwaite et al. 1997).

Greater K_d values (32 and 310 L/kg) than the ones obtained from fitting the contaminant-U(VI) desorption data, were needed to fit the short-term adsorption/desorption (SPP2-18) and adsorption (NPP1-16) breakthrough curves (Table 2.13). These K_d values are high for Hanford formation sediments and attest to the strong retardation potential of aquifer sediments in the uranium groundwater plume. The cause for the higher K_d values in the short-term experiments is not known, but is under current investigation. It is possible that the long-term leaching required to remove contaminant U(VI) dissolved carbonates that were blocking adsorption sites and maintaining elevated HCO_3^- concentrations. The average adsorption rate constants calculated with the gamma distribution model were greater than the desorption rate constant, indicating that sorption was faster than desorption. The larger β and smaller η values relative to desorption implied that a greater number of site/pore groupings exhibited more rapid rates during adsorption, which indicated that injected U(VI) sorbed to accessible surface sites that may or may not be the most energetic ones.

Mass transfer to and from poorly accessible sorbent domains within the sediment was responsible for the non-equilibrium behavior of U(VI) during sorption and desorption. As it presented in Section 2.2 of this report, microscopic evaluation of thin sections of the 300 Area sediments showed that sand grains and lithic fragments of various sizes were coated with thin layers of phyllosilicates such as smectite, vermiculite, and chlorite that were present in the clay fraction of these sediments. They may represent sorbent domains with limited accessibility that may influence U(VI) sorption/desorption rate and extent.

Unsaturated Column Studies. Previous studies of U(VI) sorption during unsaturated transport in Hanford sediments have shown that changes in retardation with water content did not follow predictions made with a constant K_d model (Lindenmeier et al. 1995; Kaplan et al. 1996). The two-region, U(VI) transport under unsaturated conditions, had a significant effect on U(VI) migration since U(VI) mass transfer between immobile and mobile water domains was diffusion limited (Gamerdinger et al. 2001a; Gamerdinger et al. 2001b).

A series of hydraulically-unsaturated column experiments were conducted to investigate the effect of water content on uranium release and migration, and to further quantify U(VI) fluxes that could emanate from the vadose zone as a result of the unsaturated leaching of uranium-containing sediments. The experiments were intended to assess whether differences existed in saturated and unsaturated leaching behavior and the causes for such behavior. Like the saturated column studies, the unsaturated leaching results are given in terms of U(VI) concentration (μmol/L) versus pore volume. The pore volume in the unsaturated case ($V/V_{o(u)}$) is smaller than the saturated one ($V/V_{o(s)}$), where $V/V_{o(u)} = f_s \cdot V/V_{o(s)}$, and $f_s = \Theta_{(u)}/\Theta_{(s)}$ is the fraction of water-filled pore space. Thus, an unsaturated column run at a given % saturation ($100 \cdot f_s$) has experienced the same volume of leaching solution to a saturated column with $V/V_{o(s)}$ at $(V/V_{o(u)})/f_s$.

The unsaturated leaching behavior of sediments SPP2-18 and NPP1-16 exhibited strong similarities to the saturated state (Figure 2.20). Generally, however the unsaturated effluent data showed greater variation and departure from smooth trends (e.g., Figure 2.30a), possibly as a result of small water content variations during the experiment. Uranium effluent concentrations from unsaturated sediment SPP2-18 reached a maximum concentration of 0.13 μmol/L ($f_s = 0.30$; 4-hour residence time) as compared to 0.165 μmol/L under saturated conditions. A similar comparison for NPP1-16 was 0.095 μmol/L under unsaturated conditions ($f_s = 0.45$) and 0.090 μmol/L when saturated. Peak uranium concentrations were reached in both unsaturated columns after 12-15 $V/V_{o(u)}$ as compared to 2.5-5.0 $V/V_{o(s)}$ under saturated conditions. This apparent delay or retardation in U(VI) leaching under unsaturated conditions was mainly a reflection of the different cumulative volume of bicarbonate containing solution that had passed through the columns.

Significant differences between saturated and unsaturated leaching behavior were observed when the saturation state was decreased to values more characteristic of the 300 Area vadose zone ($f_s = 0.21$; Figure 2.31). The U(VI) leaching profile in SPP2-18 at $f_s = 0.21$ was characterized by a retarded, sharp peak in concentration (up to 0.18 μmol/L) that began at an approximate $V/V_{o(u)} = 30$ and that persisted for approximately 30 more $V/V_{o(u)}$ (Figure 2.30a). Unlike all other columns, the release of uranium virtually ceased after this primary peak. The breakthrough of contaminant uranium at 30 $V/V_{o(u)}$ was delayed beyond that predicted from the saturated column data (25 $V/V_{o(u)}$) (Figure 2.29a versus 2.30a). Left shifting the $f_s = 0.21$ column data by 5 $V/V_{o(u)}$ allowed direct comparison (Figure 2.32) with the $f_s = 0.30$ column data from Figure 2.29a. Clear from this comparison (and calculated values from Figure 2.28) was the important observation that the extent of uranium release decreases with decreasing water content at comparable residence times. The percent of total uranium in SPP2-18 that was released in the two experiments after equal volumes of leaching solutions were passed through the columns was: 2.5% at $f_s = 0.30$, and 1.1% at $f_s = 0.21$. These differences reflect systematic variations in the pore water velocity and accessible volumetric domains at the three water contents.

Conversely, the uranium leaching profile in NPP1-16 at $f_s = 0.33$ was characterized by a sharp peak in concentration (up to 0.08 μmol/L) that began at approximately $V/V_{o(u)} = 10$ that persisted for approximately 30 more $V/V_{o(u)}$ (Figure 2.31b). This behavior was similar to that observed in NPP1-16 at $f_s = 0.45$ (Figure 2.31b). After equal volumes of leaching solutions were passed through the columns the total uranium released from NPP1-16 was: 3.8% at $f_s = 0.45$, and 1.2% at $f_s = 0.30$. The SPP2-18 sediment consisted of ~93% sand with the remaining 7% being composed of fine silt and clay. The NPP1-16 sediment, on the other hand, consisted of nearly 30% fine silt and clay, with only a 70% sand fraction.

This comparison illustrates the influence of sediment texture on hydraulic conductivity and contaminant release/migration. The high percentage of fine-textured particles in NPP1-16 dominates the sediment, promoting film flow along the fine particles. Therefore, the behavior of uranium migration is less affected by water content; yet, the total amount of uranium released remains a function of water content, decreasing with decreases in water content.

The column effluent data in Figures 2.30 and 2.31 were modeled with the nonequilibrium, distributed rate model, which was used to describe contaminant U(VI) desorption in the saturated column experiments presented in the preceding paragraphs. Rate parameters determined for saturated column experiments were used to model uranium release under unsaturated conditions. Two scenarios were considered: (1) the total uranium available for desorption was equal to the concentration of labile uranium, as constrained under saturated conditions, and (2) the total uranium available for desorption was equal to the concentration of labile uranium, linearly corrected for the degree of water saturation. This second scenario was found to yield better simulations of the unsaturated advective desorption behavior of deep, 200 A U(VI) contaminated sediments from the TX-104 uranium plume. The model parameters used to quantitatively describe the saturated column data are summarized in Table 2.13.

As shown in Figures 2.34 and 2.35b, the model could qualitatively describe the extended leaching of uranium from SPP2-18 at $f_s = 0.30$ and NPP1-16 at $f_s = 0.45$ and $f_s = 0.30$. However, in both sediments the initial spike in concentration was delayed by approximately 10 $V/V_{o(u)}$ from that predicted by the model. Moreover, the model over-estimated the extent of uranium released based on total uranium = labile uranium and under estimated the release of uranium when correcting the available uranium for the water saturation in SPP2-18 (Figure 2.32a). The model was unable to describe the release of uranium from SPP2-18 at $f_s = 0.21$ (Figure 2.33a). Model predictions for uranium release in the two sediments, as a function of decreasing water content, support the hypothesis that the flow regime within the NPP1-16 sediment, containing a high percentage of fine-textured particles, is maintained. However, a reduction in the fraction of reactive sites readily accessible by pore fluid is observed as the sediment is desaturated. Conversely, the flow regime within the SPP2-18 sediment, being dominated by coarse sand particles, is subject to greater variation in flow regime with decreasing saturation. The increasing delay in peak uranium concentrations within the SPP2-18 sediment as a function of decreasing water content suggests that more kinetically reactive sites, presumably associated with the smaller particles, are being accessed with decreasing water content. Hydro-dynamically, this is plausible because as a sediment desaturates the larger more conductive pores typically (composed of larger particles) drain first while flow is maintained through smaller pores. The modeling approach used in Figures 2.33 and 2.34 is clearly unsuitable and several new ones are being evaluated for their ability to describe the unsaturated advective desorption data.

2.5.2 Synopsis and Implications

The synopsis of findings from advective desorption and adsorption studies and their implications are as follows:

- Saturated and unsaturated leaching experiments were performed with two U(VI)-contaminated capillary fringe materials from the north [NPP1-16; 11.1 mg/kg U(VI)] and south [SPP2-18; <5.4 mg/kg U(VI)] process ponds. The experiments were intended to evaluate the concentrations of U(VI) that might develop in pore waters as a result of (1) surface recharge and infiltration and (2) groundwater height changes as a result of river stage fluctuations. Additionally the experiments evaluated the fraction of the total sorbed U(VI) that was labile to migrating fluids.

- U(VI) release from the sediments was found to be very slow and require extensive water volumes for even partial removal of the sorbed U(VI) pool. U(VI) desorption was found to be a kinetic and not an equilibrium process. Long term leaching experiments removed only 1 to 8% of the total U(VI); leaching extent increased with increasing water saturation.

- All of the materials studied leached U(VI) at concentrations in excess of the MCL for extended pore volumes when realistic fluid residence times (water flow rates) were applied under water saturated conditions. However, maximum effluent U(VI) concentrations did not exceed 0.4 μmol/L (95.2 ppb).

- While desorption extent decreased with decreasing water content, leached concentrations in the effluent pore waters tended to be higher in SPP2-18. However, in NPP1-16 the extent of desorption decreased with decreasing water content and the pore water concentrations were observed to decrease. The importance of sediment texture on uranium desorption increases with decreasing water content.

- A distributed rate model (DRM) could well describe the leaching behavior of U(VI) under saturated conditions. Equilibrium-based models were not effective. Desorption K_d values were found to be 14 L/kg for SPP2-18 and 50 L/kg for NPP1-16 when $[CO_3]_{TOT}$ = 1.05 mmol/L. The DRM has potential to predict U(VI) concentrations in saturated advective system as a function of residence time.

- Saturated column DRM parameters (K_d and rate parameter distribution) differed between contaminant U(VI) desorption and short-term U(VI) adsorption. Long-term leaching promoted this effect whose cause is under further study.

- DRM parameters developed under saturated conditions did not provide good descriptions of unsaturated uranium leaching regardless of hypothesis or assumption.

- The unsaturated leaching behavior of sorbed uranium is more complex than expected and additional experiments are needed to understand its behavior.

Table 2.12. Distributed Rate Model Parameters for Modeling Bromine and Uranium Desorption Breakthrough Curves

Parameter	Unit	Slow-Flow Column	Fast-Flow Column	Source
SPP2-18				
Porosity		0.4	0.4	Measured
Bulk density	g/cm^3	1.66	1.66	Measured
Column length	cm	14.5	14.5	Measured
Pore velocity	cm/h	1.54	13.3	Measured
Dispersion coefficient	cm^2/h	2.15	6.11	Fit to Br data
Dispersity	cm	1.40	0.46	Calculated
Labile U	mol/g	2.68×10^{-9}	2.68×10^{-9}	Measured
K_d	L/kg	14	14	Fit to U data
β (scale factor)	l/h	0.011	0.042	Fit to U data
η (shape factor)		0.42	0.42	Fit to U data

Parameter	Unit	Value	Source
NPP1-16			
Porosity		0.47	Measured
Bulk density	g/cm^3	1.45	Measured
Column length	cm	14.5	Measured
Pore velocity	cm/h	10.97	Measured
Dispersion coefficient	cm^2/h	2.47	Fit to Br data
Dispersity	cm	0.23	Calculated
Labile U	mol/g	1.76×10^{-8}	Measured
K_d	L/kg	50	Fit to U data
β (scale factor)	l/h	0.0041	Fit to U data
η (shape factor)		0.32	Fit to U data
Injected chemical conditions: pH 8.0; carbonate = 1.045 μmol/L, U(VI) = 0 μmol/L, and ionic strength = 0.05 mol/L).			

Table 2.13. Distributed Rate Model Parameters for Modeling Uranium Adsorption and Desorption in Short-Term Contaminated Sediments

Parameter	Unit	Slow-Flow Column Value	Source
SPP2-18			
Porosity		0.4	Measured
Bulk density	g/cm^3	1.66	Measured
Column length	cm	14.5	Measured
Pore velocity	cm/h	1.54	Measured
Dispersion coefficient	cm^2/h	2.15	Fit to Br data
Dispersity	cm	1.40	Calculated
K_d	L/kg	32	Fit to U data
β (scale factor)	l/h	0.065	Fit to U data
η (shape factor)		0.22	Fit to U data
Parameter	Unit	Value	Source
NPP1-16			
Porosity		0.47	Measured
Bulk density	g/cm^3	1.45	Measured
Column length	cm	14.5	Measured
Pore velocity	cm/h	10.97	Measured
Dispersion coefficient	cm^2/h	2.47	Fit to Br data
Dispersity	cm	0.23	Calculated
K_d	L/kg	310	Fit to U data
β (scale factor)	l/h	0.041	Fit to U data
η (shape factor)		0.32	Fit to U data
Injected chemical conditions: pH 8.0; carbonate = 1.045 µmol/L, U(VI) = 0.35 and 0 µmol/L, and ionic strength = 0.05 mol/L).			

Table 2.14. Distributed Rate Model Parameters for Modeling Unsaturated Uranium Desorption Breakthrough Curves

Parameter	Unit	Low-Sat. Column Value	High-Sat. Column Value	Source
SPP2-18				
Bulk density	g/cm^3	1.64	1.63	Measured
Column length	cm	6.0	6.0	Measured
Pore velocity	cm/h	1.22	1.52	Measured
Dispersion coefficient	cm^2/h	2.71	2.28	Fit to Sat. Br
Labile U	mol/g	2.68×10^{-6}	2.68×10^{-6}	Measured
Labile U* degree water saturation		5.63×10^{-7}	8.04×10^{-7}	Calculated
K_d	L/kg	14	14	Fit to Sat. U
β (scale factor)	l/h	0.011	0.42	Fit to Sat. U
η (shape factor)		0.011	0.42	Fit to Sat. U

Parameter	Unit	Value		Source
NPP1-16				
Bulk density	g/cm^3	1.32	1.63	Measured
Column length	cm	6.0	6.0	Measured
Pore velocity	cm/h	1.63	1.52	Measured
Dispersion coefficient	cm^2/h	0.37	2.28	Fit to Sat. Br
Labile U	mol/g	1.76×10^{-8}	1.76×10^{-8}	Measured
Labile U* degree water saturation		5.81×10^{-9}	7.92×10^{-9}	Calculated
K_d	L/kg	50	50	Fit to Sat. U
β (scale factor)	l/h	0.0041	0.0041	Fit to Sat. U
η (shape factor)		0.32	0.32	Fit to Sat. U
Injected chemical conditions: pH 8.0; carbonate = 1.045 μmol/L, U(VI) = 0 μmol/L, and ionic strength = 0.05 mol/L).				

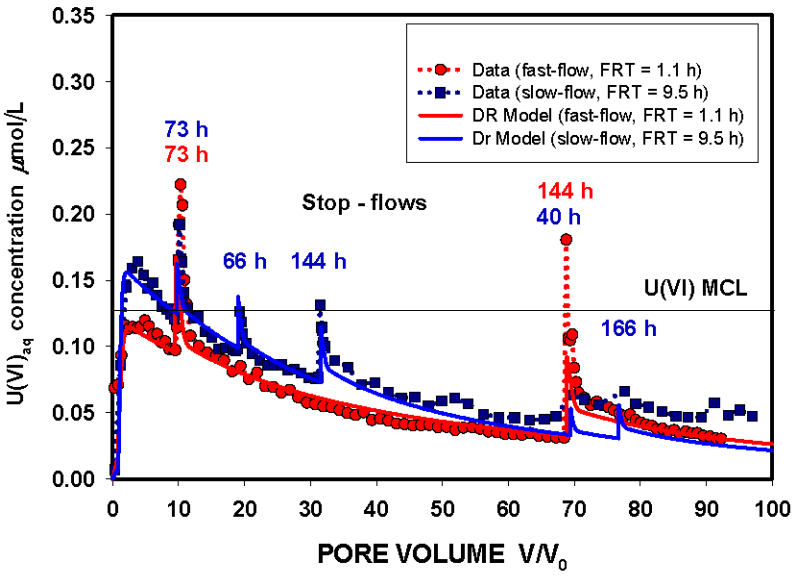

(a)

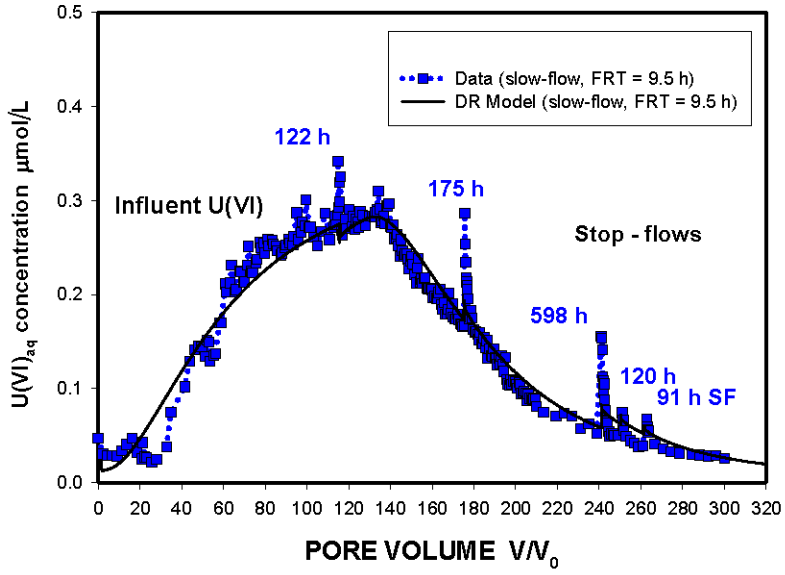

(b)

Figure 2.28. Saturated Column Desorption Data (a) for SPP2-18 at Two Different Fluid Residence Times (FRT = 1.1 and 9.5 h) and Adsorption and Desorption (b) of Injected U(VI) (FRT of 9.5 h). (Spikes in U(VI) concentration occur at stop flow events. Solid lines are calculations using the distributed rate model. The leaching solution was a mixed calcium, magnesium, sodium electrolyte with pH = 8.05 and $[CO_3]_{TOT}$ = 1.05 mmol/L.)

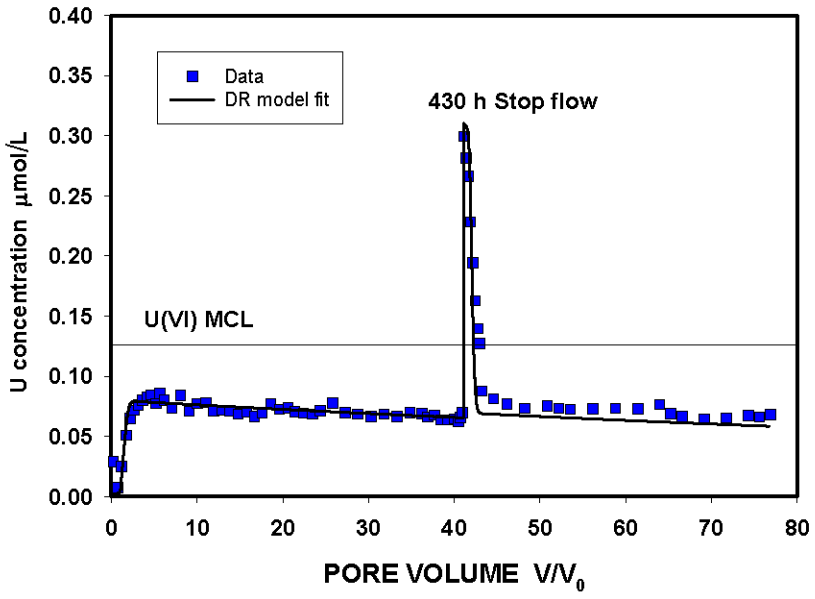

(a)

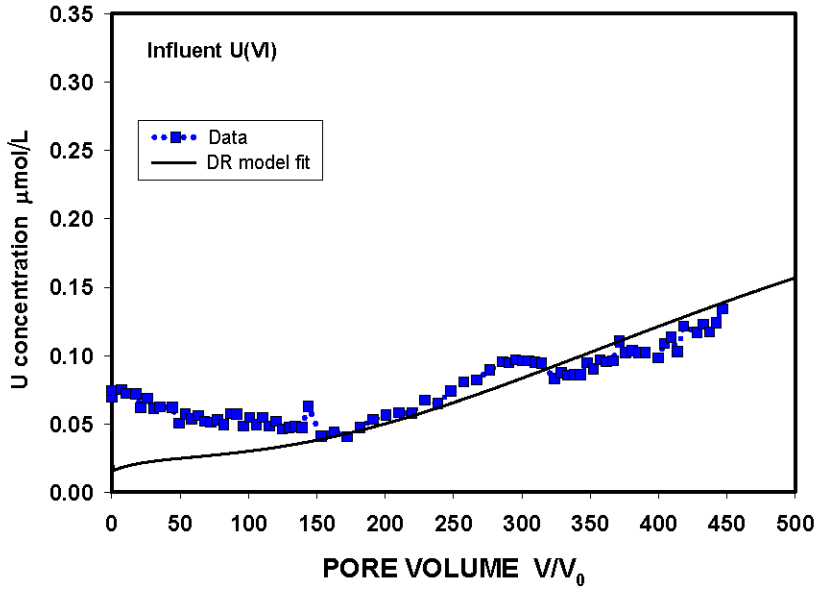

(b)

Figure 2.29. Saturated Column Desorption Data (a) for NPP1-16 at a Fluid Residence Time of 1.32 hours and Adsorption (b) of Injected U(VI). (Spike in U(VI) concentration occurs at stop flow event. The solid line represents calculations using the distributed rate model. The leaching solution was a mixed calcium, magnesium, sodium electrolyte with pH = 8.05 and $[CO_3]_{TOT}$ = 1.05 mmol/L.)

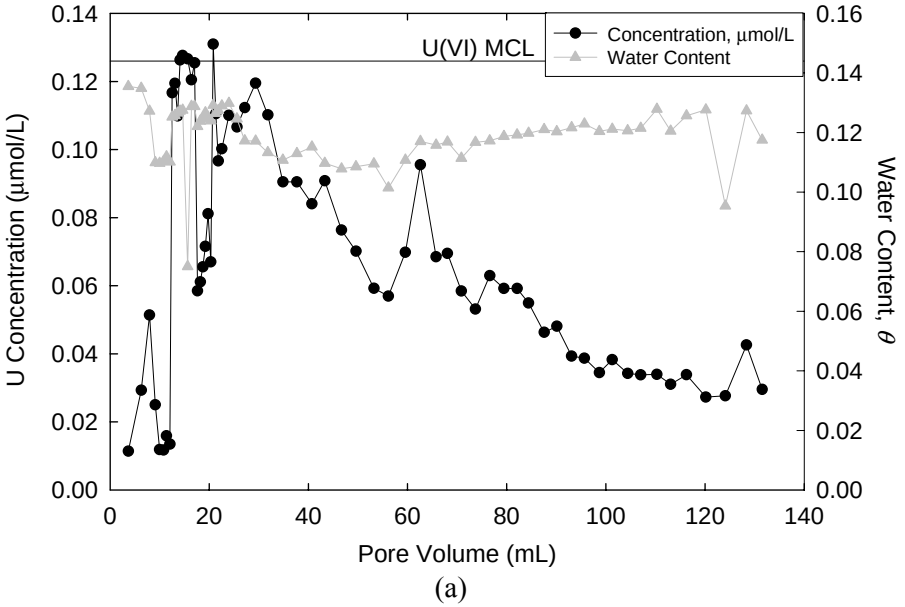

(a)

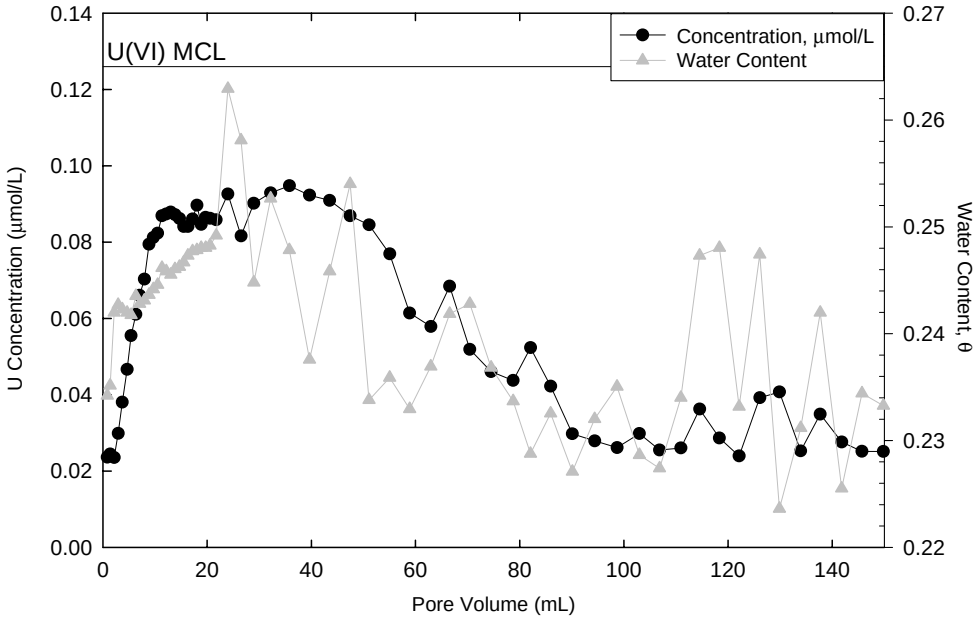

(b)

Figure 2.30. (a) Unsaturated Leaching of U(VI) from Sediments SPP2-18 at 30% Water Saturation and 4-Hour Fluid Residence Time and (b) NPP1-16 at 45% Water Saturation and 3-Hour Fluid Residence Time

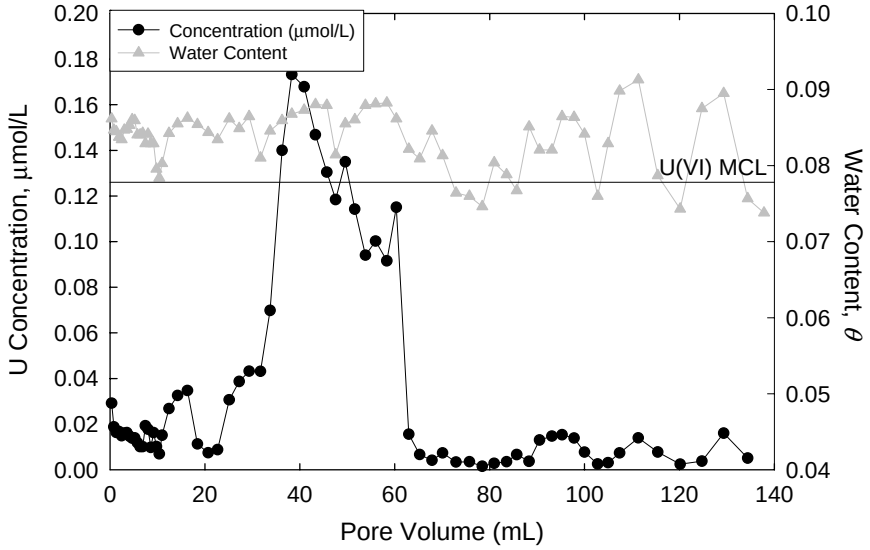

(a)

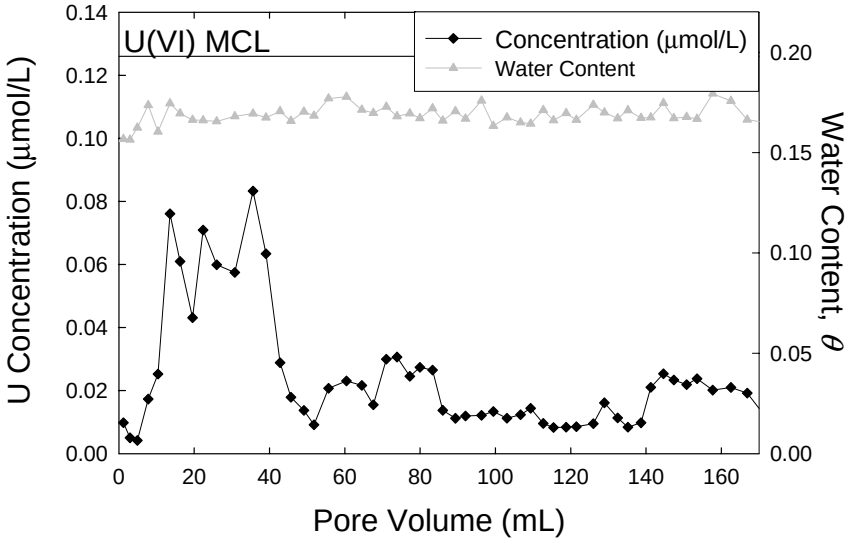

(b)

Figure 2.31. (a) Unsaturated Leaching of U(VI) from Sediments SPP2-18 at 21% Water Saturation and 5-Hour Fluid Residence Time and (b) NPP1-16 at 33% Water Saturation and 4-Hour Fluid Residence Time

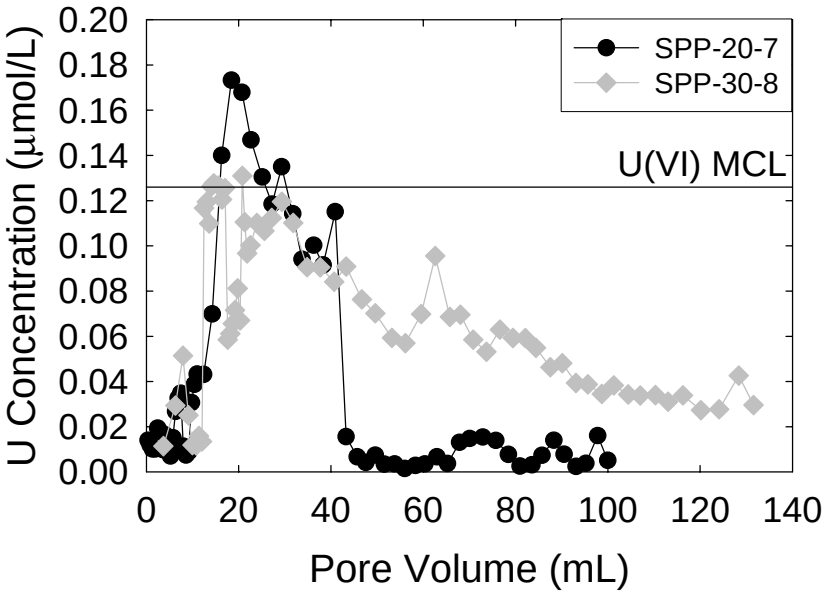

Figure 2.32. Comparison of U(VI) Leaching from the SPP2-18 Sediment at 30% (SPP-30-8) and 21% (SPP-30-8) Water Saturation. (The 21% curve has been left-shifted 5 pore volumes to allow comparison of the total uranium leached from both columns.)

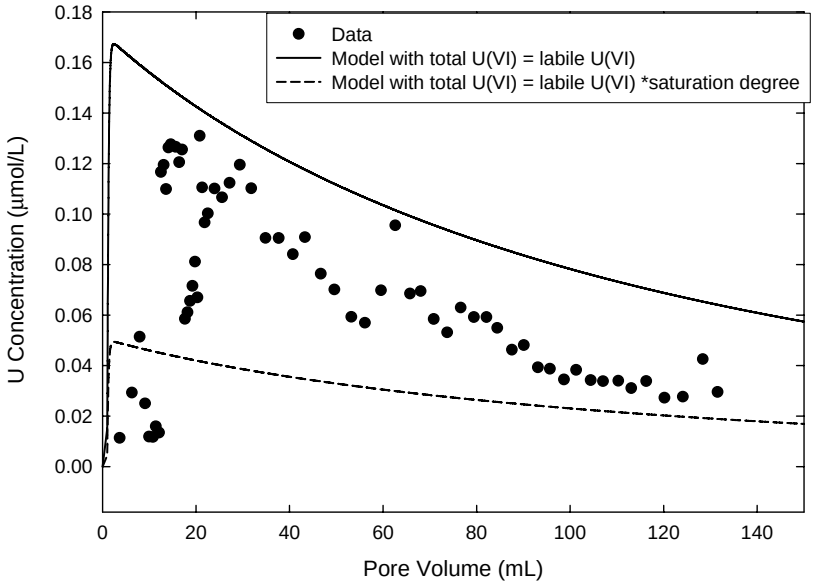

(a)

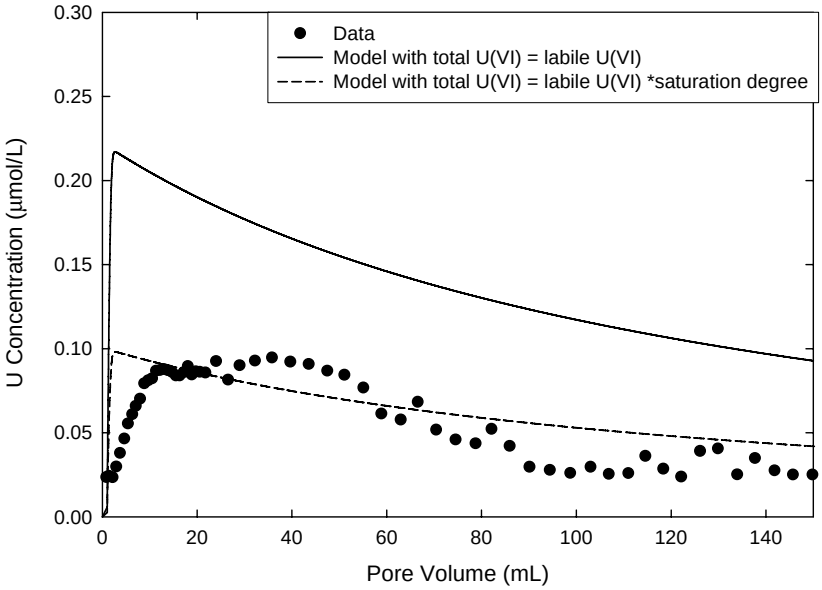

(b)

Figure 2.33. (a) Unsaturated Leaching of U(VI) from Sediments SPP2-18 at 30% Water Saturation and 4-Hour Fluid Residence Time and (b) NPP1-16 at 45% Water Saturation and 3-Hour Fluid Residence Time. (Solid lines are calculations using the distributed rate model with the total uranium concentration equal to the labile uranium concentration. Broken lines are calculations using the distributed rate model with the total amount of uranium equal to the labile uranium linearly corrected for the degree of water saturation.)

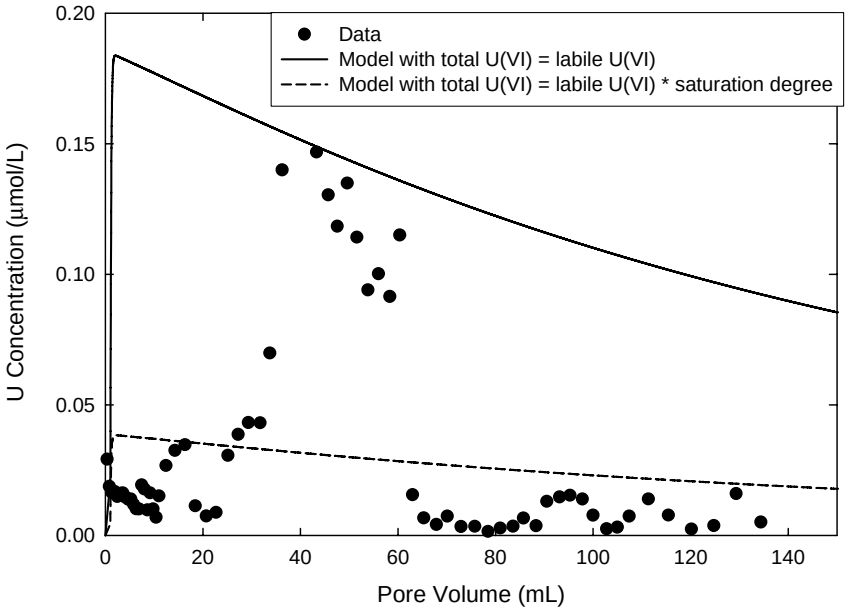

(a)

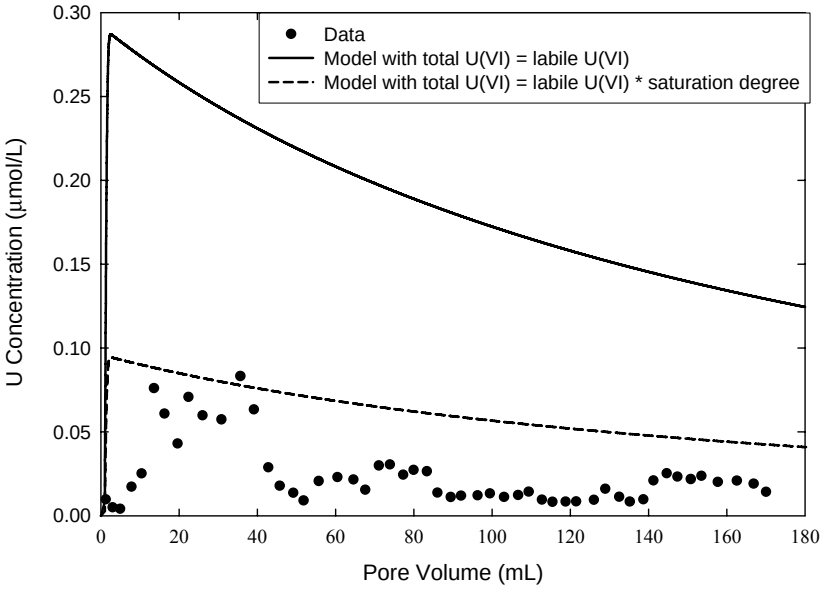

(b)

Figure 2.34. (a) Unsaturated Leaching of U(VI) from Sediments SPP2-18 at 21% Water Saturation and 5-Hour Fluid Residence Time and (b) NPP1-16 at 33% Water Saturation and 4-Hour Fluid Residence Time. (Solid lines are calculations using the distributed rate model with the total uranium concentration equal to the labile uranium concentration. Broken lines are calculations using the distributed rate model with the total amount of uranium equal to the labile uranium linearly corrected for the degree of water saturation.)

2.6 Variably Saturated Flow and Transport Modeling in the 300 Area[1]

Researchers at PNNL developed a variably saturated, two-dimensional subsurface flow model for a west-east vertical cross section perpendicular to the Columbia River, between well 399-6-1 and an island offshore from the 300 Area. Model simulations were performed with the Subsurface Transport Over Multiple Phases (STOMP; White and Oostrom 2000, 2004) multi-fluid simulator, using the Richard's equation solution mode. The simulations included water flux and hypothetical, conservative tracers associated with groundwater and river water to better understand the nature of mixing of these waters in the area near the river. Hourly water levels at well 399-6-1 and river gauge SWS-1 are the primary boundary conditions driving the flow field. The two-dimensional cross section passes through wells 399-6-1, 399-3-2, 399-3-3, 399-3-11, and the 300 Area river gauge SWS-1, which makes spatial interpolation of boundary conditions unnecessary and affords several observation locations to compare hydrologic, transport, and chemistry information (Figure 2.35).

The 88,910-cell grid (62,536 active cells) currently covers a model domain of 1,400 m lateral and 62 m vertical. This encompasses a 200-meter-wide river channel and half of the island close to the Hanford shore. A total of six geologic units are represented, including basalt (Figures 2.36 and 2.37). Variable grid spacing is used with the finest discretization specified in the hyporheic zone with 0.5 m by 0.5 m resolution. Hydraulic properties, summarized in Table 2.15, are based primarily on the current characterization effort by M.L. Rockhold and P.D. Thorne (PNNL). Basalt properties including recharge are based on the model for Hanford Site-Wide Assessment with the System Assessment Capability.

In the current model, measured hourly water levels for a one year period (March 1, 1992, to February 28, 1993) in well 399-6-1 and river gauge SWS-1 were the principal boundary conditions for the flow field (Figure 2.38). The model was run with three different schemes for temporal averaging of the water level data to investigate the effect of boundary condition (BC) timescale on the results. For the hourly BC case, the hourly data was used directly. For the daily and monthly BC cases, the hourly data for each period was averaged, and the mean was assigned to the midpoint of the period (for example, the mean value of groundwater head at the western boundary during the month of January was specified at day 15.5 of that month). The user-specified time step in STOMP was set at half-hour intervals for the hourly BC case and 1-hour intervals for the daily and monthly BC cases. STOMP used linear interpolation to derive the BCs at each time step that fell between available input BCs and used internal time stepping when needed to obtain solution during times of rapid change.

Other hydraulic BCs included surface recharge of 60 mm/year (based on the last 23 years of the 300 Area (Gee et al. 2005), upward recharge from the basalt aquifer of 0.9 mm/yr (Vermeul et al. 2003), and a no-flux east boundary that represents a groundwater divide at the center of the island in the Columbia River (Figure 2.37). Groundwater tracer concentration BCs were 1.0 at the west and bottom boundaries (groundwater inflow) and 0 at the top boundary (meteoric recharge) and river. River water tracer concentration BCs were 1.0 at the river and 0 everywhere else. The interface between the river and

[1] This section is a summary of Waichler and Yabusaki (2005).

the aquifer (both main shore and island) was simulated in STOMP as a seepage face. Water flux and river tracer flux may occur by both advection and diffusion from the river into the aquifer. Water, groundwater, and river tracer may flux from the aquifer into the river.

The model was run with the same year of boundary conditions repeated four times, so that by the end of the fourth year, the model was in a dynamic steady-state and simulated response was the same on an inter-annual basis. Following this model run, one additional year was simulated to provide output for the reported results.

2.6.1 Results

Preliminary simulations have shown that the principal flow path of groundwater to the river is within the Hanford formation (Figure 2.39). Simulated flow in the basalt and Ringold mud units is predominantly vertical (upward) and has velocities that are over four orders of magnitude smaller than the Hanford and Ringold C/E units. Groundwater velocities near the island are also small because of the groundwater divide.

The flow and transport behavior simulated in the 300 Area aquifer is driven primarily by the temporal variation in the Columbia River stage. While there is a general seasonal trend of a primary river stage peak in May to June and a secondary peak in December to January, the system is dominated by high frequency diurnal fluctuations that are principally the result of water released through the hydroelectric dam turbines to match real-time power generation needs. The magnitude of these diurnal river stage fluctuations can, on occasion, exceed the seasonal fluctuation of monthly average river stages (Figure 2.38). Water levels in the 300 Area aquifer respond rapidly to these diurnal fluctuations. During the course of a month, water levels in wells over a kilometer from the river (e.g., well 399-6-1) have several (~5) discernible but considerably damped peaks, each associated with the occurrence of a significant river stage peak followed by a significant drop (Figure 2.38).

In contrast to the relatively long distance that the pressure wave propagates into the aquifer from the river, the intrusion of river water into the aquifer (indicated by reduction in specific conductivity measurements in the 300 Area wells) is generally limited to a zone near the river. Notable exceptions are for infrequent high river stage events (e.g., 1997 and 2002) when significant drops in the conductivity measurements were detected ~350 m from the river (e.g., 399-1-17A).

The hourly hydraulic head at the model boundaries for a day in November shows that the river level can change up to 1.2 m on a daily basis (Figure 2.40). The simulated velocity fields showed a high degree of responsiveness to these river stage fluctuations, with the highest velocities associated with the Hanford formation sediments (Figures 2.41 and 2.42). Within 300 m of the river, where all principal disposal facilities are situated, pore velocities in the Hanford formation responding to a single diurnal cycle of river stage fluctuations exceeded 5 m/d to and from the river. Sustained velocities in any direction were typically not maintained over the course of a day in this zone.

In this preliminary one-year simulation, the calculated water influx to the model domain included meteoric recharge of 64.3 m^3/yr per meter width, basalt recharge of 1.3 m^3/yr per meter width, and inflow from the west aquifer boundary of 116.1 m^3/yr per meter width. This was balanced by the predicted aquifer effluent to the river of 181.7 m^3/yr per meter width.

Predicted hourly and cumulative fluxes of water and the two tracers across the riverbed surface are shown in Figure 2.43. Forcing the model with hourly boundary conditions resulted in frequent direction and magnitude changes of net water flux across the riverbed. In comparison, the fluctuations resulting from the daily and especially monthly boundary conditions were predicted to be considerably damped. A similar pattern held for the river tracer, which entered the aquifer and then returned to the river later. By design, the groundwater tracer only moved into the river (assumed total dilution prevents it from moving back into the aquifer). The cumulative flux rates shown include the absolute values of the negative hourly fluxes, so that the cumulative fluxes increase monotonically. The hourly boundary condition case predicted a much greater flux back and forth across the riverbed.

Although the year-end fluxes are similar for the different BC timescales, the size of the mixing zone in the near-shore area is very sensitive to the BC timescale (Figure 2.44). The extent of river water intrusion into the aquifer is much greater for the hourly BC case and almost non-existent for the monthly BC case.

Hourly data was not available for any of the wells that are close to the cross section line and at some distance from the boundary points. However, the hourly dataset did include well 399-3-12, which is located 140 m north of the cross section, and x = 687 m along the cross-section line. The simulated water-table height at this location was linearly interpolated from the model output for the nodes x = 650 and x = 725 (Figure 2.45). The difference (simulated - observed) had the following statistics: minimum of -5.6 cm; mean of 9.25 cm; and maximum of 25 cm. The coefficient of variation (standard deviation/ mean) for the difference was 54%.

2.6.2 Synopsis and Implications

The synopsis of findings from variably saturated flow and transport modeling and their implications are as follows:

- The two-dimensional flow and transport modeling studies were based on the most current characterization of material properties available for the 300 Area sediments and hourly water levels observed in the river and aquifer in 1992 to 1993. While river stage in the 300 Area is always measured at an hourly interval, there are no commensurately comprehensive hourly datasets available for the 300 Area wells, other than the 1992-1993 dataset.

- The high degree of responsiveness of the aquifer to the river BC predicted with the model underscores the importance of using hourly water levels. Simulations based on hourly water level BCs predicted an aquifer-river water mixing zone that reached 150 m inland from the river. On the other hand, simulations based on daily and monthly averaging of the hourly water levels at the river and interior model boundaries were shown to significantly reduce predicted river water intrusion into the aquifer, resulting in under estimation of the volume of the mixing zone. Because the river is

distinctly more dilute than typical aquifer water chemistry and uranium mobility is sensitive to changing solution chemistry, river water intrusion into the aquifer is a critical issue for uranium transport, Geochemical modeling based on the SCM in Section 2.4 predicted that for the same level of uranium contamination in sediments, the equilibrium aqueous uranium concentration in an aquifer solution can be 2 orders of magnitude higher than a river water solution.

- It is important to recognize that the predicted efflux of 181.7 m^3/yr per meter width to the river is the net flow across the riverbed or aquifer-river interface (i.e., the difference between the total influx and the total efflux). The total annual influx and total annual efflux with respect to the river and based on the hourly water level boundary conditions were 3,002 m^3 and 2,821 m^3 per meter width, respectively. The fact that the net flux is almost 2 orders of magnitude smaller than the total of the fluxes that it was derived from shows that the large swings in velocity during diurnal river stage cycles dominate the hydrologic system.

- Based on the current material property specifications in the model, groundwater flow in the basalt and the Lower Ringold Mud unit are 10,000 times smaller than the Hanford formation and Ringold C/E units. These results may provide the impetus for possibly eliminating the low-flux basalt and Lower Ringold Mud units from the grid, and using the bottom of the Ringold Gravel/Sand/Silt (B/D) unit as the lower model boundary. Similarly, the inclusion of the island to the east of the river channel in the model domain does not appear to materially change the flow and transport behavior to the river from the aquifer, as seen in the velocity vector plot. Subsequent modeling studies will used to determine an appropriate location for the east boundary of the domain.

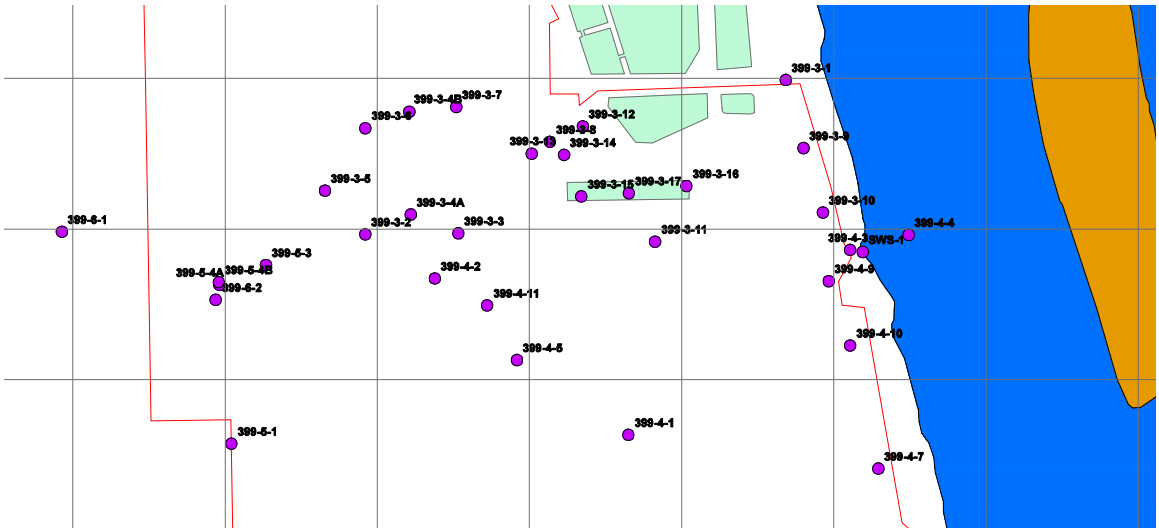

Figure 2.35. Location Map Showing 300 Area in Vicinity of Simulated Cross Section

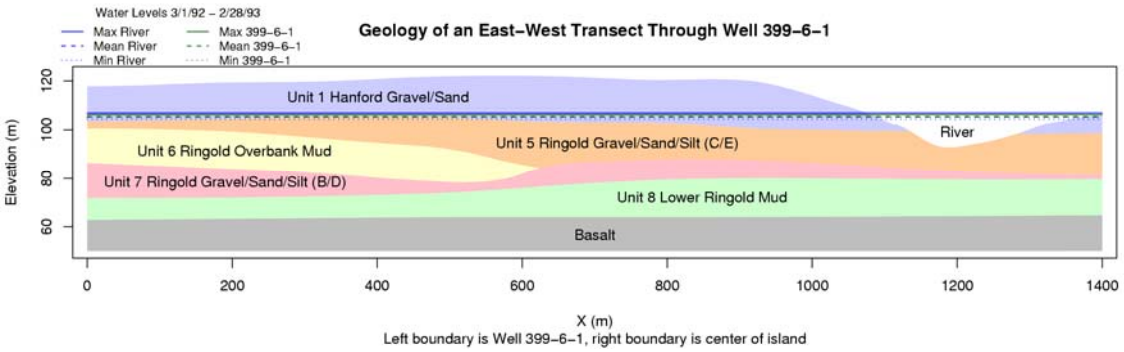

Figure 2.36. EarthVision Geology for 300 Area Vertical Two-Dimensional Cross Section and Representative Water Levels

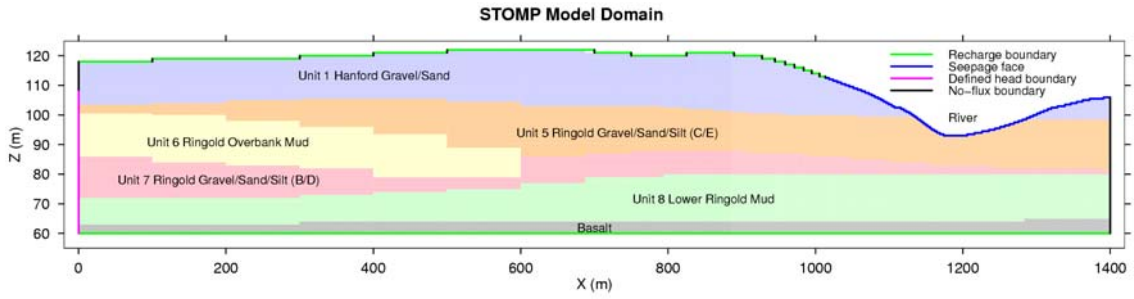

Figure 2.37. Discretized Geology and STOMP Boundary Condition Types for Two-Dimensional Flow Model

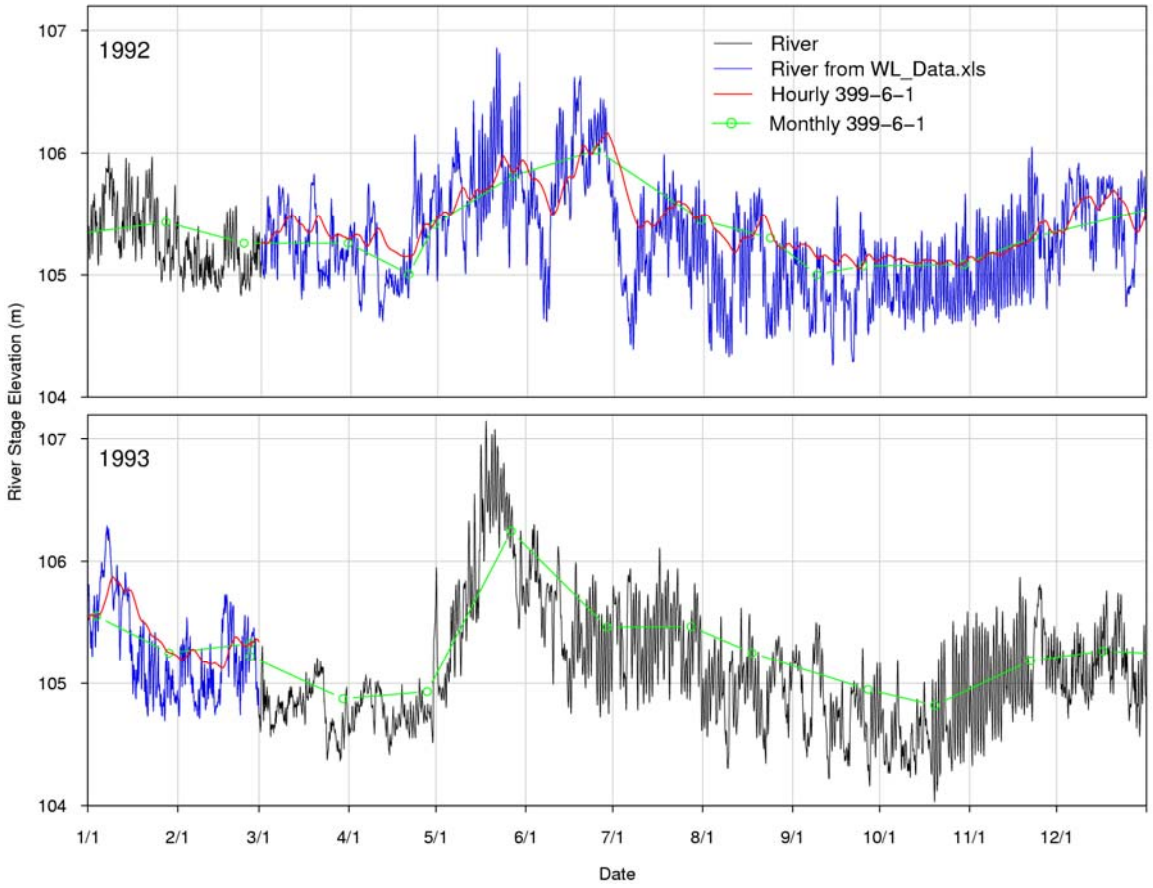

Figure 2.38. Hydraulic Head at River (SWS-1) and Well 399-6-1. (Blue line is hourly river boundary condition and red line is hourly groundwater boundary condition used in model.)

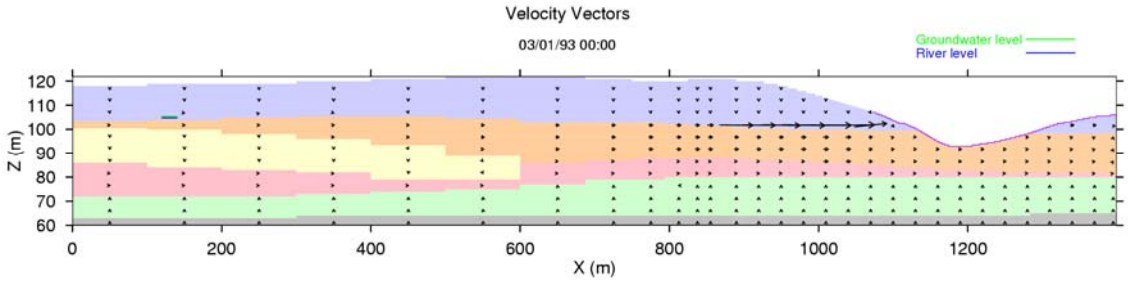

Figure 2.39. Darcy Velocity Vectors at End of Simulation (March 1, 1993) for Hourly Boundary Conditions (Case 6). (Arrow shaft lengths are directly proportional to magnitude. Absence of arrow shaft indicates zero or very low velocity.)

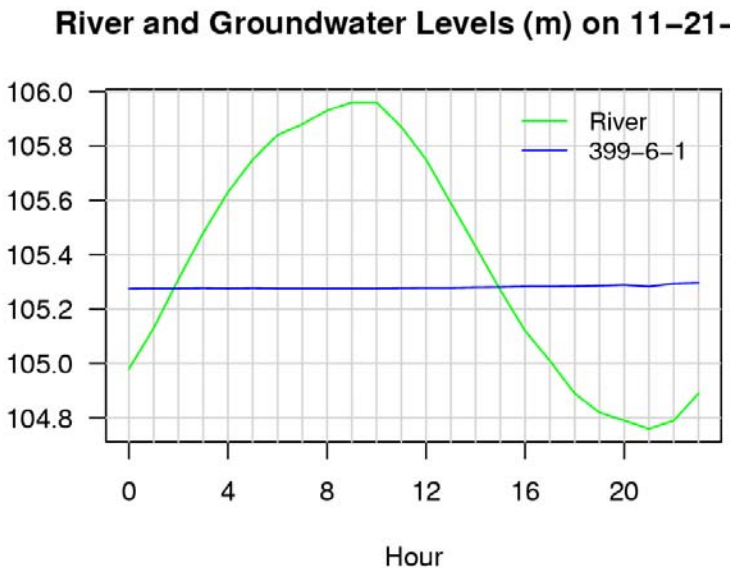

Figure 2.40. Hourly Hydraulic Head Boundary Conditions During November 21, 2004

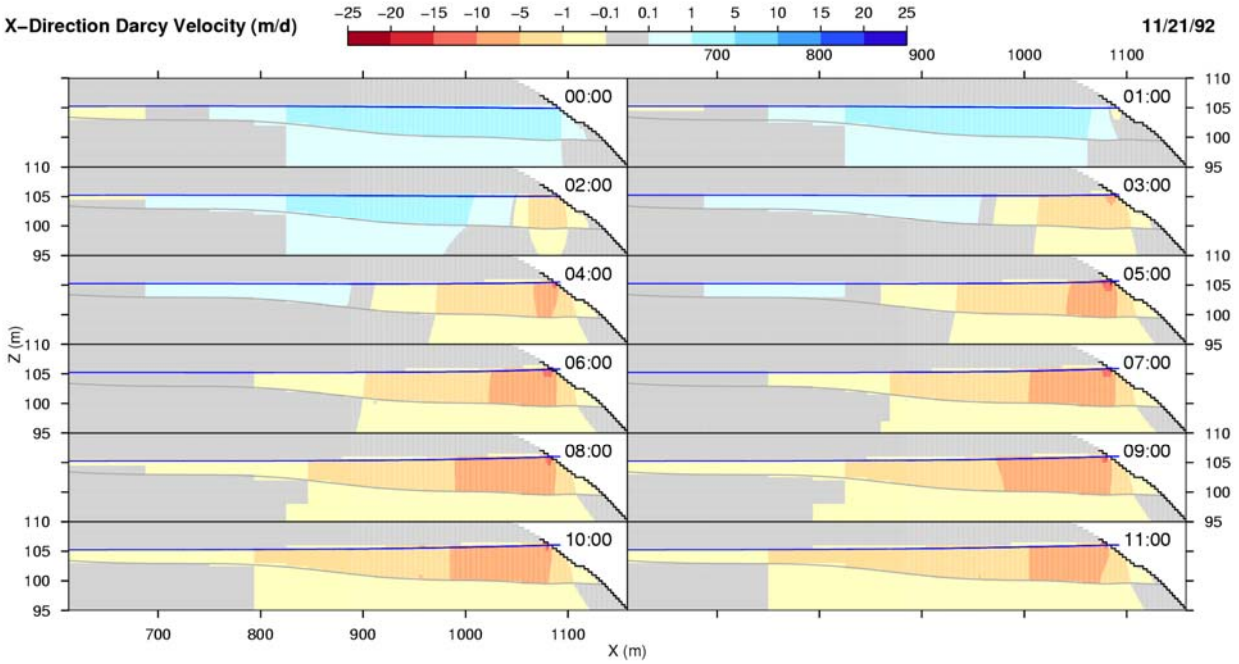

Figure 2.41. Hourly X-Direction Darcy Velocity for Near-Shore Region During First Half of November 21, 1992. (Red-to-yellow hues indicate negative velocity [away from river] and blue hues indicate positive velocity [towards the river]. Velocity is given in meters per day.)

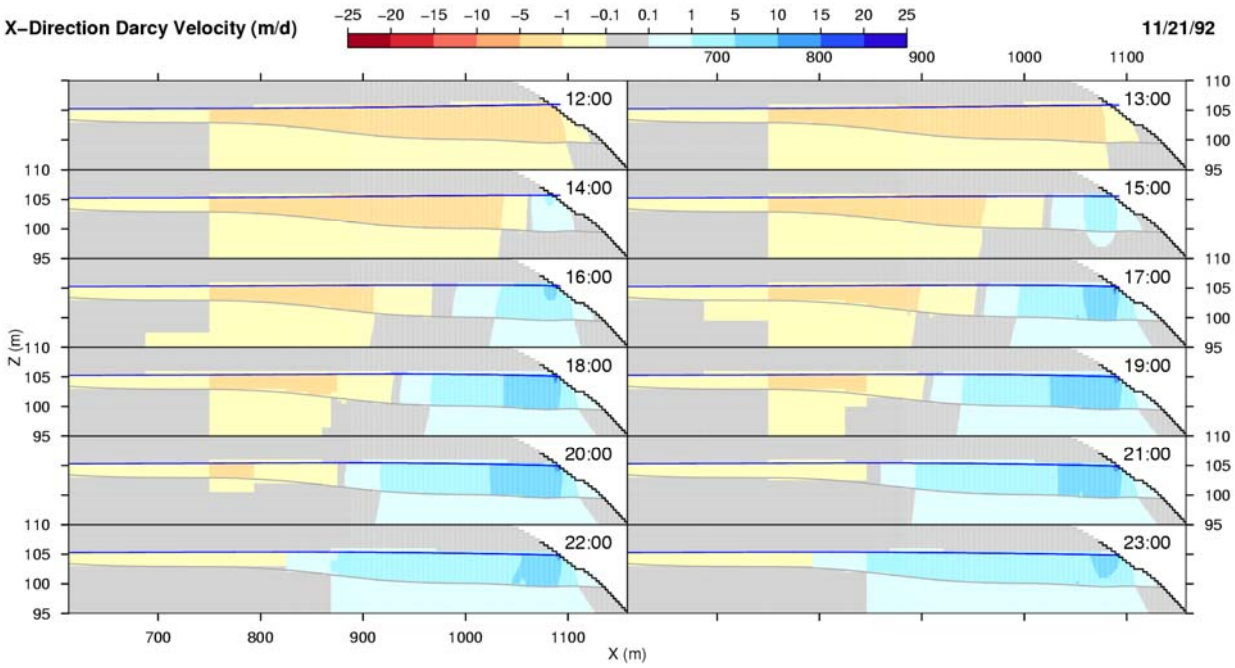

Figure 2.42. Hourly X-Direction Darcy Velocity for Near-Shore Region During Second Half of 11/21/92. (Red-to-yellow hues indicate negative velocity [away from river] and blue hues indicate positive velocity [towards the river]. Velocity is given in meters per day.)

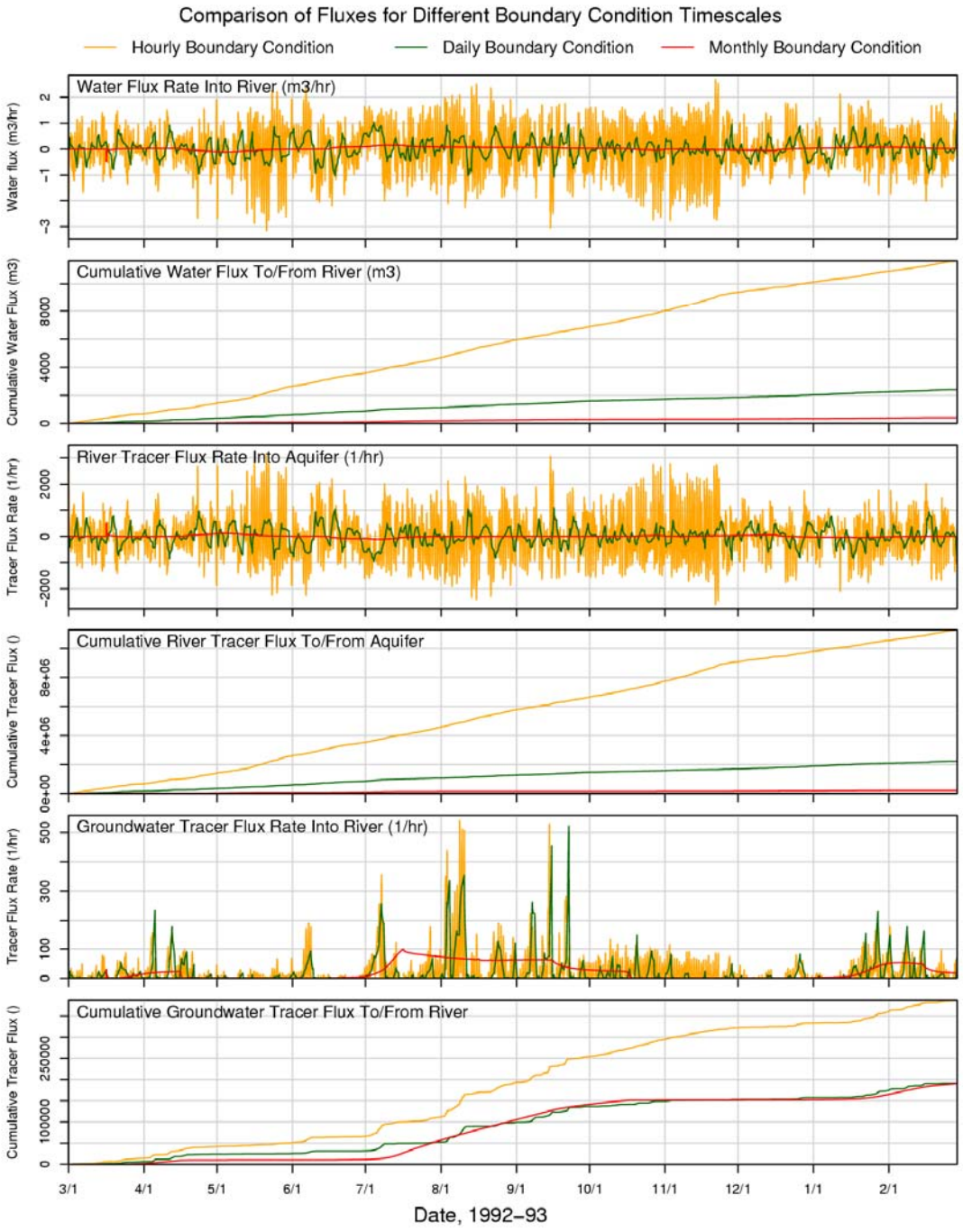

Figure 2.43. Comparison of Simulated Water and Tracer Fluxes for Different Boundary Condition Timescales. (Cumulative fluxes are based on the absolute value of the hourly fluxes—negative fluxes are counted as positive in the cumulative values.)

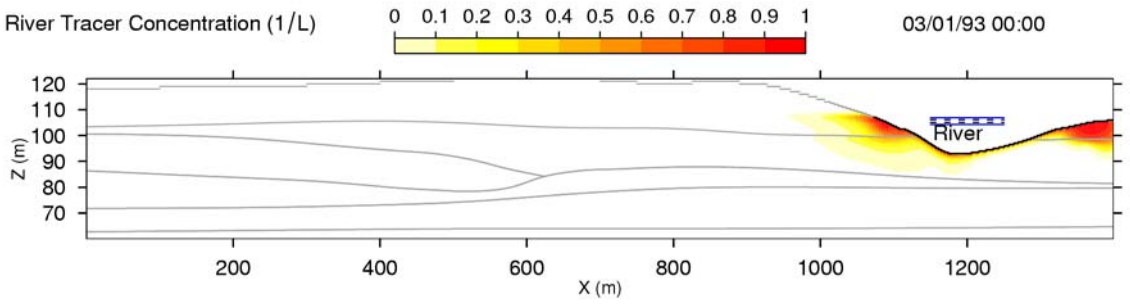

(a)

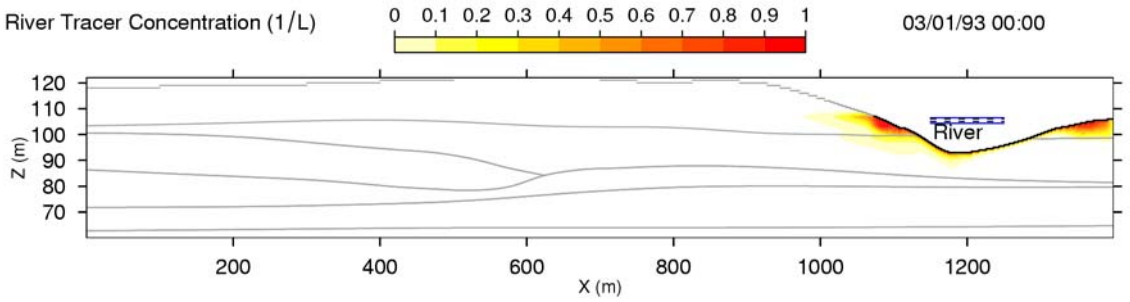

(b)

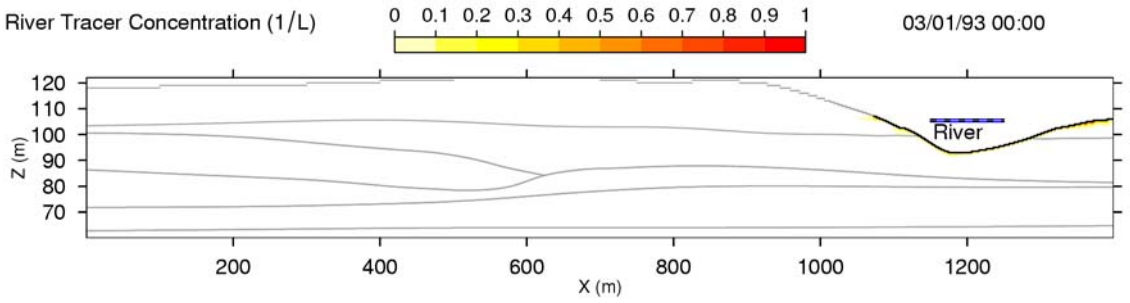

(c)

Figure 2.44. River Water Tracer Concentrations at End of Simulation (March 1, 1993) with (a) Hourly, (b) Daily, and (c) Monthly Boundary Conditions

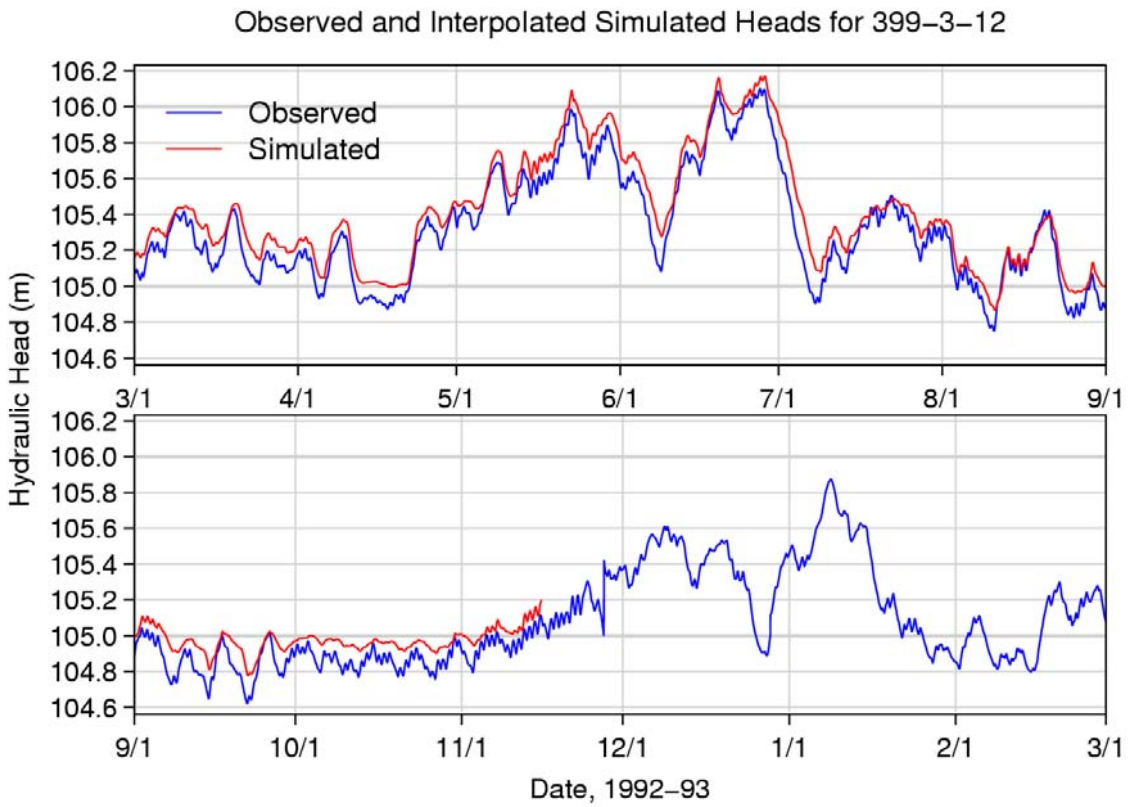

Figure 2.45. Observed Heads at Well 399-3-12 and Interpolated Simulated Heads at the Same Easting Along the Model Cross Section. (The well is located 140 m north of the cross-section line at x = 687 m in the cross section.)

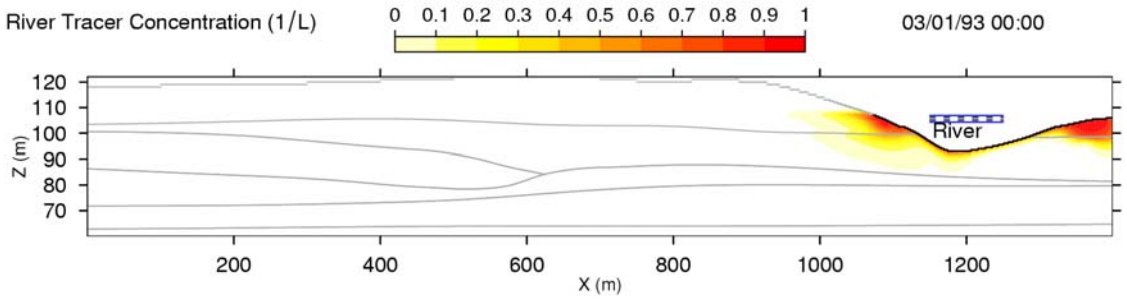

Figure 2.46. Base Case: River Water Mixing Zone in Aquifer After 1 Year of Simulation

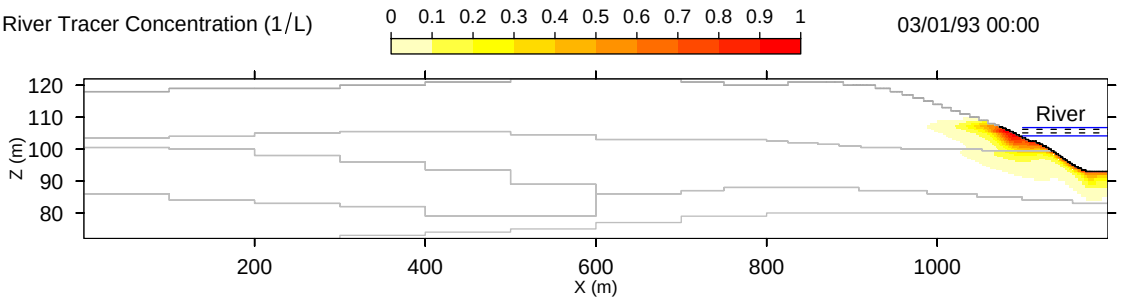

Figure 2.47. Sensitivity Case: River Water Mixing Zone in Aquifer After 1 Year of Simulation with Additional 11.3-cm Drop in River Stage

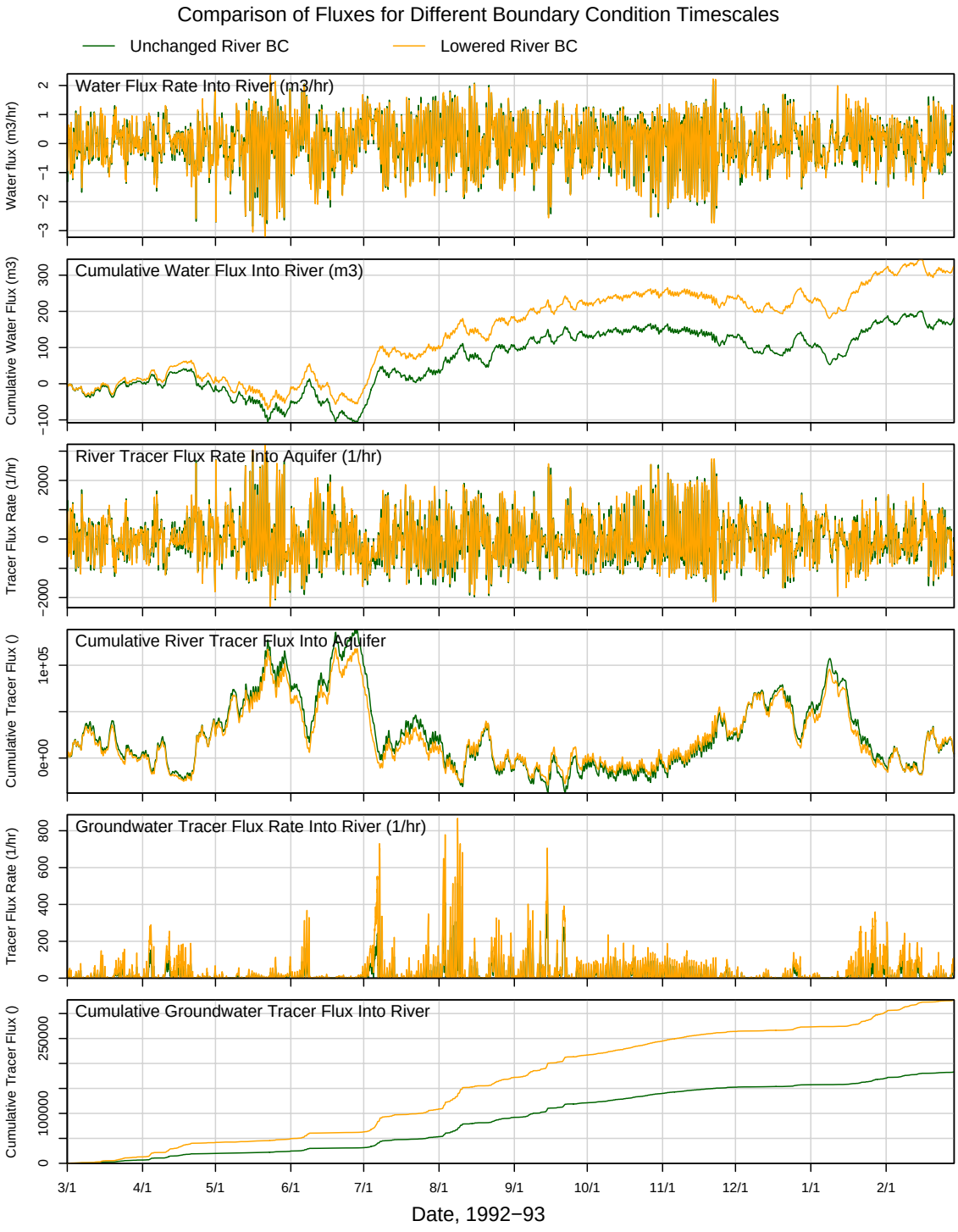

Figure 2.48. Comparison of Water Flux into River for Base Case and Sensitivity Case

Table 2.15. Key Material Properties for STOMP Simulations. (Vertical hydraulic conductivities were 10% of the lateral values.)

Property	Formations	Value
Hydraulic conductivity (lateral) meters/day	U1, Hanford gravel/sand	1,500
	U5, Ringold gravel/sand/silt (C/E)	150
	U6, Ringold overbank mud	0.01
	U7, Ringold gravel/sand/silt (B/D)	43
	U8, Lower Ringold mud and basalt	5×10^{-5}
Porosity	U1	0.25
	U5, U6, U7, U8, basalt	0.18

2.7 Recharge-Driven Uranium Transport in the Vadose Zone

Uranium-contaminated sediments in the 300 Area vadose zone are a potential long-term source of contaminant flux to the underlying groundwater. Considerable effort in the last 10 years has been directed at the excavation and removal of contaminated sediments from the major disposal sites in the 300 Area. Backfilling and re-vegetation of these excavations was completed in spring 2004. However, the experimental K_d of 14 L/kg, derived for the SPP sediments in Section 2.5, can result in aqueous uranium concentrations in excess of the MCL of 30 µg/L with a sediment concentration of as little as 0.43 mg/kg (1.8 nmol/g), which is a background concentration in the 300 Area. This can be compared with the 267 pCi/g (386 mg/kg or 1,620 nmol/g) criteria developed by Callison and Clark (2002) as a threshold for contaminated sediment removal in the 300 Area. This value was arrived at using RESRAD with a K_d = 8.9 L/kg.

While it is clear that near-background levels of uranium in sediments can result in aqueous uranium concentrations in excess of the MCL, a key question is whether recharge-driven transport of uranium in the vadose zone significantly contributes to the uranium concentrations in the groundwater. Screening level one-dimensional modeling analyses based on the equilibrium multi-component uranium surface complexation model in Section 2.4 and the nonequilibrium distributed rate model described in Section 2.5 were performed to assess the magnitude of the vadose zone uranium transport. The principal differences in this modeling approach versus the approach described in Section 2.5 are: (1) flow is unsaturated, (2) flow rates are based on natural recharge rates, and (3) the full sediment sample including all size fractions >2 mm is considered. The screening nature of the calculation is that the field-scale conditions modeled here were not represented in the laboratory experiments.

The vadose zone in the 300 Area varies in thickness from 0 to 15 m and is contained in the Hanford formation. For the purpose of examining the mobility of uranium leached from contaminated sediments in the vadose zone by natural recharge, we specify a vertical, one-dimensional modeling domain with a 1-m thick uranium-contaminated sediment zone emplaced in the center of a 5-m sediment column. Initial sediment concentrations ranged from 30 (7.14 mg/kg) to 3,000 nmol/g (7,140 mg/kg). Uranium-contaminated sediments at the 3,000 nmol/g level are 40% higher than the original 350 pCi/g excavation criteria.

To approximate the field conditions where the larger sediment size fractions dominate the matrix, a full particle size distribution from the NPP-1 4.3 m below ground surface (bgs) sample was used. In this case, the <2-mm-size fraction accounted for 8% of the total weight of the sediment (Table 2.16). Other material properties are based on the Hanford unit sediment characterization in the 300 Area of 0.25 porosity and 2.06 kg/L bulk density, which is representative of historical measurements in the 300 Area (Swanson et al. 1992). Only the <2 mm sediment size fraction (8% by weight of sample) was assumed to provide sorption sites. This was accounted for in the models as the fraction of the bulk density contributing to sorption. A steady recharge rate of 60 mm/yr, based on lysimeter studies in the 300 Area (Gee et al. 2005), was specified for the unsaturated reactive transport model. For the current characterization of the pressure-saturation-relative permeability parameters (Table 2.17) for the Hanford sediments in the 300 Area, natural recharge results in an 8% water content.

Distributed Rate Model. The rate parameters and K_d (Table 2.12) from the slow flow experiments on the SPP sediments were selected because the higher uranium mobility would be a more conservative estimate. Since there is no differentiation of chemical components in this model, there is an implicit assumption that the vadose zone solution chemistry is identical to the artificial groundwater that was used in the calibration experiments.

Multi-Component Surface Complexation Model. This screening reactive transport simulation relies on a preliminary equilibrium multi-component uranium SCM developed at the U.S. Geological Survey earlier this year by Davis et al. (2004). The generalized composite SCM model used here was a preliminary version of the model described in Section 2.4, which is based on a series of batch studies of 300 Area sediments under varying chemical conditions. For the 300 Area sediments, the reactions and calibrated surface constants of interest include one strong site and two weak site reactions:

$$2S(OH)_2 + UO_2^{2+} + 2H_2CO_3 = SO_2UO_2(HCO_3CO_3)^{3-} + 5H^+ \qquad \log K = -16.3$$

$$2W(OH)_2 + UO_2^{2+} + 2H_2CO_3 = WO_2UO_2(HCO_3CO_3)^{3-} + 5H^+ \qquad \log K = -20.6$$

$$2W(OH)_2 + UO_2^{2+} + 2H_2CO_3 = WO_2UO_2(CO_3)^{3-} + 6H^+ \qquad \log K = -28.0$$

The specific surface area of 27.2 m^2/g is used and measured in NPP1-16 bgs (Table 2.8) that is consistent with the sediment for which the SCM calibration was derived. In this case, 8% of the 2.06 kg/L field bulk density was apportioned for surface complexation (i.e., ignoring the >2-mm-size fractions). The total site density of 3.84 $\mu mol/m^2$ is comprised of a strong site density of 1.344 $nmol/m^2$ and a weak site density of 3.839 $\mu mol/m^2$. The reaction network used in conjunction with the SCM includes 46 aqueous uranium complexation reactions as well as major ion reactions including mineral reactions.

Two solution compositions are presented in Table 2.18: (1) groundwater used in a 2003 laboratory experiment, and (2) a 1988 analysis from well 399-8-3, which is situated approximately 500 m west of the 316-5 trenches and not near any contaminated zones. These compositions were used to test the sensitivity of the uranium mobility to solution composition.

2.7.1 Results

Distributed Rate Model. The preliminary results show that under the modeling assumptions of recharge-driven leaching of uranium from unsaturated Hanford unit sediments, the nominal pore water velocity of 0.75 m/yr through the vadose zone is sufficiently slow to minimize the impact of the mass transfer rates in the distributed rate model. The transport of the uranium is much slower than the pore water, on the order of 30 mm/yr (i.e., a retardation factor of 25). At this rate, it will take over 30 years for the contaminant to travel 1 m. In all cases, peak uranium concentrations exceed the MCL of 30 µg/L (0.126 µmol/L) and travel at the retarded pore velocity. This is because the model does not account for variations in uranium concentrations (or solution chemistry), essentially behaving as a function of K_d, bulk density, and water content, which are all constant. Peak aqueous concentrations for the case of 30 nmol/g (7.14 mg/kg) of initial uranium on the sediments (Figure 2.49) are about 2 µmol, and about 200 µmol for the 3,000 nmol/g (7,140 mg/kg) (Figure 2.50) case.

Multi-Component Surface Complexation Model. Simulations with the equilibrium multi-component SCM showed that the water chemistry from well 399-8-3 resulted in uranium mobility very similar to the DRM: very slow migration requiring over 30 years to move 1 m (Figure 2.51). This is because the intrinsic K_d for this system was about 12.4 L/kg, which is similar to the 14 L/kg in the DRM specification. The laboratory groundwater composition with elevated calcium yielded an order of magnitude higher uranium mobility (Figure 2.52). The intrinsic K_d in this case was 0.84, more than an order of magnitude lower than that from the well composition. The reduction in sorption results in significant uranium leaching from contaminated sediments. Uranium in this case migrates with a retardation factor of only 4.

Contribution of Uranium-Contaminated Vadose Zone Sediments to Groundwater. While uranium transport is significantly retarded in uncontaminated vadose zone sediments, aqueous uranium in equilibrium with contaminated sediments can migrate with the ambient pore water. For the case where the vadose zone sediments are contaminated with uranium down to water table, as occurs immediately below the two process ponds, the aqueous uranium concentration at the bottom of the vadose zone discharges into the aquifer with the flux of water from the vadose zone. At that point, the aqueous uranium concentration resulting from the mixing of the vadose zone pore water with the groundwater (ignoring sorption) would be dependent on (1) the flux ratio of groundwater flow to recharge and (2) the aqueous concentrations in the groundwater and the vadose zone waters. Future transport simulations will address this particular scenario in more detail.

2.7.2 Synopsis and Implications

The synopsis of findings from studies of recharge-driven uranium transport and their implications are as follows:

- These screening reactive transport simulations are based on models derived under saturated conditions in the laboratory with <2-mm-size sediments that have been adapted to represent the unsaturated field system. Assumptions include the applicability to unsaturated systems and the "dilution" of the reactive surfaces by sediments >2 mm.

- The time scales of recharge-driven transport are sufficiently long to remove most of the kinetic rate effects and approximate an equilibrium sorption model for uranium adsorption by uncontaminated sediment. Under this condition, the DRM essentially behaves as a linear equilibrium isotherm with K_d of 14 L/kg. The equilibrium SCM appears to be consistent with the time scales of recharge-driven transport in the vadose zone. In this case, uranium mobility can be nearly identical to the DRM result or much higher when the calcium concentrations (in the laboratory composition) are significantly higher.

- Based on the tested range of sediment contamination levels observed in the 300 Area, predicted peak aqueous uranium concentrations in the vadose zone will exceed the MCL.

- Assuming natural recharge of 60 mm/yr, the retarded uranium travel rate in uncontaminated sediments would be on the order of 30 mm/yr, which would delay the arrival of vadose zone uranium for several decades. The uranium mass flux to the water table under this scenario would be slow enough to minimize impact to uranium groundwater concentrations.

- Elevated calcium in the "laboratory" groundwater composition resulted in enhanced uranium mobility on the order of 0.25 m/yr, which, depending on distance above the water table, may still result in transport time scales on the order of decades.

- Once the retarded uranium front reaches the water table, as occurred beneath NPP and SPP, the aqueous concentration at the bottom of the vadose zone can move into the aquifer with natural recharge (i.e., unretarded). However, the contribution of natural recharge is relatively small compared to the net groundwater flow to the river, which would tend to reduce the impact of contaminated vadose zone pore water on the groundwater. This effect can be offset to some degree by much higher aqueous vadose zone concentrations and/or widespread contamination of the vadose zone.

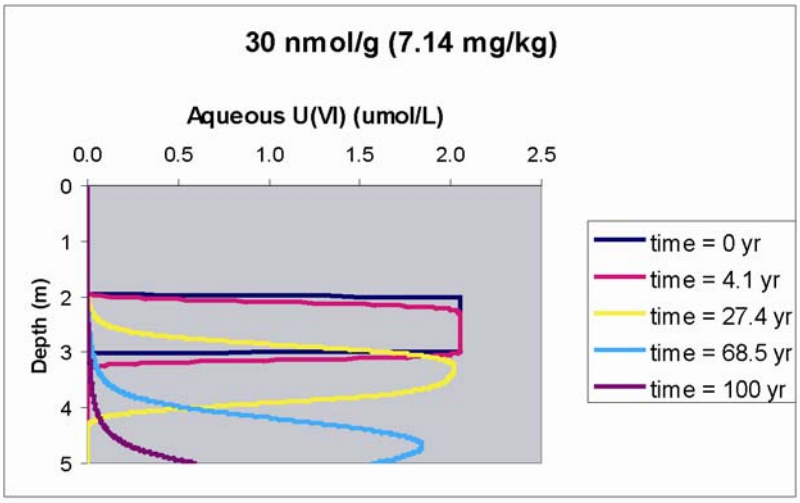

Figure 2.49. Recharge-Driven Transport of Uranium Leached from 30 nmol/g (7.14 mg/kg) Contaminated Vadose Zone Sediments. (Curves represent the spatial distribution with depth at 4.1, 27.4, 68.5, and 100 years.)

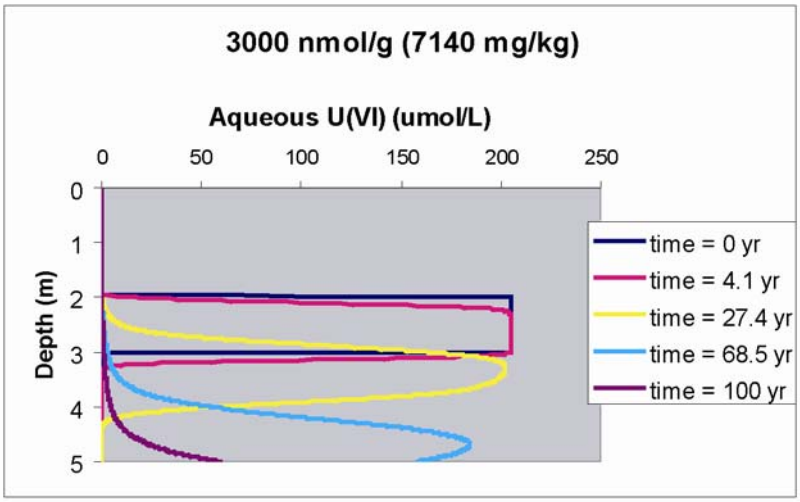

Figure 2.50. Recharge-Driven Transport of Uranium Leached from 3,000 nmol/g (7,140 mg/kg) Contaminated Vadose Zone Sediments. (Curves represent the spatial distribution with depth at 4.1, 27.4, 68.5, and 100 years.)

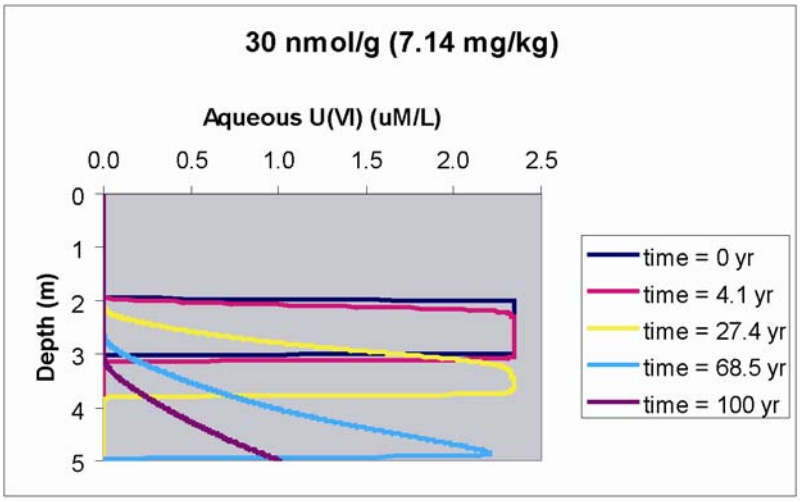

Figure 2.51. Recharge-Driven Transport of Uranium Leached from 30 nmol/g (7.14 mg/kg) Contaminated Vadose Zone Sediments Under Groundwater Chemistry from Well 399-8-3. (Curves represent the spatial distribution with depth at 4.1, 27.4, 68.5, and 100 years.)

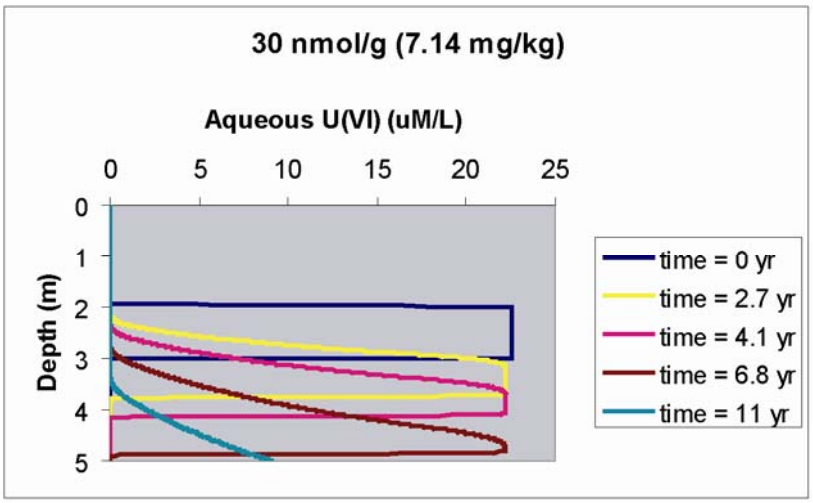

Figure 2.52. Recharge-Driven Transport of Uranium Leached from 30 nmol/g (7.14 mg/kg) Contaminated Vadose Zone Sediments Under Groundwater Chemistry from Laboratory Composition. (Curves represent the spatial distribution with depth at 4.1, 6.8, and 11 years.)

Table 2.16. Sediment Size Distribution for NPP-1, 4.3 m Below Ground Surface

Size (mm)	Mass Distribution (%)
Cobbles	
>12.5	74.5
2.0-12.5	17.2
Sand	
1.0-2.0	2.64
0.5-1.0	2.34
0.25-0.5	0.78
0.149-0.25	0.33
0.106-0.149	0.19
0.053-0.106	0.20
Silt + Clay	
<0.053	1.78

Table 2.17. Unsaturated Flow Parameters for Hanford Unit Sediments

Unsaturated Flow Model Parameters	Value	Units
Horizontal hydraulic conductivity	1,500	m/d
Vertical hydraulic conductivity	150	m/d
Air entry pressure	23.04	cm
Brooks-Corey λ	0.7465	
Residual saturation	0.1471	
Relative permeability method	Burdine	
Porosity	0.25	
Bulk density	2.06	kg/L
Recharge rate	60	mm/yr
Calculated water content	0.08	

Table 2.18. Solution Compositions Tested in the Multi-Component Surface Complexation Model

Components	2003 Experiment (mol/L)	1988 399-8-3 (mol/L)
pH	7.19	7.7
HCO_3^-	1.81×10^{-3}	2.66×10^{-3}
K^+	1.28×10^{-4}	1.50×10^{-4}
NO_3^-	0	1.73×10^{-4}
Na^+	7.85×10^{-5}	9.87×10^{-4}
Ca^{++}	6.61×10^{-3}	1.10×10^{-3}
Mg^{++}	1.83×10^{-3}	4.10×10^{-4}
Cl^-	2.75×10^{-3}	2.75×10^{-3}
SO_4^{--}	2.64×10^{-3}	3.25×10^{-4}

2.8 Solution Chemistry Effects on Saturated Uranium Reactive Transport

The migration of uranium through the 300 Area aquifer to the Columbia River is complicated by variable solution chemistry caused by the mixing of dilute river water with higher ionic strength groundwater. Two-dimensional modeling of the aquifer-river system in Section 2.6 suggests that the influence of river water exists about 100 m from the river and increases nearer the river. In this section, simulations describing the impact of aquifer versus river water chemistry on the mobility of uranium are described. The multi-component uranium surface complexation was implemented for this modeling effort. One-dimensional reactive transport simulations of a 0.5-m sediment section with an initial uranium concentration of 30 nmol/g (7.14 mg/kg), were used to examine how the partitioning of uranium initially in equilibrium with river water and sediments is significantly altered by the incursion of aquifer water. This would be the situation near the river during fluctuations of river stage.

To approximate the field conditions where the larger sediment size fractions dominate the matrix, a full particle size distribution from the NPP-1 4.3 m bgs sample was used. In this case, the <2-mm-size fraction accounted for 8% of the total weight of the sediment (Table 2.19). Other material properties were based on the Hanford formation sediment characterization in the 300 Area of 0.25 porosity and 2.06 kg/L bulk density, which is representative of historical measurements in the 300 Area (Swanson et al. 1992). Only the <2-mm-size sediment fraction (8% by weight of sample) was assumed to provide sorption sites. This was accounted for in the models as the fraction of the bulk density contributing to sorption.

The generalized composite SCM model used here was a preliminary version of the model described in Section 2.4, which is based on a series of batch studies of 300 Area sediments under varying chemical conditions. For the 300 Area sediments, the reactions and calibrated surface constants of interest include one strong site and two weak site reactions:

$$2S(OH)_2 + UO_2^{2+} + 2H_2CO_3 = SO_2UO_2(HCO_3CO_3)^{3-} + 5H^+ \qquad \log K = -16.3$$

$$2W(OH)_2 + UO_2^{2+} + 2H_2CO_3 = WO_2UO_2(HCO_3CO_3)^{3-} + 5H^+ \qquad \log K = -20.6$$

$$2W(OH)_2 + UO_2^{2+} + 2H_2CO_3 = WO_2UO_2(CO_3)^{-3-} + 6H^+ \qquad \log K = -28.0$$

The specific surface area of 27.2 m^2/g measured in NPP1-16 bgs (Table 2.8) was used, consistent with the sediment for which the SCM calibration was derived. In this case, 8% of the 2.06 kg/L field bulk density was apportioned for surface complexation (i.e., ignoring the >2-mm-size fractions). The total site density of 3.84 μmol/m^2 is comprised of a strong site density of 1.34 nmol/m^2 and a weak site density of 3.839 μmol/m^2. The reaction network used in conjunction with the SCM includes 46 aqueous uranium complexation reactions as well as major ion reactions including mineral reactions.

The SCM is adapted for the situation near the river where the solution chemistry in the aquifer alternates between the dilute river water and the higher ionic strength groundwater. The two-dimensional vertical cross-section modeling in Section 2.6 indicates that the diurnal river stage fluctuations result in a quasi-steady state mixing zone within 100 m of the river.

The reactive transport modeling investigated two solutions for the groundwater chemistry in addition to the river water chemistry. The compositions of these solutions are shown in Table 2.20. Each simulation was initialized with 30 nmol/g (7.14 mg/kg) of uranium on the sediments and brought into equilibrium with the river water chemistry. The resulting initial aqueous uranium condition is 5.76 x 10^{-8} mol/L. In case 1, the laboratory groundwater composition was used to leach the uranium from the contaminated sediments. In case 2, well 399-8-3 groundwater composition was used for the leaching.

2.8.1 Results

In the simulation with a 1.4 m/day Darcy flux (average in Hanford unit from two-dimensional flow model), influent groundwater resulted in an increase in the aqueous uranium concentrations from the initial uranium concentration of 5.76 x 10^{-8} mol/L to 2.5 x 10^{-6} mol/L (Figure 2.53) when using well 399-8-3 groundwater and to variable peaks of 1.5 x 10^{-5} to 4.0 x 10^{-5} mol/L (Figure 2.54) when using the laboratory groundwater composition. The laboratory composition was lower in pH and bicarbonate but higher in calcium and magnesium. The implication is that uranium is being complexed and made less available for adsorption. In fact, the laboratory groundwater extracted most of the uranium from the sediments as it moved with the flow. Conversely, well 399-8-3 groundwater resulted in an equilibrium aqueous uranium concentration of 2.5 x 10^{-6} mol/L that was maintained until the sediments are depleted. In this case, there was a general retardation factor of 6 in uranium migration. If the incursion of aquifer water were continuous, a depleted uranium front would move slowly through system.

Although not pictured here, when river water enters a zone where uranium has equilibrated with aquifer water chemistry, the opposite is true with aqueous uranium concentrations decreasing by two to three orders of magnitude, depending on solution composition. The SCM includes only equilibrium reactions, which is reflected in the rapid response of the system to changing aqueous concentrations.

Figure 2.55 represents a sequence of 4 days of uranium loading onto uncontaminated sediments in conjunction with a river water composition, followed by a "leaching" stage of uncontaminated well 399-8-3 groundwater. The sequence demonstrates how rapidly the aqueous uranium concentrations respond to loading and unloading cycles under the equilibrium assumption.

2.8.2 Synopsis and Implications

The synopsis of findings from studies of solution chemistry effects and the implications for saturated uranium reactive transport are as follows:

- For well 399-8-3 groundwater, the intrinsic (<2 mm) K_d value for the river water in contact with 30 nmol/g uranium on the sediments was over 500 L/kg and resulted in an aqueous uranium concentration of 5.76 x 10^{-8} mol/L. Conversely, the intrinsic K_d value for the higher ionic strength groundwater in contact with the 30 nmol/g (7.14 mg/kg) uranium on the sediments was 13.5 L/kg, which resulted in an aqueous uranium concentration of 1.87 x 10^{-6} mol/L. Thus, the endpoint aqueous uranium concentrations were two orders of magnitude different.

- The assumption that only the <2 mm sediments provide sorption sites and only 8% of the Hanford unit sediments are <2 mm, resulted in more than an order of magnitude reduction in the apparent K_d values, all other factors (pH, $pCO_{2(g)}$, U) being equal.

- The one-dimensional modeling study showed that uranium that is leached off contaminated sediments is comparatively mobile in the higher ionic strength groundwater. As this uranium came into contact with uncontaminated sediments, uranium partitioned onto surface sites, retarding travel. Aqueous uranium that comes into contact with groundwater diluted by river water experienced enhanced sorption with as much as 99% of the aqueous uranium partitioned to the solid phases. Under these conditions, uranium accumulated on these surfaces associated with the solid phases. The accumulated sorbed uranium can significantly desorb when higher ionic strength groundwater comes into contact with these contaminated sediments.

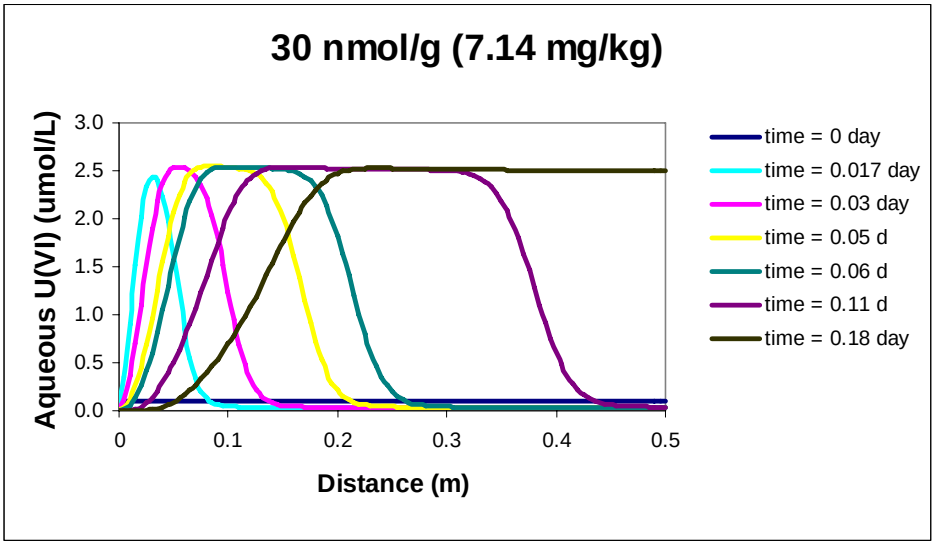

Figure 2.53. Uranium Leached from 30 nmol/g (7.14 mg/kg) Contaminated Sediments by Groundwater from Well 399-8-3. (Curves represent the spatial distribution with distance at 0.017, 0.03, 0.05, 0.06, 0.11, and 0.18 days. Residence time is 0.14 days.)

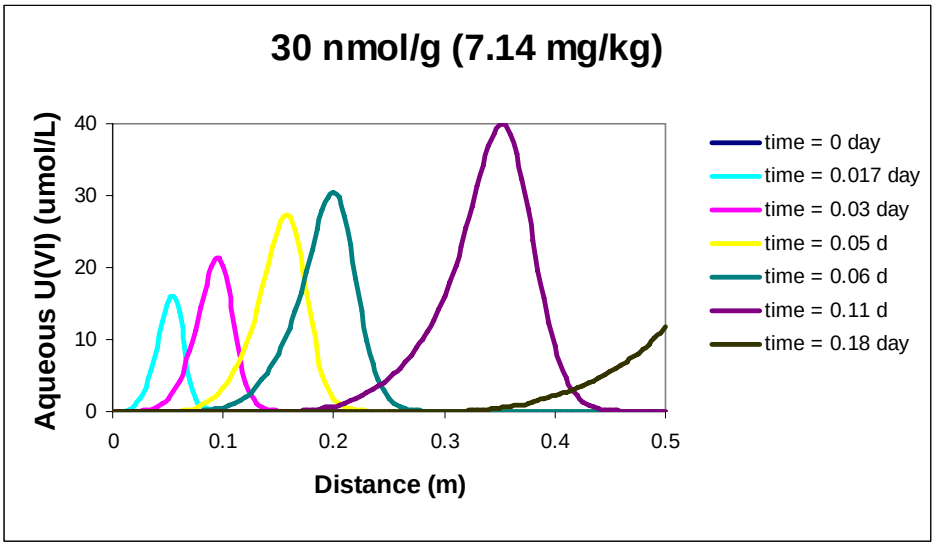

Figure 2.54. Uranium Leached from 30 nmol/g (7.14 mg/kg) Contaminated Sediments by Laboratory Composition Artificial Groundwater. (Curves represent the spatial distribution with distance at 0.017, 0.03, 0.05, 0.06, 0.11, and 0.18 days. Residence time is 0.14 day.)

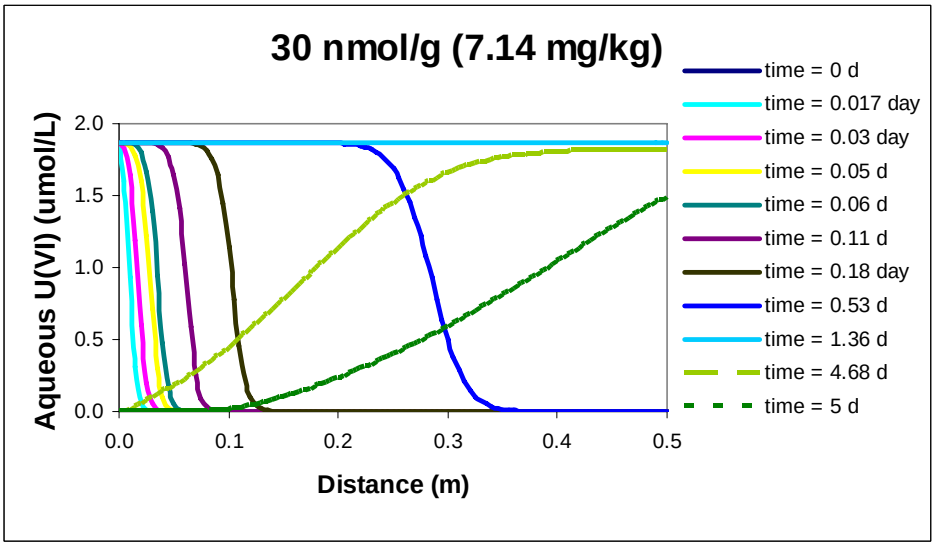

Figure 2.55. Sequence of 4 Days Loading and 1 Day Unloading of Sites Using Groundwater Composition from Well 399-8-3

Table 2.19. Sediment Size Distribution for NPP-1, 4.3 m Below Ground Surface (Smith and Zachara 2004)

Size (mm)	Mass Distribution (%)
Cobbles	
>12.5	74.5
2.0-12.5	17.2
Sand	
1.0-2.0	2.64
0.5-1.0	2.34
0.25-0.5	0.78
0.149-0.25	0.33
0.106-0.149	0.19
0.053-0.106	0.20
Silt + Clay	
<0.053	1.78

Table 2.20. Water Composition for the River, Groundwater, and Laboratory Solution

Components	River Water (USGS 6/1/2000)	1988 Well 399-8-3	2003 Lab Analysis
pH	7.1	7.7	7.19
HCO_3^- (mol/L)	9.18×10^{-4}	2.66×10^{-3}	1.81×10^{-3}
K^+ (mol/L)	1.75×10^{-5}	1.50×10^{-4}	1.28×10^{-4}
NO_3^- (mol/L)	8.55×10^{-6}	1.72×10^{-4}	0
Sr^{++} (mol/L)	1.23×10^{-6}	0	1.12×10^{-5}
Na^+ (mol/L)	1.00×10^{-4}	9.87×10^{-4}	1.10×10^{-3}
Ca^{++} (mol/L)	3.74×10^{-4}	1.10×10^{-3}	6.61×10^{-3}
Mg^{++} (mol/L)	1.48×10^{-4}	4.1×10^{-4}	1.83×10^{-3}
Cl^- (mol/L)	3.10×10^{-5}	2.75×10^{-3}	2.75×10^{-3}
SO_4^{--} (mol/L)	7.08×10^{-5}	3.25×10^{-4}	2.64×10^{-3}

3.0 An Integrated Conceptual Model

Major objectives of the research described in the preceding sections have been to: (1) develop an improved geohydrochemical conceptual model of the linked uranium-contaminated vadose zone and aquifer system in the 300 Area, and (2) develop and parameterize a reactive transport simulator that captures key aspects of the conceptual model for improved predictions of uranium plume behavior in 300 Area groundwater. While the studies are still ongoing, a first phase of research was completed to support the 5-year review of the 300-FF-5 interim record of decision (ROD 1996) and update of the conceptual model and work plan recently published (DOE 2005). Research has progressed to the point where a preliminary, but defensible integrated conceptual model can be proposed. This model is described in the following paragraphs. More detailed versions of the studies and additional data are being submitted to peer reviewed journals and should be consulted as well.

The 300 Area process ponds (NPP and SPP) received waste between 1943 and 1975, while trench 316-5 was used from 1975 to 1985. A complex, poorly documented series of waste streams were disposed to these locations including process waste from nuclear fuel fabrication (the primary waste stream), radioactive liquid waste, sewage, lab waste, and coal power waste. The waste from nuclear fuel fabrication included basic sodium aluminate solutions and acidic copper/uranyl nitrate solutions. Primary chemical contaminants disposed to NPP and SPP included uranium (33,565 to 58,967 kg), copper (241,311 kg), fluoride (117,026 kg), aluminum (113,398 kg) nitrate (2,060,670 kg), and large volumes of acid (HNO_3) and base (NaOH).

The initially acid conditions of the copper/uranyl nitrate waste allowed migration of copper and uranium through both the vadose zone and aquifer system to the Columbia River. Limited records document that the pH of the 300 Area process pond water varied over large range during operation (pH 1 to 12) as a result of the nature of the waste and intentional manipulation by site personnel. Anecdotal remarks (Dennison et al. 1989; DOE 1990) indicate that base (e.g., NaOH) was added to the pond water to neutralize acid and limit the migration of copper to the river that was evident as green-staining around shoreline seeps. Divalent copper (Cu^{2+}) and U(VI) (UO_2^{2+}) exhibit comparable and high mobility under acidic conditions. Both these ions adsorb strongly to mineral matter (iron, aluminum, and manganese oxides, and layer silicates) at circumneutral pH and are prone to precipitation as hydroxide, carbonate, and other mineral phases as pH is increased. Neutralization of the pond waters decreased migration of copper and uranium through a combination of near-field precipitation and far-field adsorption process in both the vadose zone and aquifer sediments.

The subsurface mobility of uranyl, in strong contrast to Cu^{2+}, increases above pH 8 through formation of anionic uranyl carbonate [$UO_2(CO_3)_3^{2-}$] and weakly-sorbing calcium uranyl carbonate [$Ca\ UO_2(CO_3)_3$] aqueous complexes. Over neutralization of the pond waste encouraged the formation of these more mobile uranium species that permeated the groundwater system for extended operational periods. In groundwater, a significant fraction of the dissolved uranium adsorbed to fine-grained materials (layer lattice silicates primarily with very minor Fe(III) oxide content) in the aquifer sediments. Long periods of elevated groundwater uranium concentrations promoted diffusion of uranium to sorption and precipitation sites in distal intragrain/intraaggregate microfractures and pores.

These residual sorbed (adsorbed and precipitated) uranium and copper phases still exist in the sediments and groundwater fines that were sampled and investigated in this research. Much of the Remediation and Closure Science Project research has sought to identify the precise nature of the sorbed uranium phases and to quantify the uranium concentrations released by these materials and their rate of supply to pore or groundwater. The research objective has been to understand the implications of contaminant uranium desorption or dissolution from these phases to the future, long-term geochemical behavior of uranium in both the vadose zone and aquifer system.

Over neutralization of the waste ponds in their later years of operation left a mineralogical legacy of high calcite content in the near surface sediments (NP 4-1 and 4-2) that was excavated as part of source term removal. The Remediation and Closure Science Project received samples of these near-surface materials that were retrieved over ten years ago. Some of these pond sediments contained as much as 35% calcite. Calcite super saturation and precipitation occurred in basic waste solutions and pore water through absorption of atmospheric $CO_{2(g)}$ and mass-action displacement of Ca^{2+} by Na^{+} from the layer-lattice silicate dominated, sediment ion exchange complex. Thin veneers of calcium carbonate indurated grain coatings were observed on upper vadose zone sediments collected beneath NPP and SPP by microscopic analyses of sediment thin sections (e.g., Section 2.2). The extent, and possibly the rate, of calcite precipitation decreased with depth below the pond interface as sediment-water reaction reduced the extent of calcite super saturation by pH neutralization (silicate mineral dissolution) and carbonate precipitation. Our analyses documented that calcite concentrations decrease with depth below the disposal ponds and are near detection (<0.1 mass percent) in the deeper vadose zone materials and capillary fringe. However acidified ammonium acetate extractions show that calcite is still present, albeit at low concentration, in the capillary fringe sediment.

X-ray absorption spectroscopic (XAS) measurements (Section 2.2) indicated that most, if not all sorbed uranium in the 300 Area sediments is hexavalent and present as the uranyl cation (UO_2^{2+}) in complexed, precipitated, and adsorbed forms. Precipitation of uranium was most evident in "historic" shallow pond sediments where high levels of sediment associated uranium were found (e.g., all of the NP series sediments with total uranium >1,000 mg/kg). Precipitated uranium was also present in select, post-excavation sediments from pit #2 in the NPP whose total uranium concentration (in the <2.0 millimeter fraction) exceeded 100 mg/kg (e.g., NPP2-0.5 and NPP2-4). These sediments invariably displayed greenish hue from precipitated, co-contaminant copper. Sediments with concentrations between 50 and 100 mg/kg uranium (e.g., NPP2-2) may also have precipitated uranium, but supporting spectroscopic evidence is ambiguous. Microscopic evaluations of the contaminated sediments typically showed contaminant copper and uranium in close spatial association. In certain locations copper and uranium were coincident at the micron to submicron scale, while in others they were closely associated, but separate.

Spectroscopic measurements (EXAFS, CLIFS, and synchrotron diffraction) indicated that precipitated uranium exists primarily as a minor substitute in aragonitic calcite in the shallow pond sediments (NP 4-1 and 4-2). The formation of aragonitic calcite in the pond floor sediments was promoted by the high salt and soluble magnesium and phosphate content of the wastes. Precipitated uranium in the shallow depths of the post excavation sediments (e.g., NPP2-0.5 and NPP2-4) appears to exist as a minor substituent in calcite and as a copper uranium phosphate (metatorbernite). Malachite $[Cu_2(CO_3)(OH)_2]$ was the primary copper phase identified in the sediments by synchrotron x-ray

diffraction. These phase identifications are considered preliminary at this point and subject to change with further analyses. Definitive measurements of this sort are difficult to make because of the small size of the precipitates and mineralogical heterogeneity of the sediments.

The geochemical nature of adsorbed U(VI) in sediments containing <50 mg/kg total uranium has not yet been precisely identified, but remains a subject of ongoing spectroscopic and geochemical study. Almost all of the adsorbed U(VI) exists in the silt and clay-sized (fines) fraction which is present at small mass percent (e.g., ≈1.5-2.0%) in the whole sediment (Table 2.1). The fines fraction is comprised of the phyllosilicates chlorite, vermiculite/illite, and beidellite. It is presumed that adsorption occurs through the surface complexation of aqueous uranyl carbonate complexes to their hydroxylated edges. However, the significantly higher sorptivity noted for sediments from the NPP as compared to the SPP (Sections 2.4 and 2.5) appeared to result from the higher extractable (AAO) Fe(III) oxide content of the former sediments. The poorly crystalline Fe(III) oxides removed by AAO are known to be strong U(VI) adsorbents, and their presence likely results from the oxidative weathering of fine-grained chlorite in the silt and clay fractions. This type of weathering is expected to be greater in the aquifer sediments. Electron microscopy has shown that the poorly crystalline Fe(III) oxides exist as small, widely dispersed aggregates of nanometer-sized precipitates adhering to chlorite surfaces. The uranium sorptivity of the <2.0 mm fraction of both the SPP and NPP sediments was found to vary directly with the bicarbonate concentration of the contacting electrolyte.

The degree of uranium sorption to the 300 Area materials was high as compared to other Hanford sediments. Adsorption distribution coefficients (K_d values) for the <2.0 mm sediments ranged from approximately 5 to 100 L/kg (in batch experiments) at the approximate bicarbonate concentration of the groundwater. Even higher values (e.g., 310 L/kg) were observed in the column experiment with <2.0 mm NPP1-16 sediment washed free of contaminant uranium. The K_d range for the whole sediment with its high cobble content was estimated to be 1 to 24 L/kg, (based only on batch experiment results). This range will be further substantiated by ongoing experiments and modeling. It is important to recognize that K_d values must be carefully formulated to account for the effects of sorbed contaminant uranium which is significant. The magnitude of K_d observed in our studies of 300 Area sediments significantly exceeds those used in earlier modeling of the 300 Area plume.

A SCM model was developed to account for the effect of pH, bicarbonate concentration, $CO_{2(g)}$ partial pressure, and aqueous uranium speciation on uranium adsorption to sediments from the NPP and SPP. These factors, along with mineral composition and sediment texture, are the primary ones causing large variability in the U(VI)-K_d for 300 Area sediments. The SCM allows estimation of K_d as a function of these variables, or it may be used directly in a reaction-based solute transport model such as STOMP. The SCM predicts that U(VI)-K_d values will increase markedly (e.g., by 10 to 100 times) when low bicarbonate-containing river water contacts uranyl containing aquifer sediments. Thus, the infusion of river water into the U(VI)-containing aquifer during times of high flow will not hasten the dissipation of the existing U(VI) plume. In contrast, it will act to stabilize it, and to concentrate adsorbed uranium in near-river aquifer sediments.

Both precipitated and adsorbed uranium was released from the sediments more slowly then expected. The precise cause for the slow kinetic release appears twofold. First, a significant fraction of sorbed uranium in the higher concentration sediments exists as a co-precipitate with calcite or copper that indurates fine-grained aluminosilicate precipitates. Solid carbonates dissolve slowly in 300 Area vadose zone and groundwater because their composition is at or near thermodynamic saturation with calcite. Dissolution of U(VI) from copper-containing precipitates is likewise regulated by the solubility of Cu^{2+} that is significantly lower than uranium under the current pH conditions of the 300 Area vadose zone. Secondly, U(VI) adsorption appears to occur in phyllosilicate aggregates of waste and detrital origin that contain variable concentrations of poorly crystalline Fe(III) oxides. Entrance and exit from the aggregates is diffusion controlled, and the slow sorption/desorption rates observed suggest that the intra-aggregate porosity is highly tortuous. Many, many pore volumes of fluids were required (e.g., >100) to leach the labile uranium fraction from sediments at all depth levels. The extent of desorption/dissolution was lower under unsaturated conditions because of pore bypass and other factors, but aqueous concentrations in the unsaturated leachates tended to peak at higher levels when moisture contents were low.

The desorption/dissolution of sorbed uranium was controlled by bicarbonate concentration in the leaching fluid and the contact time. Longer contact times allowed the kinetically slow release process to progress closer to equilibrium. Increasing bicarbonate stabilized U(VI) as carbonate complexes in the aqueous phase. All materials studied, ranging from the lowest (<5 mg/kg) to the highest total uranium concentration (3,000 mg/kg) sediments desorbed U(VI) to concentrations in excess of the MCL when contact times and bicarbonate concentration were used that approximate in situ conditions. However the maximum effluent U(VI) concentration observed in experiments performed to date with deep vadose zone materials (e.g., those currently remaining in the field) was 0.4 μmol/L (95.2 ppb). The geochemical reaction controlling this concentration has not yet been identified.

All of the experimental work and associated modeling described in this report were performed with the <2.0 mm sediment fraction. While these materials are the most reactive sediment components, they represent only a small fraction (approximately 8.3%) of the total sediment mass. Over 74.5% of the sampled sediment was rounded, surface smooth, river cobble that was >12.5 mm in size. The <2.0 mm materials studied exist as infilling between the large cobbles, but their in-situ structure, porosity, and other physical attributes were not characterized. They may, in fact, exhibit complex physical character that exerts a significant influence on uranium reactive transport, in particular the kinetically controlled reactions. Consequently, appropriate use of the experimental data and model parameters developed by this research for field scale predictions requires the scaling of this information to in-situ textural and structural conditions. Strong kinetic behavior for uranium dissolution, desorption, and adsorption has been observed in laboratory studies of <2.0 mm sediment materials, and it is assumed that such behavior will occur in the field. However, the relative importance of sorption/desorption kinetics in the vadose zone and groundwater system needs to be assessed with scaling and explicit consideration of pore water velocities in both the saturated and unsaturated zones. Reaction parameter scaling has not yet been performed, but is planned as part of associated Environmental Management Science Program research.

In summary, the scientific studies described in this report have made important additions to a conceptual geohydrochemical model for the 300 Area uranium plume. The following are important conclusions and implications:

1. Residual U(VI) concentrations observed beneath SPP and NPP are heterogeneous and display no marked trend with depth. An average of 37.5% of the residual, sorbed uranium appears accessible to dissolution/desorption, but variation in this number between sediments is large. Dissolution/desorption extent was found to decrease with decreasing water content and at 21% water saturation was only 1-3% of total uranium.

2. Both precipitated and adsorbed U(VI) exists in the sediments. A precise demarcation of precipitated and adsorbed forms, and their relative concentrations is difficult. Adsorbed U(VI) predominates in sediments with total uranium <25 mg/kg.

3. The vadose zone sediments beneath both SPP and NPP will remain as potential source terms to maintain groundwater U(VI) concentrations at or above the MCL. Their ultimate impact will be controlled by moisture flux rates through the vadose zone and their bicarbonate concentrations. Increasing groundwater levels at high river stage will solubilize sorbed U(VI) from the capillary fringe and lower vadose zone.

4. Adsorption extent decreases with increasing aqueous bicarbonate concentration. U(VI) is adsorbed by 300 Area vadose zone and aquifer sediments more strongly than previously recognized. Travel times for adsorption and desorption fronts through the aquifer will consequently be longer by factors of 2 to 5, or even more.

5. The intrusion of river water into the aquifer during periods of high river stage increases the adsorption of U(VI) to aquifer solids in regions of the saturated zone where groundwater composition is controlled by river water quality. These intrusion events slow the dissipation of the U(VI) groundwater plume and reduce discharge concentrations to the Columbia River.

6. The vadose zone and aquifer sediments beneath the SPP and NPP differ significantly in sorption properties for uranium. A single value of K_d is therefore unlikely to yield realistic simulations of U(VI) geochemical behavior in the 300 Area plume given heterogeneity in sediment properties and the apparent importance of kinetic processes. Reactive transport modeling of the future dynamics of the plume will consider these issues.

7. The dissolution of U(VI) containing solids and the desorption of U(VI) surface complexes in the contaminated sediments are slow. Equilibrium-based models don't capture the slow release and have led to shorter predictions of the time required for plume dissipation to the MCL.

4.0 References

Arnold T, T Zorn, H Zanker, G Bernhard, and H Nitsche. 2001. "Sorption Behavior of U(VI) on Phyllite: Experiments and Modeling." *J. Contam. Hydrol. 47*, 219-231.

Baik MH, WJ Cho, and PS Han. 2004. "Sorption of U(VI) onto Granite Surfaces: A Kinetic Approach." *J. Radionanal. Nucl. Chem.* 260:495-502.

Bargar JR, R Reitmeyer, and JA Davis. 1999. "Spectroscopic Confirmation of Uranium(VI)-Carbonate Adsorption Complexes on Hematite." *Environ. Sci. Technol.* 33:2481-2484.

Bargar JR, R Reitmeyer, JJ Lenhart, and JA Davis. 2000. "Characterization of U(VI)-Carbonate Ternary Complexes on Hematite: EXAFS and Electrophoretic Mobility Measurements." *Geochim. Cosmochim. Acta* 64:2737-2749.

Barnett MO, PM Jardine, and SC Brooks. 2002. "U(VI) Adsorption to Heterogeneous Subsurface Media: Application of a Surface Complexation Model." *Environ. Sci. Technol. 36*:937-942.

Barnett MO, PM Jardine, SC Brooks, and HM Selim. 2000. "Adsorption and Transport of Uranium(VI) in Subsurface Media." *Soil Sci. Soc. Am. J.* 64:908-917.

Bernhard G, G Geipel, T Reich, V Brendler, S Amayri, and H Nitsche. 2001. "Uranyl(VI) Carbonate Complex Formation: Validation of the $Ca_2UO_2(CO_3)_3$ (aq.) Species." *Radiochim. Acta* 89:511-518.

Bethke CM, and PV Brady. 2000. "How the K_d Approach Undermines Groundwater Cleanup." *Ground Water 38*:435-443.

Braithwaite A, FR Livens, S Richardson, MT Howe, and KWT Goulding. 1997. "Kinetically Controlled Release of Uranium from Soils." *Eur. J. Soil Sci*. 48:661-673.

Braithwaite A, S Richardson, LN Moyes, FR Livens, DJ Bunker, and CR Hughes. 2000. "Sorption Kinetics of Uranium-238 and Neptunium-237 on Glacial Sediment." *Czech. J. Phys.* 50:265-269.

Brooks SC, JK Fredrickson, SL Carroll, DW Kennedy, JM Zachara, AE Plymale, SD Kelly, KM Kemner, and S Fendorf. 2003. "Inhibition of Bacterial U(VI) Reduction by Calcium." *Environ. Sci. Technol 37:*1850-1858.

Callison SW and SW Clark. 2002. *Protection of 300 Area Groundwater from Uranium-Contaminated Soils at Remediated Sites.* BHI-01667, CH2M HILL Hanford, Inc., Richland, Washington.

Chen W and RJ Wagenet. 1997. "Description of Atrazine Transport in Soil with Heterogeneous Nonequlibrium Sorption." *Soil Sci. Soc. Am. J.* 61:360-371.

Clark DL, DE Hobart, and MP Neu. 1995. "Actinide Carbonate Complexes and Their Importance in Actinide Environmental Chemistry." *Chem. Rev.* 95:25-48.

Comprehensive Environmental Response, Compensation, and Liability Act. 1980. Public Law 96-150, as amended, 94 Stat. 2767, 42 USC 9601 et seq.

Connaughton DF, JR Stedinger, LW Lion, and ML Shuler. 1993. "Description of Time-Varying Desorption Kinetics: Release of Naphthalene from Contaminated Soils." *Environ. Sci. Technol.* 27:2397-2403.

Culver TB, CF Brown, and JA Smith. 2000. "Rate-Limited Sorption and Desorption of 1,2-Dichlorobenzene to a Natural Sand Soil Column." *Environ. Sci. Technol*. 34:2446-2452.

Culver, TB, SP Hallisey, D Sahoo, JJ Deitsch, and JA Smith. 1997. "Modeling the Desorption of Organic Contaminants from Long-Term Contaminated Soil Using Distributed Mass Transfer Rates. *Environ. Sci. Technol*. 31:1581-1588.

Curtis GP, P Fox, M Kohler, and JA Davis. 2004. "Comparison of Field Uranium K_d Values with a Laboratory Determined Surface Complexation Model. *Applied Geochemistry*, 19:1643-1653.

Davis JA, and GP Curtis. 2003. *Application of Surface Complexation Modeling to Describe Uranium(VI) Adsorption and Retardation at the Uranium Mill Tailings Site at Naturita, Colorado*. NUREG CR-6820, U.S. Nuclear Regulatory Commission, Rockville, Maryland.

Davis JA, TE Payne, and TD Waite. 2002. "Simulating the pH and pCO_2 Dependence of Uranium(VI) Adsorption by a Weathered Schist with Surface Complexation Models." *Geochem. Soil. Radionuclides. Special Pub. 59*, Soil Science Society of America, Madison, Wisconsin.

Davis JA, DE Meece, M Kohler, and GP Curtis. 2004. "Approaches to Surface Complexation Modeling of Uranium(VI) Adsorption on Aquifer Sediments." *Geochim. Cosmochim. Acta*, 68, 3621-3641.

Dennison DI, DR Sherwood, and JS Young. 1989. *Status Report on Remedial Investigation of the 300 Area Process Ponds*. PNL-6442, Pacific Northwest Laboratory, Richland, Washington.

DOE. 1990. *Remedial Investigation/Feasibility Study Work Plan for the 300-FF-1 Operable Unit, Hanford Site, Richland, Washington*. DOE/RL-88-31, U.S. Department of Energy, Richland, Washington.

DOE. 2005. *Work Plan for Phase III Feasibility Study 300-FF-5 Operable Unit*. DOE/RL-2005-41, Rev. 0, U.S. Department of Energy, Richland, Washington.

Duff MC and C Amrhein. 1996. "Uranium(VI) Adsorption on Goethite and Soil in Carbonate Solutions." *Soil Sci. Soc. Am. J.* 60:1393-1400.

Finch R and T Murakami. 1999. "Systematics and Paragenesis of Uranium Minerals." In *Uranium: Mineralogy, Geochemistry, and the Environment*, Vol. 38, pp. 91-179, PC Burns and RJ Finch (eds.). Mineralogical Society of America, Washington, D.C.

Gabriel U, JP Gaudet, L Spadini, and L Charlet. 1998. "Reactive Transport of Uranyl in a Goethite Column: An Experimental and Modeling Study." *Chem. Geol*. 151:107-128.

Gamerdinger AP, DI Kaplan, DM Wellman, and JN Serne. 2001a. "Two-Region Flow and Rate-Limited Sorption of Uranium(VI) during Transport in an Unsaturated Silt Loam." *Water Resour. Res*. 37:3147-3153.

Gamerdinger AP, DI Kaplan, DM Wellman, and JN Serne. 2001b. "Two-Region Flow and Decreased Sorption of Uranium(VI) During Transport in Hanford Groundwater and Unsaturated Sands." *Water Resour. Res*. 37:3155-3162.

Gee GW, JM Keller, and AL Ward. 2005. "Measurement and Prediction of Deep Drainage from Bare Sediments at a Semiarid Site." *Vadose Zone Journal* 4:32.40

Giammar DE and JG Hering. 2001. "Time Scales for Sorption-Desorption and Surface Precipitation of Uranyl on Goethite." *Environ. Sci. Technol*. 35:3332-3337.

Glynn PD. 2003. "Modeling Np and Pu Transport with a Surface Complexation Model and Spatially Variant Sorption Capacities: Implications for Reactive Transport Modeling and Performance Assessments of Nuclear Waste Disposal Sites." *Computers & Geoscienc*. 29:331-349.

Grenthe I, J Fuger, RJM Konings, RJ Lemire, AB Muller, C Nguyen-Trung, and H Wanner. 1992. *Chemical Thermodynamics Series, Vol. 1: Chemical Thermodynamics of Uranium*. Elsevier Science, Oxford, United Kingdom.

Gustafson DI and LR Holden. 1990. "Nonlinear Pesticide Dissipation in Soils: A New Model Based on Spatial Variability." *Environ. Sci. Technol.* 24:1032-1038.

Hartman MJ, LF Morasch, and WD Webber (eds.). 2004. *Hanford Site Groundwater Monitoring for Fiscal Year 2003*. PNNL-14548, Pacific Northwest National Laboratory, Richland, Washington.

Hem JD. 1985. *Study and Interpretation of Chemical Characteristics of Natural Water.* Water-Supply Paper 2254, U.S. Geological Survey, Reston, Virginia.

Kalmykov SN and GR Choppin. 2000. "Mixed Ca^{2+} /UO_2^{2+} / CO_3^{2-} Complex Formation at Different Ionic Strengths." *Radiochim. Acta* 88:603-606.

Kaplan DI, JN Serne, AT Owen, J Conca, TW Wietsma, and TL Gervais. 1996. *Radionuclide Adsorption Distribution Coefficients Measured in Hanford Sediments for the Low-Level Waste Performance Assessment Project*. PNNL-11485, Pacific Northwest National Laboratory, Richland, Washington.

Kelly SD, MG Newville, L Cheng, KM Kemner, SR Sutton, P Fenter, NC Sturchio, and C Spotl. 2003. "Uranyl Incorporation in Natural Calcite." *Environ. Sci. Technol*. 37:1284-1287.

Kohler M, GP Curtis, DB Kent, and JA Davis. 1996. "Experimental Investigation and Modeling of Uranium(VI) Transport Under Variable Chemical Conditions." *Water Resour. Res.* 32:3539-3551.

Kohler M, GP Curtis, DE Meece, and JA Davis. 2004. "Methods for Estimating Adsorbed Uranium(VI) and Distribution Coefficients of Contaminated Sediments." *Environ. Sci. Technol.* 38:240-247.

Koretsky C. 2000. "The Significance of Surface Complexation Reactions in Hydrologic Systems: A Geochemist's Perspective." *J. Hydrol.* 230:127-171.

Lindenmeier CW, JN Serne, JL Conca, AT Owen, and MI Wood. 1995. *Solid Waste Leach Characteristics and Contaminant-Sediment Interactions, Volume 2: Contaminant Transport Under Unsaturated Moisture Contents.* PNNL-10722, Pacific Northwest National Laboratory, Richland, Washington.

Lorden SW, W Chen, and LW Lion. 1998. "Experiments and Modeling of the Transport of Trichloroethene Vapor in Unsaturated Aquifer Material." *Environ. Sci. Technol.* 32:2009-20017.

Pabalan RT, DR Turner, FP Nertetti and JD Prikryl. 1998. "Uranium(VI) Sorption onto Selected Mineral Surfaces, Key Geochemical Parameters." In A*dsorption of Metals*, Geomedia, Academic Press, EA Jenne (ed.), San Diego, California.

Pedit JA and CT Miller. 1994. "Heterogeneous Sorption Processes in Subsurface Systems: 1. Model Formulation and Applications." *Environ. Sci. Technol.* 28:2094-2104.

Pedit JA and CT Miller. 1995. "Heterogeneous Sorption Processes in Subsurface Systems. 2. Diffusion Modeling Approaches." *Environ. Sci. Technol.* 29:1766-1772.

Pignatello JJ. 2000. "The Measurement and Interpretation of Sorption and Desorption Rates for Organic Compounds in Soil Media." *Adv. Agron.* 69:1-73.

Qafoku NP, CC Ainsworth, JE Szecsody, and OS Qafoku. 2003. "The Effect of Coupled Dissolution and Redox Reactions on $Cr(VI)_{aq}$ Attenuation during Transport in the Hanford Sediments under Hyperalkaline Conditions." *Environ. Sci. Technol*. 37:3640-3646.

Qafoku NP, CC Ainsworth, JE Szecsody, and OS Qafoku. 2004. "Transport-Controlled Kinetics of Dissolution and Precipitation in the Hanford Sediments under Hyperalkaline Conditions." *Geochim. Cosmochim. Acta* 68:2981-2995.

Qafoku NP, JM Zachara, C Liu, OS Qafoku, and SC Smith. 2005. "Kinetic Desorption and Sorption of U(VI) During Reactive Transport in a Contaminated Hanford Sediment." *Environ. Sci. Technol*. (in press).

Read D, D Ross, and RJ Sims. 1998. "The Migration of Uranium through Clashack Sandstone: The Role of Low Molecular Weight Organics in Enhancing Radionuclide Transport." *J. Contam. Hydrol.* 35:235-248.

Read D, TA Lawless, RJ Sims, and KR Butter. 1993. "Uranium Migration through Intact Sandstone Cores." *J. Contam. Hydrol.* 13:277-289.

Record of Decision. 1996. Declaration of the Record of Decision, USDOE Hanford Area 300-FF-1 and 300-FF-5 Operable Units, Hanford Site, Benton County, Washington. Washington State Department of Ecology, U.S. Environmental Protection Agency, and U.S. Department of Energy, Richland, Washington.

Reeder R, M Nugent, G Lamble, CD Tait, and DE Morris. 2000. "Uranyl Incorporation into Calcite and Aragonite: XAFS and Luminescence Studies." *Environ. Sci. Technol*. 34:638-644.

Reeder R, M Nugent, CD Tait, DE Morris, SM Heald, KM Beck, WP Hess, and A Lanzirotti. 2001. "Coprecipitation of Uranium (VI) with Calcite: XAFS Micro-XAS, and Luminescence Characterization." *Geochim. Cosmochim. Acta* 65(20):3491-3503.

Serne JN, CF Brown, HT Schaef, EM Pierce, MJ Lindberg, Z Wang, PL Gassman, and JG Catalano. 2002. *300 Area Uranium Leach and Adsorption Project*. PNNL-14022, Pacific Northwest National Laboratory, Richland, Washington.

Spottl C, M Unterwurzacher, A Mangini, and FJ Longstaffe. 2002. "Carbonate Speleothems in the Dry, Inneralpine Vingshgau Valley, Northernmost Italy: Witnesses of Changes in Climate and Hydrology Since the Last Glacial Maximum." *J. Sed. Res.* 72:793-808.

Stumm W and JW Morgan. 1996. *Aquatic Chemistry*. John Wiley & Sons, New York.

Swanson LC, GG Kelty, KA Lindsey, KR Simpson, RK Price, and SD Consort. 1992. *Phase 1 Hydrogeologic Summary of the 300-FF-5 Operable Unit, 300 Area*. WHC-SD-EN-TI-052, Rev. 0, Westinghouse Hanford Company, Richland, Washington.

Vermeul VR, MP Bergeron, CR Cole, CJ Murray, WE Nichols, TD Scheibe, PD Thorne, SR Waichler, and Y Xie. 2003. *Transient Inverse Calibration of the Site-Wide Groundwater Flow Model (ACM-2): FY 2003 Progress Report*. PNNL-14398, Pacific Northwest National Laboratory, Richland, Washington.

Waichler SM and SB Yabusaki. 2005. *Flow and Transport in the Hanford 300 Area Vadose Zone-Aquifer-River System.* PNNL-15125, Pacific Northwest National Laboratory, Richland, Washington.

Waite TD, JA Davis, BR Fenton, and TE Payne. 2000. "Approaches to Modeling Uranium(VI) Adsorption on Natural Mineral Assemblages." *Radiochim. Acta* 88:687-699.

Wang Z, JM Zachara, PL Gassman, C Liu, O Qafoku, and JG Catalano. 2002. "Fluorescence Spectroscopic Studies of Uranium-Bearing Vadose Zone Sediments." In Appendix D of *Field Investigation Report of Waste Management Area B-BX-BY*. RPP-10098, Rev. 0, prepared by Jacobs Engineering Group, Inc. for CH2M HILL Hanford Group, Inc., Richland, Washington.

Wang Z, JM Zachara, W Yantanssee, C Liu, PL Gassman, and AG Joly. 2004. "Cryogenic Laser Induced Fluorescence Characterization of U(VI) in Hanford Vadose Zone Pore Waters." *Environ. Sci. Technol*. 38:5591-5597.

Wang Z, JM Zachara, JP McKinely, and SC Smith. 2005a. "Cryogenic Laser Induced U(VI) Fluorescence Studies of a U(VI) Substituted Natural Calcite: Implications to U(VI) Speciation in Contaminated Hanford Sediments." *Env. Sci. Technol.* DOI:10.1021/es048448d.

Wang Z, JM Zachara, PL Gassman, C Liu, O Qafoku, and JG Catalano. 2005b. "Fluorescence Spectroscopy of U(VI)-Silicate and U(VI)-Contaminated Hanford Sediment." *Geochim. Cosmochim. Acta* 69(6):1391-1403.

White MD and M Oostrom. 2000. *STOMP, Subsurface Transport Over Multiple Phases v. 2.0 Theory Guide*. PNNL-12030, Pacific Northwest National Laboratory, Richland, Washington.

White MD and M Oostrom. 2004. *STOMP, Subsurface Transport Over Multiple Phases v. 3.1 User's Guide*. PNNL-14478, Pacific Northwest National Laboratory, Richland, Washington.

Distribution

No. of Copies

ONSITE

9 **DOE Richland Operations Office**

BL Charboneau	A6-33
RD Hildebrand	A6-38
JG Morse	A6-38
KM Thompson	A6-38
AC Tortoso	A6-38
Public Reading Room (2)	H2-53
Administrative Record (2)	H6-08

2 **Bechtel Hanford, Inc.**

JA Lerch	L6-06
SG Weiss	H0-23

3 **Fluor Hanford, Inc.**

JV Borghese	E6-35
BH Ford	E6-35
VG Johnson	E6-35

8 **Washington State Department of Ecology**

FW Bond	H0-57
J Caggiano	H0-57
F Hodges	H0-57
AD Huckaby	H0-57
TK Masterson-Heggen	H0-57
J Price	H0-57
E Rochette	H0-57
Ecology Library	H0-57

No. of Copies

3 **U.S. Environmental Protection Agency**

DA Faulk	B5-01
LE Gadbois (2)	B5-01

23 **Pacific Northwest National Laboratory**

PE Dresel	K6-96
EJ Freeman	K9-36
MD Freshley	K9-33
JS Fruchter	K6-96
TJ Gilmore	K6-81
MJ Hartman	K6-96
JW Lindberg	K6-81
SP Luttrell	K6-96
JP McDonald	K6-96
LF Morasch	K6-86
CJ Murray	K6-81
TG Naymik	K6-96
GW Patton	K6-75
RE Peterson	K6-96
JR Serne	P7-22
PD Thorne	K9-33
MJ Truex	K6-96
VP Vermeul	K6-96
MD Williams	K9-36
SB Yabusaki	K9-36
JM Zachara	K8-96
Hanford Technical Library (2)	P8-55